DEVELOPMENT AND CHARACTERIZATION OF ELECTROLESS NI-P COMPOSITE COATINGS WITH SUPERELASTIC NANO-NITI ADDITIONS

by

Marissa MacLean

Submitted in partial fulfilment of the requirements

for the degree of Master of Applied Science

at

Dalhousie University

Halifax, Nova Scotia

May 2019

Table of Contents

List of Tables

List of Figures

Abstract

Many types of protective coatings have been developed to protect oil and gas pipelines from erosion and corrosion damage. Such damage is caused by erosive particles and corrosive media flowing through the pipes. Electroless Ni-P coatings, which are known for their excellent wear and corrosion resistance, have the potential to protect low carbon steel pipelines against a multitude of detrimental conditions. However, low toughness upon deposition limits their current use. Therefore, the objective of this study is to incorporate superelastic nano-NiTi particles into the electroless Ni-P matrix to enhance toughness. Upon applied mechanical stress, these particles will undergo a reversible martensitic transformation that is responsible for superelastic nature. The ability to absorb larger amounts of strain than typical materials can can aid in absorbing crack propagation energy and deflect or arrest cracks in composites. Ni-P-nano-NiTi coatings were successfully plated on API X100 steel substrates and characterized using SEM, XRD, OM, and micro-Vickers hardness. In order to assess the effect of superelastic NiTi on toughness, several tests were done on composite coatings containing 5.14 wt.%, 6.07 wt.%, and 7.02 wt.% NiTi. Scratch and indentation testing using spherical indenters was coupled with acoustic emission to monitor cracking and fracture behaviour. Single particle erosion was done in order to gain perspective on the micro-mechanisms driving erosion in the composite coatings. Bend testing, along with acoustic emission was used to assess bend strength, elastic modulus, and cracking behaviour under bending conditions. It was found that the addition of superelastic nano-NiTi particles resulted in toughening of the monolithic Ni-P matrix under scratch, indentation and single particle conditions. Transformation toughening, micro-cracking, crack bridging and deflection were observed in the coatings.

List of Abbreviations Used

AE	Acoustic Emission
API	American Petroleum Institute
COF	Coefficient of Friction
EDS	Energy Dispersive Spectroscopy
EN	Electroless Nickel
HV	Vickers Hardness
ICP-OES	Inductively Coupled Optical Emission Spectrometry
OM	Optical Microscopy
RPM	Revolutions Per Minute
SE	Superelasticity
SEM	Scanning Electron Microscope
SMA	Shape Memory Alloy
SME	Shape Memory Effect
SPE	Single Particle Erosion
XRD	X-ray Diffraction

Acknowledgements

First and foremost, I would like to thank my supervisor, Dr. Zoheir Farhat for allowing me to be a member of the Advanced Tribology Laboratory and to contribute to the excellent array of work done by past and present members of the group. Your guidance, constructive criticism, and knowledge that you shared with me and the rest of the group was invaluable. I am very grateful to have had the opportunity to work under such a well-respected member of Dalhousie. I'd also like to thank Dr. George Jarjoura, and Dr. Craig Lake for serving as members of my committee. Thank you for your guidance.

A special thanks to my fellow ATL members, and fellow grad students and friends for all of the support. I'd also like to thank all of the staff at Dalhousie who were always willing to lend a helping hand when I needed it. All of your help was very much appreciated. I am grateful for all of the assistance throughout my two years at Dalhousie

Finally, I'd like to thank my parents—my two biggest supporters in everything that I do. Without your encouragement I would not have been able to complete this degree. Thank you for always believing in me and assuring me that I could do anything that I put my mind to.

Marissa MacLean

May 2019

1 Introduction

Every material is susceptible to some form of wear when in contact with another material, resulting in progressive material loss [1]. Whether it be adhesion, abrasion, erosion, corrosion, or another mechanism, this can lead to severe damage, and eventually catastrophic failure [1]. In the case of oil and gas pipelines, these failure mechanisms are accelerated by corrosive gases or solid particulates that flow through the oil and gas pipelines, such as hydrogen sulfide/ carbon dioxide, or contaminants [2, 3, 4]. The Canadian Energy Pipeline Association (CEPA) reported $1.6 billion spent for pipeline maintenance and monitoring in 2017 for Canadian pipelines [5]. While the number of significant incidents has begun to decline for both liquid and natural gas lines, the threat of pipeline failure and potential material release is still possible. The leading cause of these incidents is metal loss, followed by materials, manufacturing and construction, and cracking as seen in Figure 1-1. With the proper preventative measures in place to minimize wear and degradation of the pipe materials, the risk of failure due to these criteria can be minimized. However, damage during pipeline maintenance or construction also poses significant risk for pipeline damage. Thus, the pipelines must have high impact strength and dent resistance in addition to wear and corrosion resistance to limit the likelihood of cracking or failure.

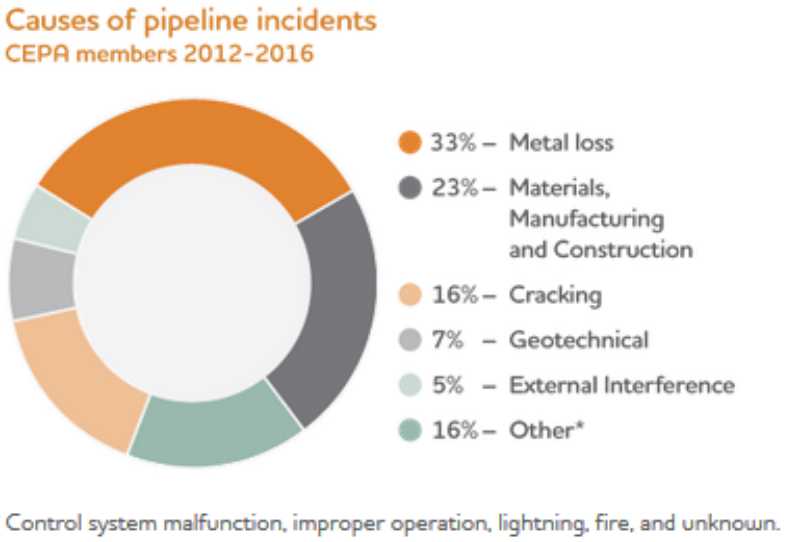

Figure 1-1 Cause of pipeline incidents over a four-year period from the CEPA 2017 annual performance report [6]

To protect pipelines different preventative measures have been adopted including simply changing the pipeline material, or the application of coatings [2]. However, choosing a more durable and corrosion resistant material can prove to be costlier. Protective coatings, particularly polymer based, introduce other issues such as thermal damage during assembly [7]; other epoxy based coatings do not provide significant protection against certain chemicals found in crude oil [3]. Therefore, there is room for improvement of these protective coatings in order to find a solution that provides the highest protection with minimal need for replacement or re-coating procedure.

Electroless nickel phosphorous (EN) coatings have become increasingly popular over the past 70 years. These coatings are plated electrolessly, meaning that no external current is required [8]. This allows for a more uniform coating, particularly on complex parts, in comparison with typical electrodeposition methods [9]. With no external current being applied, the integrity of these coatings does not rely on the current density and thus the entire surface will coat uniformly. This also results in a decrease in production cost in comparison to electrodeposition. Due to their superior wear and corrosion properties, EN coatings are an excellent candidate to be used as protective coatings of oil and gas pipelines.

The coating deposition mechanisms, and coating properties will be reviewed in the following sections.

These coatings are known for their high wear resistance, high hardness, and excellent corrosion resistance, among other desirable properties [9]. However, these coatings exhibit low toughness upon deposition [10]. Lately, researchers have been working to develop electroless Ni-P composite coatings, which involve either the addition of secondary alloying elements, or the incorporation of second phase particles to enhance the properties of these coatings [8]. Work has been done implementing single elements such as copper, or tungsten but compounds such as silicon dioxide, tungsten carbide, and more have also been explored as second phase additions. These composite coatings exhibit superior properties such as hardness and wear resistance in comparison to the monolithic Ni-P coatings. Little of present research in electroless composite coatings has been to increase toughness, thus presenting a need for this study.

Superelastic NiTi is an excellent candidate as a second phase particle for electroless Ni-P composite coatings. First discovered in the 1960s, this equiatomic alloy is known to possess both shape memory and superelastic characteristics, which means that after thermal or mechanical stress the material is able to recover its original shape or endure large recoverable strains respectively [11]. This is possible due to a reversible martensitic transformation characteristic of shape memory alloys. The superelastic characteristic is particularly of interest due to its potential ability to absorb crack propagation energy therefore increasing toughness and dent resistance of electroless Ni-P coatings. Transformation toughening resulting from the martensitic transformation, and other toughening mechanisms due to the addition of a second phase particle will be discussed below.

In order to fully characterize these coatings, it is necessary to test them under several degradative conditions including sliding wear and Hertzian indentation. This requires a full understanding of the contact between the coated surfaces and the indenter, or the erosive particles. Elastic contact based on Hertzian contact theory will be discussed. In addition to understanding contact mechanics, the ability to assess the material behaviour upon fracture is also required. Different fracture mechanisms and crack types will also be examined.

The objectives of this work are as follows:

1. Successfully plate electroless Ni-P-nano-NiTi coatings on a low carbon steel substrate
2. Characterize the composite coatings (composition, deposition rate, hardness)
3. Inspect the performance of the composite coatings under scratch, indentation, erosion and bend tests
4. Compare the performance of the composite coatings to the performance of monolithic Ni-P coating
5. Identify toughening mechanisms present in the coatings due to the addition of superelastic NiTi

The content of this thesis is divided into five chapters. A literature review on EN coatings, NiTi shape memory alloys, EN composite coatings, contact mechanics, and fracture mechanics is provided in Chapter 2. Experimental procedures are listed in Chapter 3. All results are examined, and a formal discussion is presented in Chapter 4. Conclusions and future recommendations are considered in Chapter 5.

2 Literature Review

2.1 Electroless Ni-P Coatings

First successfully developed by Brenner and Riddell in 1944, electroless nickel phosphorous (EN) coatings have found use in many applications [8, 9]. The most common uses for these coatings include applications requiring wear resistance, corrosion resistance, and instances requiring high hardness. Ni-P coatings are also used for their conductive, lubricious and magnetic properties [12]. These coatings find use in metal finishing and electronics [13]. Nickel can be plated through electroless means, such that no external electric current is required. With the proper plating bath constituents, phosphorous can be co-deposited in the presence of heat. This electroless deposition is more efficient than electrolytic deposition (which requires the use of an external current) because it can follow contours and complex geometry of the substrate for a more uniform coating whereas electrolytic is dependent on electric current and is not consistent in corners and other complex geometries [14, 15]. Electroless Ni-P coatings are hard, brittle, lubricious, and solderable [16]. If heat treated, their hardness can be further increased due to the precipitation of hard intermetallic phases, driving the wear resistance to match the caliper of chromium coatings [17]. Ni-P coatings are self-lubricating due to the phosphorous, which results in a low coefficient of friction. These coatings also exhibit high corrosion resistance, particularly when the P content is high [9, 15].

2.1.1 Autocatalytic Reaction Mechanism

Electroless plating is driven by an autocatalytic reaction mechanism, the reaction kinetics of which are dictated by the substrate being plated on. This autocatalytic process requires the use of a reducing agent to supply electrons for the reduction of nickel, a complexing agent to control free nickel ions, and a stabilizer/inhibitor to control reduction so that

deposition only occurs on the substrate being plated [8, 18]. A source of nickel, typically in the form of a nickel salt, is required for plating. Usually supplied in the form of nickel sulfate or nickel chloride, Ni^{2+} ions undergo reduction to Ni on the autocatalytic substrate surface [8, 16]. Sodium hypophosphite (NaH_2PO_2) is typically used as a reducing agent for Ni-P plating [18]. Once the NaH_2PO_2 is oxidized, Ni^{2+} ions get cathodically reduced on the substrate surface [9, 16]. The reduction of Ni is characterized by equations 1-3 [18].

$$3NaH_2PO_2 + 3H_2O + NiSO_4 \rightarrow 3NaH_2PO_3 + H_2SO_4 + 2H_2 + Ni \quad \text{(Equation 1)}$$

$$2H_2PO_2^- + Ni^{2+} + 2H_2O \rightarrow 2H_2PO_3^- + H_2 + 2H^+ + Ni \quad \text{(Equation 2)}$$

$$Ni^{2+} + H_2PO_2^- + H_2O \rightarrow Ni^0 + H_2PO_3^- + 2H^+ \quad \text{(Equation 3)}$$

Once the first layer of Ni is deposited, it acts as a catalyst for the remainder of the process. The deposition rate can be affected by many variables, including temperature, pH, the concentration of Ni^{2+}, the reducing agent and its' concentration, the bath load, and the agitation factor [9, 14]. These variables will be discussed in further detail in later sections.

The hypophosphite reducing agent provides a supply of P and therefore P simultaneously co-deposits alongside Ni reduction. Gonzalez states that the ideal concentration of $H_2PO_2^-$ is between 0.15- 0.3 M [19]. The phosphorous reduction reaction can be seen in equations 4 and 5 below [18].

$$H_2PO_2^- + \frac{1}{2}H_2 \rightarrow H_2O + OH^- + P \quad \text{(Equation 4)}$$

$$3H_2PO_2^- \rightarrow H_2PO_3^- + H_2O + 2OH^- + 2P \quad \text{(Equation 5)}$$

This co-deposition results in the formation of the desired Ni-P coating, which is characterized by equation 6 [18]:

$$H_2PO_2^- + H_2O \rightarrow H^+ + HPO_3^{2-} + 2H \quad \text{(Equation 6)}$$

Following the atomic hydrogen theory, hydrogen is absorbed, and subsequently consumed. This results in the deposition of Ni-P, characterised by equations 7 and 8.

$$Ni^{2+} + 2H \rightarrow Ni + 2H^{+} \quad \text{(Equation 7)}$$

$$H_2PO_2^- + H \rightarrow P + OH^- + H_2O \quad \text{(Equation 8)}$$

2.1.2 Coating Microstructure and Properties

When prepared properly, EN coatings are homogeneously deposited onto a substrate. Coating adhesion is affected by thickness, phosphorous content, and ductility of the substrate [14]. Strong adhesion between the coating and the substrate is ideal in order to avoid delamination.

The final phosphorous content in the matrix is dependent upon the bath composition. Ni-P coatings are classified into three categories; low phosphorous, medium phosphorous, and high phosphorous. Low phosphorous, which contains between 1-5 wt.% P, exhibits high hardness and wear resistance, while a high phosphorous coating (9-11wt.% P) is used for its excellent corrosion resistance. Medium phosphorous contains between 6-9 wt.% P [14]. Low phosphorous coatings are typically microcrystalline [14]. On the other hand, high phosphorous coatings are amorphous. Medium phosphorous coatings are typically a mixture of crystalline and amorphous [9, 14]. The degree of crystallinity depends on the phosphorous content, heating rate, heat treatment temperature and time, and the previous thermal history [9].

As seen from the equilibrium phase diagram in Figure 2-1 (a) on cooling, the alloy forms α-Ni and Ni_3P. The respective concentrations of each phase are dependent on temperature and the concentration of P in the matrix. However, Ni-P coating microstructure is non-equilibrium as deposited [9]. In this non-equilibrium structure (Figure 2-1 (b)), two addition phases are present β, which is a crystalline solid solution phase, and γ, which is an amorphous phase [9].

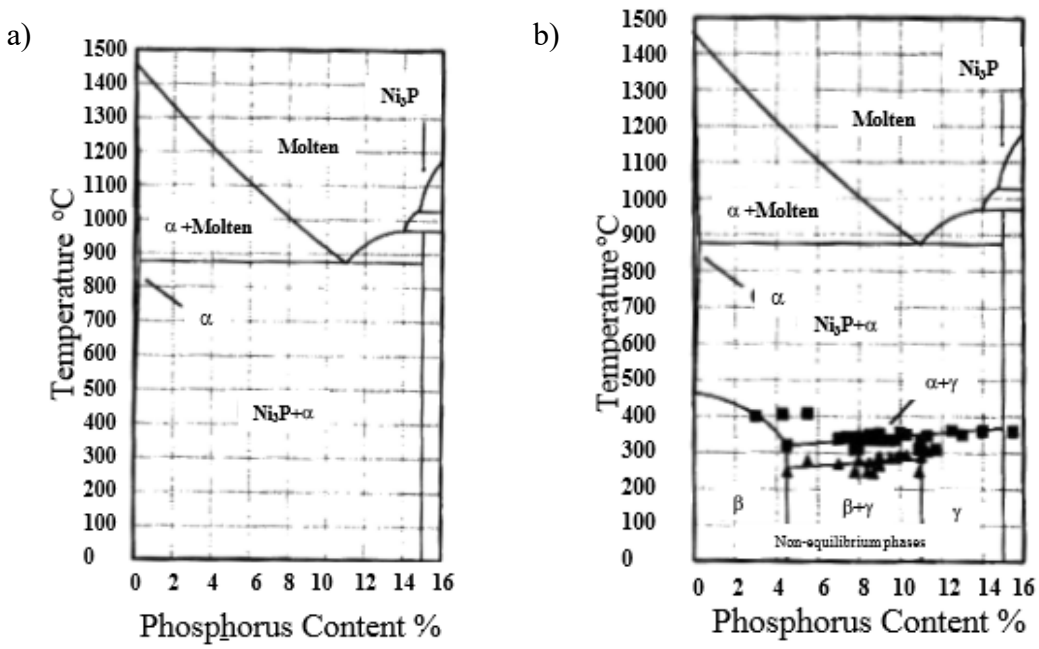

Figure 2-1 a) Equilibrium Ni-P phase diagram and b) non-equilibrium Ni-P phase diagram [9]

Due to the amorphous crystal structure of the coating [15], a high tensile strength and strain are present, which increases with increasing phosphorous content. When the phosphorous content is between 4-7.5 wt.%, the microstructure is in an incoherent (brittle) state, consisting of both β and γ phases. At this point, the internal stress is at a maximum tensile value, thus, ductility is at its lowest at this point [9]. On the other hand, if the phosphorous content is below 4 wt.% or above 11wt.%, the microstructure is either β phase or γ phase respectively, producing a coherent microstructure. Thus, at this point the internal stress is compressive [9]. When the structure is single phase, ductility increases [9]. That being said, ductility is still relatively low [20].

Ni-P coatings have high wear resistance, due to their high hardness. However, different conditions affect the hardness of the coating. In general, an increase in P content lowers the hardness, due to the formation of a softer, γ phase at higher concentrations [9]. Therefore, the maximum hardness is obtained at 4 wt.% P, which corresponds to the single β phase [9].

Taheri stated that mechanical and corrosion properties of the Ni-P coatings are directly related to the state of internal stress [9]. Internal stress is "the force, free from external

forces that is created within the deposit that tends to change the shape of the deposit in order to relieve the force" [20]. As mentioned previously, the state of internal stress is initially tensile, however once the P content is sufficiently high, this stress changes to compressive [9]. Internal stress is also a function of bath age. As the bath gets older, the internal tensile stress approaches a maximum [9].

As mentioned above, corrosion resistance is a maximum in high phosphorous coatings. This resistance is attributed to a lack of grain boundaries and the formation of passive layers [20]. These coatings act as barrier coatings which protect the substrate from the corrosive environment in which it comes into contact with [20].

2.1.3 Plating Variables and Their Effect on Deposition and Coating Properties

Coating deposition rates as well as coating properties are highly dependent upon the conditions in which they are plated. Should hypophosphite form molecular hydrogen rather than atomic hydrogen, following equation 9, the reducing power will be compromised [8]. This reduces the efficiency of the coating process and results in a less than adequate deposition.

$$H_2PO_2^- + H_2O \rightarrow H^+ + HPO_3^{2-} + H_2 \qquad \text{(Equation 9)}$$

Another reaction that negatively affects the coating process is the precipitation of nickel orthophosphite. This reaction depletes the concentration of nickel ions in the plating bath, which in turn produces a rougher coated surface than desired [8]. The formation of nickel orthophosphite can be seen in equation 10.

$$Ni^{2+} + H_2\,PO_3^{2-} \rightarrow \ NiHPO_3 \qquad \text{(Equation 10)}$$

The temperature of the plating bath and the pH of the plating bath are crucial to ensure a stable bath. A change in temperature of the plating bath has a direct effect on the deposition rate. It has been seen that an increase in temperature results in an increase in deposition rate. Typical temperature ranges for plating baths include 80-90 °C for acidic solutions,

and 40 °C or higher for alkaline solutions [9]. Since plating time and coating thickness are approximately linearly related, temperature in turn also influences the thickness of the coating. Should the temperature of the plating bath get too high or too low, deposition will slow down, or the bath will become unstable, respectively [8]. By increasing pH, Ni reduction is accelerated, and P reduction is retarded. This results in a lower P content, which in turn increases the deposition rate. In some cases, the hypophosphite reaction can go from catalytic to homogeneous, which results in spontaneous decomposition of the solution with Ni deposition and a lower solubility of nickel phosphate. This initiates decomposition, which results in rough, less desirable deposits. Lowering the pH would prevent deposition of basic salts and hydroxides, thus lowering the reducing power of hypophosphite. This creates a more effective buffering action of bath species [9]. For an acid plating bath, the ideal pH is around 5 [9].

2.2 Shape Memory Alloys

First observed by Ölander in 1932 [21], the discovery of pseudoelasticity of an Au-Cd alloy was the starting point of many discoveries regarding a particular group of alloys with special properties. These alloys—designated "Shape Memory Alloys"—have the ability to restore their original shape and endure large recoverable strains. Shortly after Ölander's initial finding, in 1938, martensitic phase transformation behavior was observed by Greninger and Mooradian in a Cu-Zn alloy. Nearly a decade later, the shape memory effect was extensively studied by Kurdjumov and Khandros, as well as by Chang and Read [21]. The shape memory effect as well as pseudoelastic phenomena will be discussed below.

Adharapurapu lists the requirements for shape memory and superelastic behavior [22], which are as follows:

i. Thermoelastic nature of the martensitic phase transformation that leads to a mobile boundary between both phases, hysteresis, and avoidance of permanent slip
ii. Ordering which guarantees the reverse portion of the transformation

iii. Group-subgroup relationship between austenite and martensite that leads to twinning, which also allows the reverse transformation to take place

2.2.1 Shape Memory Effect

Under certain conditions, a select number of alloys can recover their shape with an increase in temperature. These alloys are called shape memory alloys and undergo a diffusionless shear phase transformation from a parent phase to martensite [21, 23, 24]. This phase transformation occurs on the atomic level [21]. The parent, or austenitic phase, is a high temperature phase [24]. It has a cubic structure and exhibits high symmetry which allows it to form many martensitic variants under thermal stress [24]. In comparison, the martensitic phase is stable at low temperatures and has low symmetry [24]. Martensitic crystal structures include tetragonal, orthorhombic, or monoclinic [11]. A schematic of this shape memory affect in terms of temperature and load can be seen in Figure 2-2 [21].

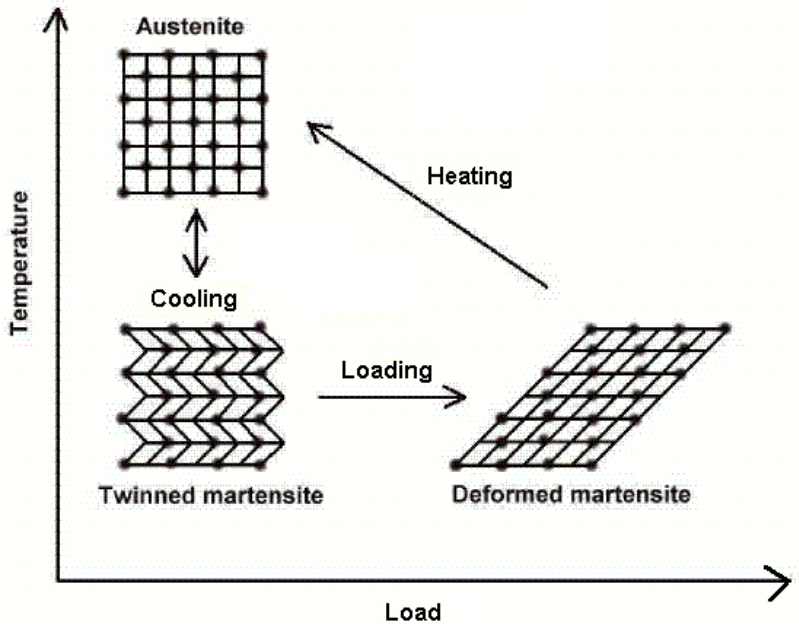

Figure 2-2 SME/ SE Effects showing austenite to martensite forward and reverse transformation [11]

The transformation required to induce the shape memory effect occurs by shear lattice distortion as a result of the structures desire to exist at its lowest energy state [11, 21]. This distortion occurs along a habit (or lattice invariant) plane, which forms an interface between the austenite and martensite phases [11, 24]. This transformation occurs by two mechanisms: slip, which is the movement of atoms by one or more atomic space, and twinning, which is the movement of atoms through a fraction of an atomic space. Twinning is the most common mechanism [11]. Both of these lattice invariant shear mechanisms cause the formation of martensite with minimal permanent volumetric change in material [11].

On cooling, austenite changes to martensite through a forward transformation. Upon reheating, the reverse transformation takes place and the structure reverts back to the austenitic phase. Twinned martensite is formed by the combination of self-accommodated martensitic variants, where the arrangement of variants is such that each variant accommodates the strain of the other variants. The four transformation temperatures are [11, 24]:

1. Martensitic start temperature (M_s): on cooling austenite transforms into twinned martensite under zero load
2. Martensitic finish temperature (M_f): temperature at which the entire material is fully martensitic
3. Austenitic start temperature (A_s): during heating a reverse transformation initiates
4. Austenitic finish temperature (A_f): the transformation is complete

Austenite can also transform into detwinned martensite, in the presence of an applied load. If a mechanical load is applied to the twinned specimen, and is enough to start the detwinning process, reorientation of variants occurs. This results in a macroscopic shape change, and the deformed configuration is retained when the load is released. The atoms are displaced while maintaining their original atomic bonds, which allows for the reverse transformation to occur upon heating [11]. Upon heating above A_f, this transformation takes place and detwinned martensite transforms into austenite with a complete shape recovery. Cooling below M_f leads to the formation of twinned martensite again, with no shape change [11].

2.2.2 Superelasticity

While the SME is a useful property, SMA's have the potential to exhibit superelastic properties as well, which is the focus for this research. At temperatures above the typical shape memory transformation temperatures, this phenomenon is observed with the aid of an applied external load [21]. A large, nonlinear, recoverable strain is observed upon loading and unloading [25]. The SMA has the ability to be strained several times more than any typical alloy, without undergoing plastic deformation [21].

Under low loads, the interface between the martensitic and austenitic phases is mobile, and the strain is within the superelastic strain range. Austenite undergoes elastic loading as the mechanical load is applied. This stress induced martensitic transformation is accompanied by large inelastic strains. Once the applied load is released, the material returns to its original shape as martensite transforms back into the austenitic phase. A schematic of a pseudoelastic stress-strain curve for the phase transformation from austenite to martensite can be seen in Figure 2-3. As indicated in the figure, there is a specific start and finish stress for the forward and the reverse transformations. These stresses are as follows [11]:

1. Austenitic start stress (σ_{As}): Stress required to initiation phase transformation to austenite
2. Austenitic finish stress (σ_{As}): Stress at which all of the material is converted to austenite
3. Martensitic start stress (σ_{Ms}): Stress required to initiate martensitic phase transformation
4. Martensitic finish stress (σ_{Mf}): Stress at which all of the material is converted to martensite

Pseudoelasticity is typically characterized by a plateau during unloading on the stress-strain curve [22]. This plateau is caused by yielding of the austenitic phase due to the application of a critical stress [22]. The martensitic variant capable of accommodating the highest amount of strain forms from the parent phase, and eventually begins to elastically deform once it has completely transformed to martensite [22].

From the stress-strain curve, it can be seen that there is a hysteresis effect taking place during the transformation. Ryhanen defines this as "the difference between the temperatures at which the material is 50% transformed to austenite upon heating and 50% transformed to martensite upon cooling" [21]. This temperature difference is typically between 20-30°C [21], and represents the difference between M_f and A_s, or M_s and A_f. Thus, the temperature range for the forward transformation is higher than the reverse transformation [21]. Hashemi and Smith attribute this property to the sliding and rotation of grains or clusters of grains [26].

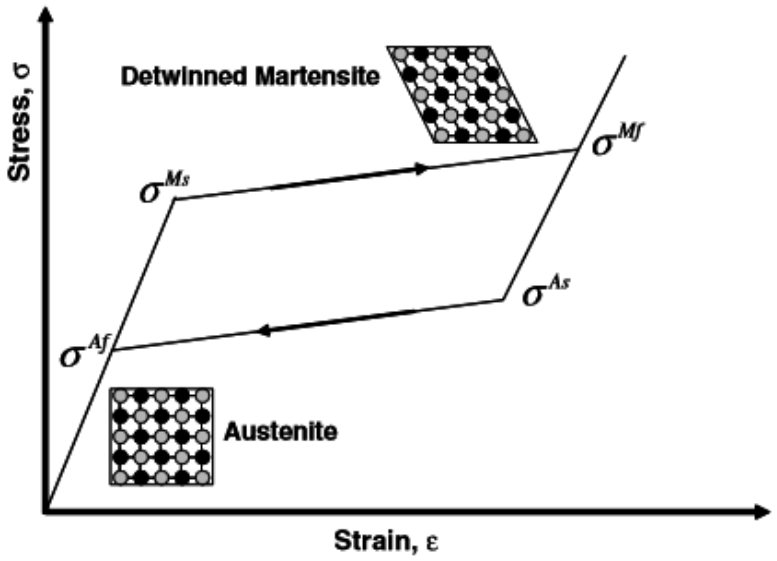

Figure 2-3 Typical pseudoelastic stress-strain curve for SMA [11]

Under sufficiently high loads, the stress required for slip is less than the stress required for the phase transformation from austenite to martensite. [21, 22, 27]. Thus, there is some deformation by slip and the superelastic properties are not fully functional [27].

2.2.3 NiTi Shape Memory Alloy

The shape memory effect of a nickel titanium alloy was first discovered by Buehler and coworkers in the 1960s in an equiatomic alloy. The discovery was made at the Naval Ordnance Laboratory, and thus the alloy was termed "Nitinol" after the alloy (NiTi) and

the lab at which it was discovered (Naval Ordnance Laboratory) [21]. NiTi SMA's find use in biomedical devices and bearings due to their low elastic modulus, superior oxidation resistance and fatigue resistance [28, 29, 30].

From the phase diagram (Figure 2-4), it is seen that at a nearly equiatomic composition below approximately 600°C, only the intermetallic phase NiTi is present. However, should the composition or the temperature vary, the formation of other intermetallic compounds may occur. These include Ni_3Ti and $NiTi_2$, depending on the composition. At higher temperatures, NiTi is present over a wider range of compositions.

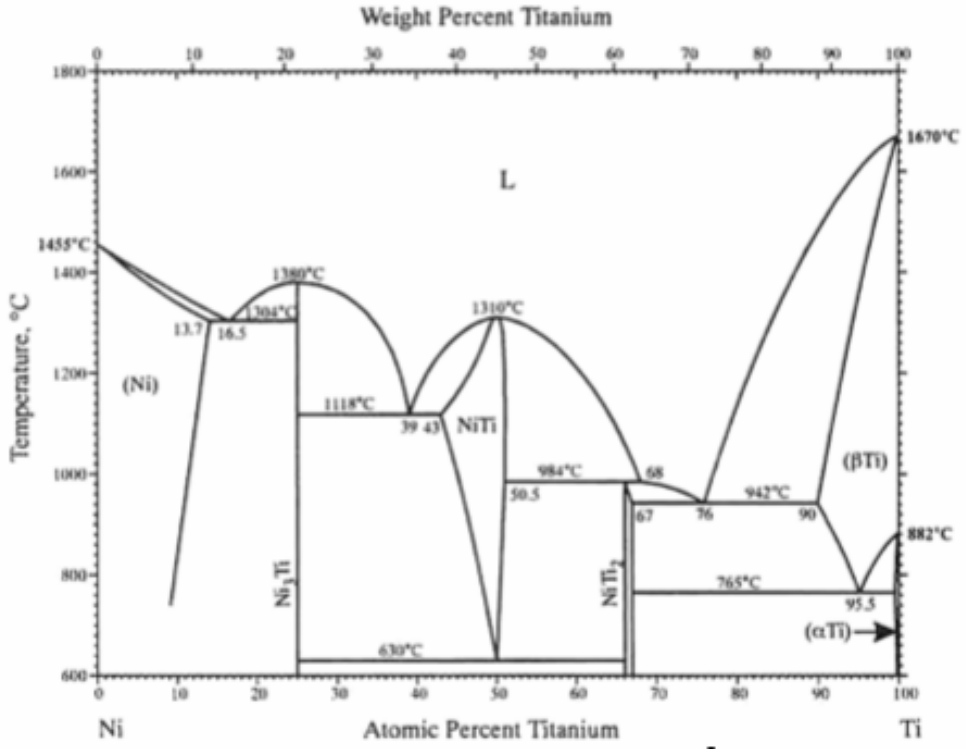

Figure 2-4 Equilibrium phase diagram of Ni-Ti [31]

Three different crystal structures have been observed in NiTi. Austenite is a highly ordered cubic structure (B2) in which a single Ni atom is surrounded by Ti atoms [11, 24, 27, 32]. This unit cell is also known as a CsCl structure and at room temperature has a lattice parameter of 0.3015 nm [27]. This phase is known for its high hardness and strength [21]. No variants of this structure exist, as it has only one possible orientation [21]. Due to the

simultaneous movement of a large number of atoms associated with twinning, inducing thermal energy to the system will inhibit motion, thus decreasing the ductility [23].

Martensite has a related, yet distorted structure to that of austenite. Due to the high symmetry of the austenitic parent phase, 24 martensitic variants can be formed [11, 27]. Variants are crystal structures with different orientations or configurations [27]. Martensite is polymorphic, and can be orthorhombic, monoclinic or tetragonal depending on the temperature. The martensitic structure that forms depends on the composition as well as the alloying elements added [11]. The monoclinic structure (B19'), which forms after the orthorhombic B19 structure, is the most stable martensitic phase [24, 27, 32]. The martensitic phase is the softer, more ductile phase [21].

The "R-Phase" is an intermediate, trigonal phase that presents itself occasionally during the transformation. Generally, this phase occurs before the formation of B19', however it does not always form [27]. It can be characterized by a sudden increase in electrical resistivity of the sample [27]. In order for the R-phase to occur, there needs to be either an increase in nickel concentration, cold working followed by heat treatment, or thermal cycling [33]. Inamura et al characterize the R-phase by the appearance of platelets in the microstructure under scanning electron microscope [34].

While NiTi shape memory alloys are most widely known for their ability to revert to their original shape or recover large amounts of strain under certain conditions, other properties make the alloy desirable as well. While Nitinol has a similar melting point and electrical resistivity (at low temperatures) to 316L stainless steel, it has a lower density and a higher ultimate tensile strength. The lower density makes it more ideal for aerospace applications. NiTi also has good damping properties [21, 23]. Schuerch stated that NiTi can undergo tensile elongations up to 20%, can retain its ductility at cryogenic temperatures, and exhibits excellent fatigue resistance [23]. In comparison to other known SMAs, Nitinol has the highest ductility and excellent corrosion resistance [26].

This shape memory alloy exhibits high wear resistance and excellent flexibility [35]. NiTi also exhibits excellent corrosion resistance. Richman showed that NiTi had the lowest relative cavitation-erosion rates compared to cast martensitic stainless steel, austenitic

stainless steel, duplex stainless steel, Stellite 6, Stellite 21 and a Co-containing steel (IRECA) after explosive welding [32].

It should be noted that while decreasing the atomic percentage of Ni does not affect the transformation temperatures, increasing the atomic percentage of Ni results in a large decrease in transformation temperatures [11]. For example, Schuerch reported that increasing the atomic percent of Ni from 50-53 at. % resulted in a decrease in transition temperature from 165 to -50°C [23]. The transformation temperatures are also affected by alloying elements, as mentioned previously. Kök and Ateş studied the effects of adding different alloying elements to NiTi SMAs, including Mn, Sn, Cr, Cu and Co [36]. They found that the addition of alloying elements shifted as well as shortened the range of transformation temperatures from DSC measurements [36]. The addition of two elements—Cr and Co showed the greatest affect on the transformation temperatures, bringing the M_f temperature down to ~ -20°C and the A_f to ~ 10°C. The Ni-45at%. Ti alloy showed the M_f and A_f temperatures at ~ 50°C and ~ 100°C in comparison. The transformation peaks also became much sharper with the addition of alloying elements [36].

2.3 Electroless Ni-P Composite Coatings

Composite coatings have been developed to improve existing properties of Ni-P coatings. Ploof defines composite electroless nickel coatings as "those that incorporate distinct particles into the deposit to impart a specific property" [37]. These coatings can either involve the addition of other alloying elements, or particle incorporation [38]. Since the focus of this research is on the incorporation of nano-particles, this section will focus strictly on the latter.

Particle incorporation in electroless Ni-P coatings has been extensively studied, with research beginning in the 1960s [38]. Particles are incorporated through surface modification, convection, diffusion, migration across the electrical double layer, and physical embedding [39]. Celis and Ghosh state that the composite coating characteristics

are defined by the number of incorporated, non-agglomerated nano-size particles per unit volume [40]. Coating deposition is influenced by the following:

- particle concentration
- coating surface roughness and morphology
- void fraction and hardness
- particle characteristics
- bath composition
- flow environment and
- substrate conditions.

2.3.1 Factors Affecting Particle Incorporation

Several factors affect the incorporation of particles into the Ni-P matrix to form adequate composite coatings, including particle properties, and plating conditions [38]. Particles must be large enough to settle within the bath solution, yet not so large as to induce roughness in the coating or to affect the suspension properties [38]. The optimal size, however, depends on the desired thickness of the coating. Balaraju has suggested that the optimal particle size is between 4-7 μm, while other studies have suggested even smaller particle sizes [38]. Celis and Ghosh stated that particle content is inversely proportional to particle size, which can be attributed to a lack of surface area for incoming particles to attach to at the electrode due to the large volume of particles [40]. Particle shape will also affect the deposit. Smooth surfaces have been found following the incorporation of small rounded particles, while rough surfaces have been found from incorporating large, angular particles [38]. While having a rough surface on the substrate initially aids in deposition, smooth surfaces are more desirable in the final product, especially if high corrosion resistant is a requirement.

To properly disperse the particles within the solution and prevent agglomeration or flocculation, appropriate agitation must be used. Balaraju has found that circulation by pumping or controlled air sparging are the best methods of agitation for particle

incorporation [38]. It has also been noted that the most effective agitation speed corresponds to the laminar-turbulent transition flow region. Purely laminar flow results in a stirring speed that fails to achieve complete particle dispersion, where as purely turbulent flow results in poor particle incorporation due to insufficient time for attachment to the substrate surface [38].

Orientation of the samples also plays a key role in deposition. It has been found that samples hung horizontally contained twice the number of particles that were obtained from hanging the samples vertically, if the samples were facing upwards. In comparison, if hung horizontally, samples facing downwards showed very few particles on the surface [38].

Arguably, the most important factor in particle incorporation is the concentration of the second-phase particles within the plating bath. Studies on the incorporation of Si_3N_4, CeO_2, and TiO_2 (not mentioned in detail in this review) particles showed an increase in particle concentration in the Ni-P matrix with increasing additions to the plating bath. However, at a certain concentration of particles, a saturation point is reached. Beyond this point agglomeration and settling of the second-phase particles can occur, which decreases the particle incorporation into the Ni-P matrix [38].

2.3.2 Effects of Particle Incorporation on Ni-P Coating Properties

As mentioned above, the main objective of producing electroless composite coatings is to improve upon existing properties of monolithic Ni-P coating. The majority of particle incorporation found in the literature revolved around improving hardness, wear resistance, or corrosion resistance.

From the work of Islam et al [39], it was found that the addition of SiO_2 nanoparticles in the Ni-P matrix resulted in grain refinement, a decrease in surface roughness, and a reduction in surface porosity which increased the coating density. These factors contributed to an increase in hardness (approximately 11 GPa). The addition of the SiO_2 nanoparticles also resulted in superior corrosion resistance from the medium phosphorous coatings [39]. This agreed with the work previously done by Afshar and Sadreddini, who found an

increase in corrosion resistance with the addition of SiO_2 nanoparticles, due to a decrease in porosity [41].

Titanium nitride (TiN) is used for its wear resistance and diffusion barrier properties [42]. Mafi et al [43] studied the effects of adding TiN nanoparticles to a high phosphorous deposit. The addition of TiN nanoparticles resulted in a nodular surface, with a uniform distribution of the nanoparticles within the Ni-P matrix. Deposition rate decreased due to surface coverage of the surfactant, and the fact that the nanoparticles act as a barrier for Ni-P codeposition. Hardness was also found to increase, and heat treatment increased the hardness further due to nickel phosphide formation. Corrosion properties were diminished due to a combination of three things: the high electrical conductivity of TiN, the rough surface of the specimen, and a galvanic cell that is set up between the nanoparticles (cathode) and the Ni-P matrix (anode) [43]. Huang et al also found that the addition of uniformly distributed TiN nanoparticles increased the hardness and wear resistance of the coating [44], which they attribute to dispersion strengthening due to the presence of the nanoparticles [44].

Tungsten carbide (WC) is also added for its wear resistance properties. Luo et al [45] found that the addition of WC nanoparticles resulted in an amorphous coating with the nanoparticles being well dispersed within the Ni-P matrix. Microhardness was improved compared to the bulk, and further through heat treatment. Corrosion resistance was also improved [45]. The addition of WC particles was also found to increase the abrasion resistance of steel by approximately 13 times, compared to an increase of three times for only the bulk [46]. The optimal concentration of WC was found to be approximately 20 g/L, with any additional particles decreasing the number of particles incorporated into the matrix. Aal et al devotes this to the fact that at this concentration, the number of co-depositing particles is equivalent to the number of particles approaching the substrate, and thus steady state equilibrium is reached [46]. Any further addition of particles results in particle agglomeration, and likely a non-uniform coating.

The addition of TiC to EN coatings has been studied by Afroukhteh et al [47]. In this study, Ni-P-TiC was plated on low carbon steel using a Ni-P matrix with a high phosphorous content. The addition of TiC nanoparticles showed changes in surface morphology,

deposition rates, and phosphorous content. Different amounts were added to several samples and it was found that higher concentrations of TiC nanoparticles resulted in a nodular structure where the TiC was trapped, and the Ni-P matrix showed a fine nodular structure [47]. The deposition rate was slow when <0.1g/L of TiC nanoparticles were used, while the highest rate was obtained from co-deposition with the 0.3g/l TiC nanoparticles. The phosphorous content was decreased with increasing amounts of TiC nanoparticles. Co-deposition of TiC nano-particles with Ni-P did not show uniform distribution.

The addition of SiC particles resulted in an increased micro-hardness in the amorphous coating plated on a cast iron substrate [48]. This is in agreeance with the results found from the work of Apachitei et al, which found that the as-deposited coating had an HV_{100} of approximately 705, compared to a Ni-P coating with a micro-hardness of approximately 600 HV_{100} [49]. It was also found from Chang et al that the hardness depends on the SiC content in the coating film, film thickness, phases and chemical compounds formed upon different heat treatments, spread of dislocation types, and more. Wear and corrosion resistance benefited from the addition of SiC nanoparticles. It was found that the addition of the SiC particles to the plating bath decreased the corrosion resistance, similar to research conducted with TiN [48]. Due to the brittle nature of these coatings, Colombo, Molinari and Straffelini reported that Ni-P-SiC composite coatings have poor rolling-sliding resistance in comparison to coatings with other particles incorporated such as BN, MoS_2 and PTFE [50].

The addition of diamond to a Ni-P coating is chosen to improve wear resistance [37]. Karaguiozova [51] studied the affects of the addition of nano-diamonds to a Ni-P matrix for strengthening purposes. It was found that the addition of nano-diamonds did in fact increase the micro-hardness of the coatings, and the optimal wear resistance was found with 3 g/L of nano-diamond particles. The study also examined the effects of adding the nano-particles in as dry particles versus in suspension versus in a coating. The bilayer coating prevailed as the best option, having the highest micro-hardness and minimum weight loss due to wear [51].

Azari-Dorchech et al studied the effects of adding B_4C to Ni-P coating [52]. Added for its extremely high hardness, low density, and wide range of temperature applications, the Ni-

P-B_4C coatings were found to increase the hardness of the coatings plated on low carbon steel substrates [52]. Wear resistance was tested at different loads for different concentrations of B_4C in the matrix. It was found that the optimum wear resistance was at 25 vol.%, increasing up to 90 % in comparison to the bulk Ni-P coatings [52]. However, any additional increase above 25 vol.% was found to decrease the wear resistance due to an increase in crack nucleation [52].

2.4 Hertzian Contact

When one body comes into contact with another under an applied load, a stress field is generated. Upon contact with a substrate, an indenter will generate a stress field within said material. This stress field depends greatly on the geometry of the indenter, as well as the bulk material properties. Spherical indenters will be the focus of this research. Stress fields generated under spherical indentation will be examined below for the elastic case.

Elastic contact is analysed using appropriate distributions of normal pressure on a semi-infinite half space. This is best described by Hertz, who examined the nature of localized deformation and the distribution of pressure between two elastic bodies that come into contact [53]. The following assumptions are made for Hertzian contact [53]:

1. Radii of curvature of the contacting bodies is much larger than the radius of the circle of contact, thus each surface can be treated as an elastic, semi-infinite half-space
2. The dimensions of each contacting body are much larger than the radius of the circle of contact. Thus, indentation stresses and strains can be considered independently from those arising from the geometry, method of attachment, and boundaries
3. Contact between bodies is frictionless, and thus only normal pressure is transferred between the indenter and the sample surface
4. The distance between surfaces of two bodies is equal to zero inside the circle of contact, and greater than zero outside

5. The force between the two contacting bodies is given by an integral of pressure distribution within the contact circle with respect to area
6. The displacements and stresses must satisfy differential equations of equilibrium for elastic bodies
7. At large distances from the contact surface, stresses must vanish

Indentation between a hard, spherical indenter with a flat surface can be classified as Hertzian indentation [54]. Under the indenter a compressive stress is induced, while at the edge of the circle of contact, a tensile stress is induced [54]. The normal contact stress (p) can be calculated for a sphere in contact with a flat surface using the following equations:

$$a = \left(\frac{3Pr}{4E^*}\right)^{\frac{1}{3}} \quad \text{(Equation 11)}$$

$$p_m = \left(\frac{16E^*P}{9\pi^3 r^2}\right)^{\frac{1}{3}} \quad \text{(Equation 12)}$$

where P = applied load, E = elastic modulus, r = radius of contact, and p_0 = maximum contact stress. Where E^* is the equivalent elastic modulus, defined by the following equation:

$$\frac{1}{E^*} = \left[\frac{1-v_1^2}{E_1}\right] + \left[\frac{1-v_2^2}{E_2}\right] \quad \text{(Equation 13)}$$

Where $\boldsymbol{\nu_1, E_1}$ and $\boldsymbol{\nu_2, E_2}$ are the Poisson's ratio and elastic modulus of the indenter and sample surface, respectively.

2.5 Fracture Mechanics

There are three modes of cracking in materials; opening of crack faces, sliding mode, and out of plane (tearing) mode [55]. These modes are designated "Mode I", "Mode II", and "Mode III" respectively for the previously mentioned definitions [55], and can be seen in Figure 2-5.

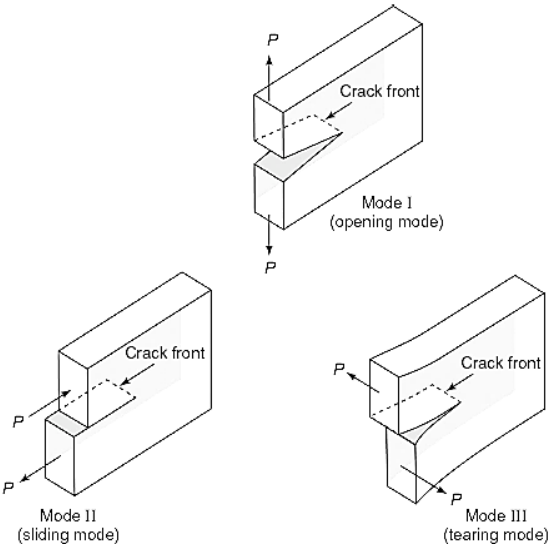

Figure 2-5 A schematic of the three modes of cracking in materials [56]

2.5.1 Types of Cracks

Fracture, or failure, of a coating depends on the following [57]:

- hardness
- toughness
- elastic modulus
- stress applied
- flaw size and density
- loading conditions
- indenter geometry and
- thickness of the coating

Typically, under lower applied loads, the coating controls the response to deformation. However, under higher loads, the substrate plasticity dominates the response, due to the fact that the quasi-plastic zone moves from the coating to the substrate [57]. In thin coatings, the quasi-plastic zone lies within the substrate, therefore the substrate plasticity dictates the damage mode. However, in thick coatings, the quasi-plastic zone lies within

the coating and thus fracture dominates the response to loading [57]. Coatings with intermediate thickness have shown radial cracks initiating at the bottom of the surface due to coating flexure [57].

Different types of cracks that will be discussed below include cone, radial, median, half-penny, and lateral. These crack types have been extensively studied in glass. Cone cracks are generated by elastic loading of spherical or flat-punch indenters **[57, 58, 59]**. Initially, a ring crack at the external boundary surface of contact nucleates. The crack then spreads away from surface at characteristic angle relative to load axis **[57, 58]**. Should there be a large mismatch in elastic modulus between the indenter and the substrate, there is potential for deviation in crack trajectory **[59]**. An example of a Hertzian cone crack can be seen in Figure 2-7. Hertzian fracture is a result of tensile stress acting in the radial direction near the contact circle. This results in the formation of cone cracks, discussed below. The geometry of a Hertzian cone crack can be found in Figure 2-6.

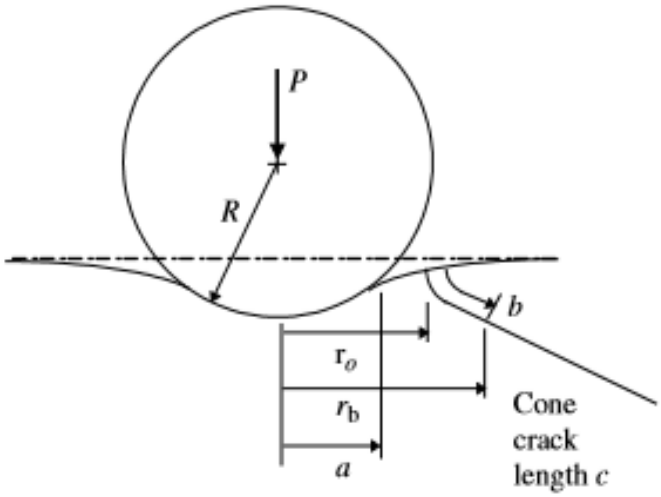

Figure 2-6 Geometry of Hertzian cone crack [53]

The maximum tensile stress required to produce Hertzian cracks is given by equation 14, while the maximum tensile stress outside of the circle of contact is given by equation 15 [53, 54]. The mean contact pressure, also known as the indentation stress is defined below by equation 16, where P = applied load, a = radius of circle of contact, R=indenter radius [60].

$$\sigma_{max} = (1 - 2v)\frac{P}{2\pi a^2} \quad \text{(Equation 14)}$$

$$\sigma_{max} = \left(\frac{(1-2v)}{2\pi}\right)\left(\frac{4E^*}{3}\right)^{\frac{2}{3}} P^{\frac{1}{3}} R^{-\frac{2}{3}} \quad \text{(Equation 15)}$$

$$p_m = \frac{P}{\pi a^2} = \left[\frac{4}{3}\frac{E^*}{\pi}\right]\frac{a}{R} \quad \text{(Equation 16)}$$

The a/R term refers to the indentation strain. Even if indentations are made with indenters of different radii, if a/R is equivalent, no differences can be distinguished [53]. The relationship between the mean contact stress and the indentation stress can define a stress-strain response similar to that obtained from a typical uniaxial test. Due to the fully elastic nature, the relationship between the mean contact pressure and the indentation strain is linear. However, due to localized nature of the indentation stress field, the elastic-plastic response proves to be more complex [53].

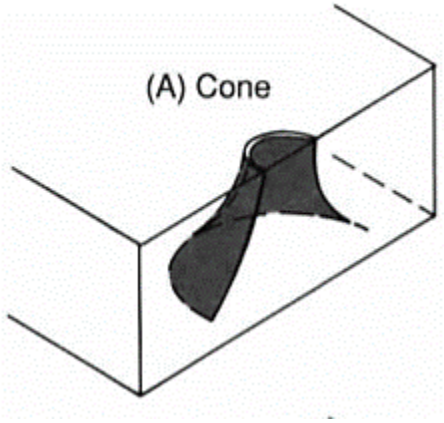

Figure 2-7 Schematic of Hertzian cone crack [58]

Radial cracks, which typically occur in materials that are tougher than glass [59], are generated by excessive loading of blunt indenters (e.g. Vickers diamond indenter) and form parallel to load axis [57, 58, 59]. These particular cracks lead to the generation of plastic impressions in surface (elastic-plastic contacts), and typically spread from edge of contact impression corner while remaining close to the surface [57, 58, 59]. Secondary radials spread out from edge of contact impression adjacent to indentation corner and propagate

into surrounding material while remaining close to the surface [58]. These cracks are driven by tensile hoop stress [59], and can be seen in Figure 2-8.

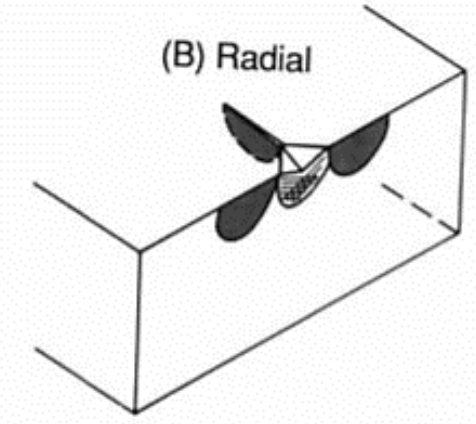

Figure 2-8 Schematic of radial cracks [58]

Median cracks are generated beneath plastic deformation zone at an elastic-plastic contact and form full circles/circular segments that have been truncated by deformation zone boundary or materials surface [57, 58, 59]. These cracks form due to a wedging action [59]. They propagate parallel to the loading axis [57, 58]. A schematic of median cracks can be seen in Figure 2-9.

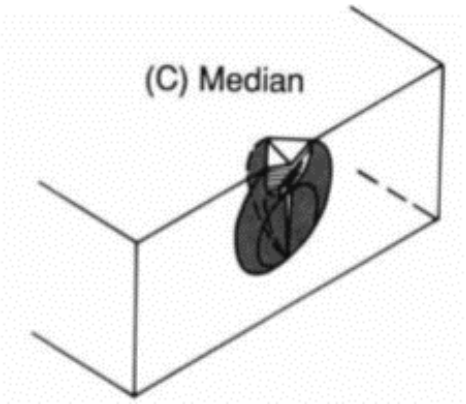

Figure 2-9 Schematic of median cracks [58]

Half-penny cracks are the final morphology of median cracks. Half-penny cracks are formed by either median growth toward surface, radial propagation downward, or

coalescences of the two [57, 58, 59]. These particular cracks form on unloading [57, 59] and can be seen in Figure 2-10 .

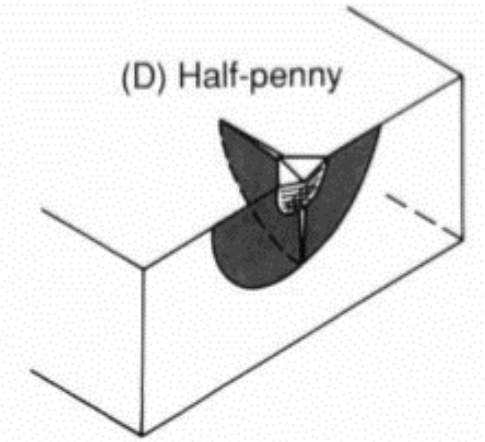

Figure 2-10 Schematic of half-penny cracks [58]

Lateral cracks run parallel to the surface and are generated beneath the deformation zone [57], [58], [59]. Laterals then turn up towards the surface, forming a chip [59]. Lateral cracks are circular, and shallow [58]. These types of cracks are generated at edge of contact impression [57], [58]. Laterals are typically bounded by radial or secondary radial cracks [58]. While they typically start on unloading, there is evidence of their generation during cyclic loading in tough materials [59]. This particular type of crack has been found to be responsible for abrasive wear and erosion of ceramics and ceramic coatings [59]. An example of deep and shallow lateral cracks can be seen in Figure 2-11.

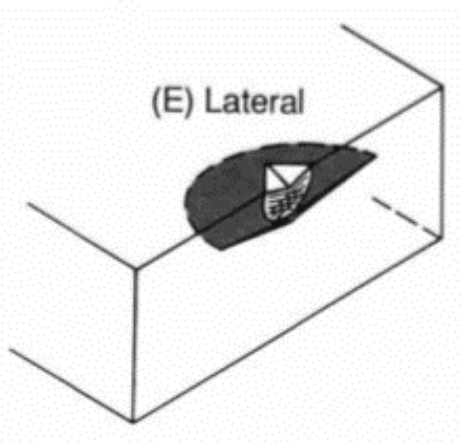

Figure 2-11 Schematic of lateral crack

2.5.2 Delamination

Delamination is another failure mode that often occurs in coatings, defined by O'Brien and Raju as "…a crack that forms between adjacent plies". [55]. An example of a delaminated coating can be found in Figure 2-12, where the coating has de-bonded from the substrate due to some sort of shear stress at the coating interface.

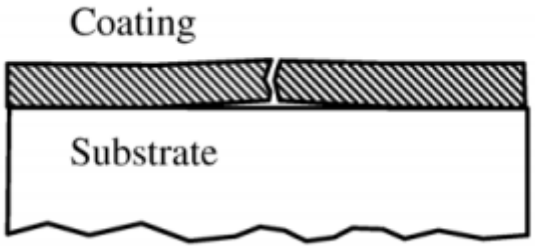

Figure 2-12 Example of delamination of a coating from a substrate

This type of failure is a crack that occurs at the interface between anisotropic materials, caused by interlaminar stresses [55]. This mixed mode fracture typically occurs at stress free edges as a result of layer mismatch, at particularly thick regions, and at regions subjected to bending out of the plane [55]. In thin films, such as coatings, debonding is a three-stage process, likely caused by some sort of property mismatch between the film and the substrate [61]. The three stages, given by [61], are as follows:

1) Initiation
2) Steady-state propagation and
3) Final transient

Yu states that the effects of modulus mismatch play a significant role in buckling of the film, which becomes even more pronounced when the substrate is more ductile than the film [61], which is the case for the coatings studied in this thesis. Thermal expansion mismatch on the other hand results in edge delamination, due to high amounts of compressive stresses that generate on cooling [61].

2.6 Wear Behaviour

Wear is defined by Budinski as the "progressive loss or damage of a solid surface caused by contact with another solid" [62]. There are many different wear mechanisms, some of which will be discussed below. These include abrasive wear, adhesive wear, and erosion of monolithic materials. For the case of composite materials, particularly the composite coatings discussed in this paper, the mechanisms become more difficult to analyze. This will be discussed in the final section.

2.6.1 Monolithic Materials

Abrasion is a form of wear that occurs when a material is in sliding contact with a harder material [62]. This can occur through several different mechanisms, including cutting, fracture, fatigue and grain pullout. These mechanisms are illustrated in Figure 2-13.

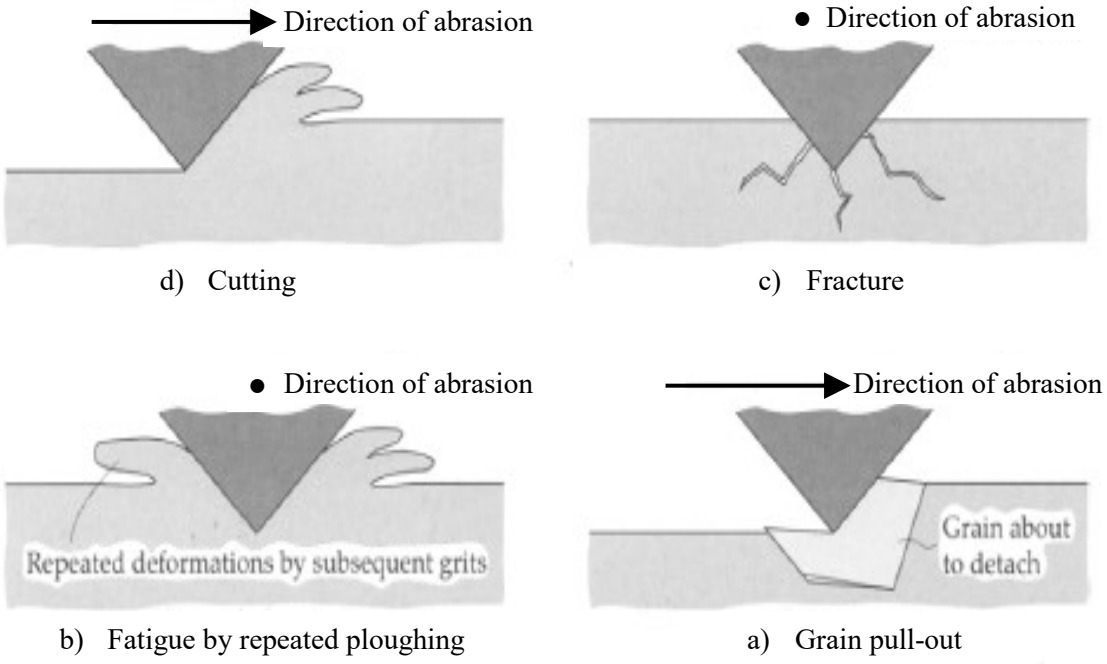

Figure 2-13 Abrasion mechanisms: a) cutting, b) fracture, c) fatigue by repeated ploughing, and d) grain pull-out [63]

Cutting, as the name implies, is a result of a hard asperity cutting a softer surface and involves the generation of wear debris [63]. Fracture occurs in the case of contact with a brittle material [63]. Fatigue occurs when the softer material comes into contact with the harder material repeatedly, resulting in a ploughing effect, or plastic deformation of material [63]. The final mechanism, grain pull-out, mainly occurs in ceramics and will not be discussed in detail [63].

Adhesive wear in a result of rubbing contact of asperities, which results in fusion of the two asperities. As the harder material slides over the softer material, the softer material is removed in the form of wear debris [62]. The wear rate due to adhesion wear can be determined through Archard's wear law below:

$$W = \frac{kLD}{H} \qquad \text{(Equation 17)}$$

Where W=wear rate, k = constant, D= sliding distance, L=applied load, and H= hardness of the softer material [62].

Erosion occurs when a surface is impacted by particles in a solid or liquid environment. In the case of solid particles, the mechanism is similar to abrasion, however if the erodent is a liquid, then the mechanism changes [63]. Erosion is highly dependent on the angle of impingement of particles, and the velocity at which they are bombarding the surface [63]. Figure 2-14 shows the relationship between the severity of erosion and the angle of impingement of solid particles. The dotted line (a) represents erosion of ductile materials, while the solid line represents erosion of brittle materials (b). In the case of ductile materials, the most detrimental effects occur at an angle of 30°, which can be correlated to elbows or bends in pipelines [64]. Brittle materials on the other hand experience the highest erosion rates at 90°, meaning that any impingement directly at the material will result in higher material removal rates [64].

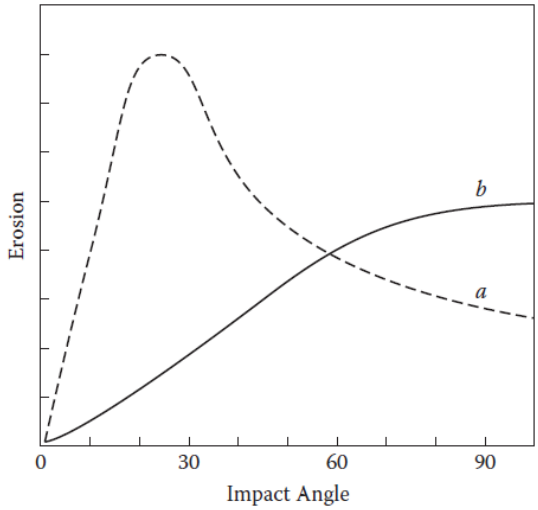

Figure 2-14 Effect of impact angle on erosion [62]

Particle shape has significant influence over the erosion mechanism and the amount of material removed. In particular, for spherical shaped impact particles, it has been found in the literature that ductile materials exhibit lower material removal rates in comparison to those found for brittle materials under impact of the same spherical particles [65]. For protective coatings, which tend to be hard and wear resistance, yet brittle, crack initiation and propagation tend to be the dominant failure mechanism in erosive conditions [66]. Particles impacting the surface at low velocities are less problematic in comparison to

particles impacting at high velocities, due to the fact that at low velocities it is less likely that plastic deformation will occur [63].

Erosion mechanisms are complex and can be difficult to determine. Many models have been proposed in order to try to predict the mechanism of erosion, with most being classified as either “ductile” or “brittle”. With ductile materials such as steel or aluminum, cutting and ploughing tend to be the dominant erosion mechanisms [67]. Material pile-up is also typically seen. This material is displaced to form a lip or crater, rather than actually being removed [68]. This lip formation is a result of the formation of shear band(s) [68, 69]. In solid particle erosion, repeated impact on shear bands results in material removal [68]. On the other hand, brittle materials tend to fracture, similar to mechanisms seen with indentation.

2.6.2 Composite Materials

Most models used to analyze wear in composites are simplified and thus are not completely accurate in predicting the wear mechanisms. Therefore, there is not a complete understanding of how the reinforcing particles affect the material [70]. Shen and Chawla found through their work with indentation that as an indenter comes into contact with a composite surface, the concentration of particles with increase in the deformation zone. This is illustrated with SiC particles in an aluminum matrix in Figure 2-15. This locally increases the hardness, and the amount of stress applied to the matrix itself is reduced [71].

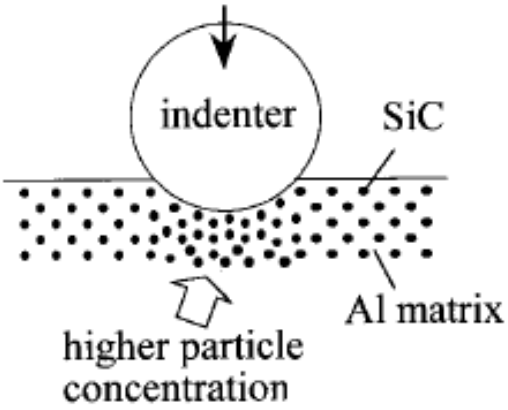

Figure 2-15 Particle concentration directly beneath indenter in particle reinforced metal matrix composite [71]

In the case of brittle materials, such as EN coatings, the wear mechanism is a function of the toughness of the material [70]. Therefore, in order to improve the wear resistance, a tough secondary phase must be added in order to reduce the probability of fracture and wear [70]. Toughening of brittle materials using ductile phase reinforcements can be achieved through several mechanisms including; micro-cracking, crack bridging, crack deflection, crack arresting, and transformation toughening [72, 73, 74, 75, 76, 77, 78]. mechanisms have been found to increase the energy required for propagation of cracks, subsequently increasing the fracture toughness of the material being toughened.

The addition of a ductile phase to a brittle matrix allows for the absorption of crack propagation energy such that the crack loses driving force. Micro-cracking can allow for the reduction of stress adjacent to the crack tip, reducing the overall driving force [79]. Micro-cracking has been found to also increase fracture toughness by reducing major cracks to a series of micro-cracks [80]. The addition of a second phase particle serves to break up larger cracks into smaller ones.

Crack bridging is commonly seen in reinforced composites, where again the propagation energy is significantly increased upon interaction with a second phase. Bridging involves the plastic deformation of the reinforcement upon contact with a crack. In order to continue, the crack must pass through the second phase [81, 82]. Once the crack hits the ductile reinforcement, it absorbs the crack energy and the crack is less severe as it continues to propagate [74, 83]. This mechanism can be seen illustrated in Figure 2-16. It was found

through work done by Jin and Chen that SMA fibers situated directly behind a crack tip optimize the opportunity for crack closures and aid in closure of mode I cracks [84].

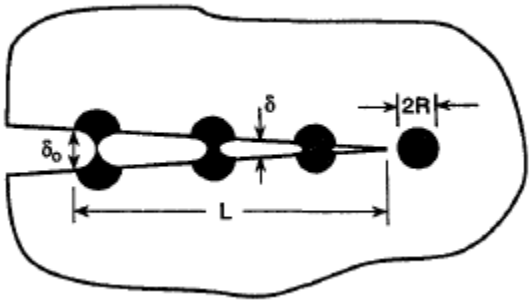

Figure 2-16 Crack bridging due to ductile particles in a brittle matrix [83]

A similar mechanism is crack deflection, which involves the absorption of the crack driving force by changing the direction of propagation [85], whereas crack arresting stops the crack altogether. Crack deflection involves the interaction of a second phase particle with a propagating crack. When the crack comes into contact with a particle or fibre, the crack path must change its path, which requires energy, thus reducing the energy at the crack wake [86, 87].

Inhomogeneities in the microstructure due martensitic transformations, such as that occurring under an applied stress in superelastic NiTi, can aid in deflection of cracks [75, 88]. When a crack attempts to propagate, stress concentrations are highest at the crack tip. When these high stresses approach a superelastic particle, a transformation from austenite to detwinned martensite occurs, accompanied by a change in volume. This results in an increase in compressive stresses at the crack tip which reduce the tensile stresses involved in the crack propagation and subsequently the stress intensity factor at the crack tip [88]. Transformation toughening will take place provided that the applied stress (mean contact stress) is greater than that required in initiate the martensitic transformation.

3 Methodology

3.1 Material Characterization

3.1.1 Substrate

API X100 pipeline steel 16 mm discs having 6 mm thickness were used as substrates for all scratch, indentation, and erosion experiments. High amounts of Mn, C and Si are present in the steel, with minor amounts of Ti, V, and Cr as shown in Table 3-1. In order to determine the microstructure of the substrate, a steel sample was etched with 5% Nital etchant and examined using OM. For bend test experiments, steel sheets having 0.6 mm thickness, 20 mm width and 50 mm length were used as substrates. The low carbon steel sheets had a hardness of 60 HRC. These sheets were also etched using Nital and examined using OM.

Table 3-1 Elemental composition of API X100 steel substrate [89]

Element	Ti	C	Si	V	P	Mn	Cu	Cr	Fe
Wt.%	0.018	0.103	0.121	0.036	0.010	1.221	0.009	0.070	Balance

3.1.2 Second Phase Particles

Commercial superelastic 60 nm NiTi powder from US Research Nanomaterials Inc. was used as a second phase particle. Using a particle absorption index of 0.1, the size distribution was analyzed using laser diffraction. Inductively coupled plasma spectroscopy was used in order to confirm the chemical composition of the powder. The superelastic NiTi powder was first dissolved in aqua regia and then examined using inductively coupled plasma optical emission spectrometry (ICP-OES). Hitachi S-4700 Scanning Electron Microscope was used to qualitatively confirm the relative distribution found using particle size analysis.

3.1.3 Single Particle Erodent Particles

WC-Co particles having a nominal 1 mm diameter were used as erodent particles for single particle erosion tests. Hardness value of the WC-Co particles was rated as 75 HRC from the supplier. An area scan using EDS was done to confirm the composition of the spheres, outlined in Figure 3-1. The elastic modulus and Poisson's ratio for the erodent material has been found in the literature to be approximately 600 GPa and 0.26, respectively [27].

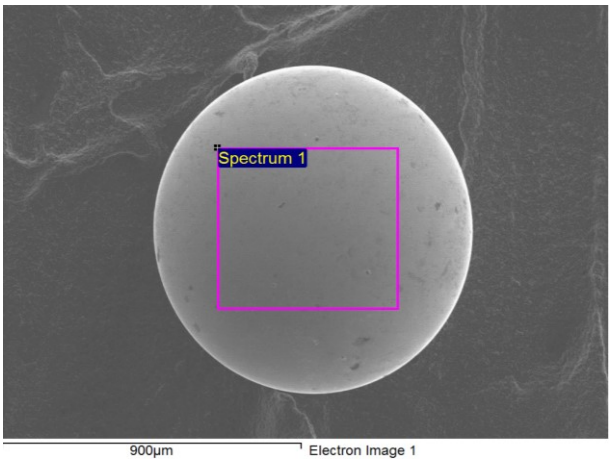

Figure 3-1 EDS scan area of WC-Co erodent particle used to determine elemental composition

3.2 Coating Procedure

3.2.1 Development of Coating Procedure

The plating process of monolithic Ni-P has been previously established and implemented, however, the addition of second phase particles can affect the plating bath composition and deposition rate. Before testing of the composite coatings could begin, it was necessary to optimize the plating procedure. Therefore, the presence of NiTi was confirmed using SEM and EDS. After it had been determined that it was possible to produce the coatings, the plating procedure had to be optimized to ensure that coatings with a uniform distribution

of particles were being produced, otherwise there could be an inhomogeneity of coating properties across the sample. The following variables were assessed to optimize the plating process:

- Use of surfactant
- Stirring method
- Concentration of particles being incorporated
- Temperature and pH

An aqueous surfactant was added to the plating bath in order to try to prevent agglomeration of nano-particles in the coating. After analyzing coating surfaces with and without surfactant, it was determined that while the surface of the samples containing surfactant were smoother than those without, there was minimal effect on particle distribution and therefore it would not be used in the production of future coatings. EDS mapping showed nearly identical distributions of Ti on both surfaces with surfactant (Figure 3-2) and without surfactant (Figure 3-3). In fact, EDS confirmed that the coating without surfactant had a higher concentration of Ti (2.56 wt.%) in comparison to the coating that had surfactant (2.38 wt.%). Therefore, the addition of surfactant was eliminated from the coating process.

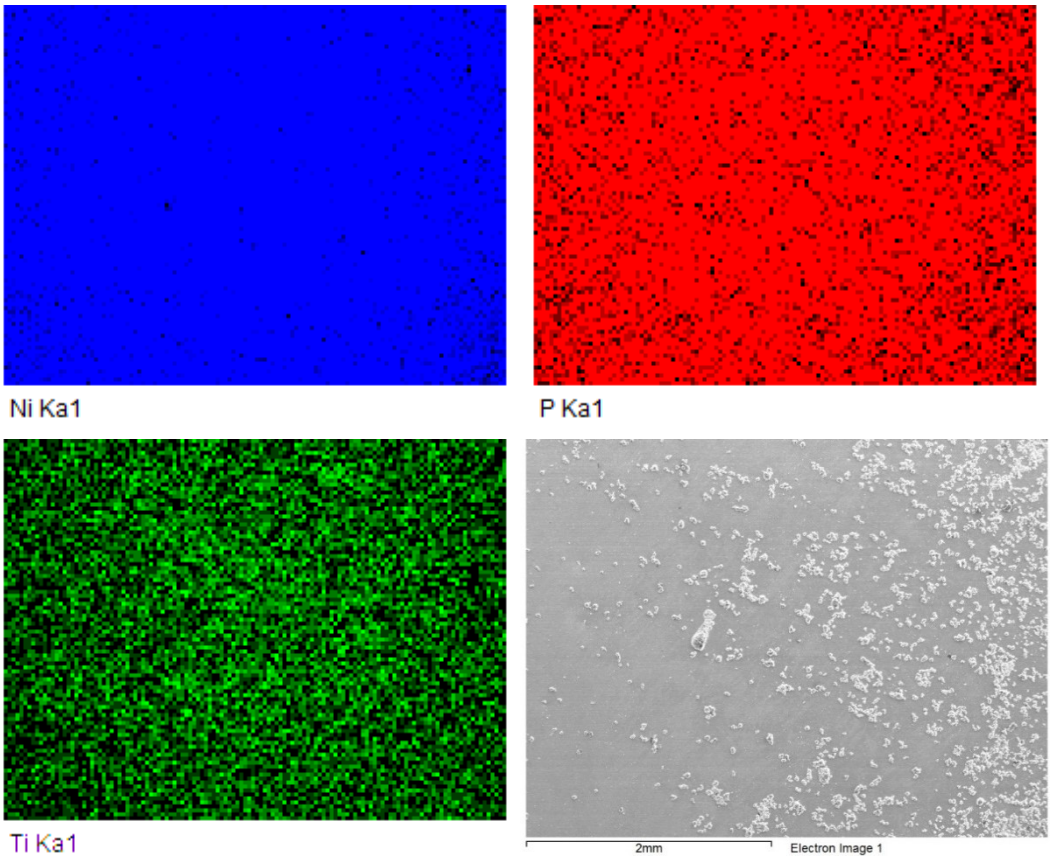

Figure 3-2 EDS Map and SEM image of Ni, Ti and P elements and surface morphology of 1 g coating surface with surfactant

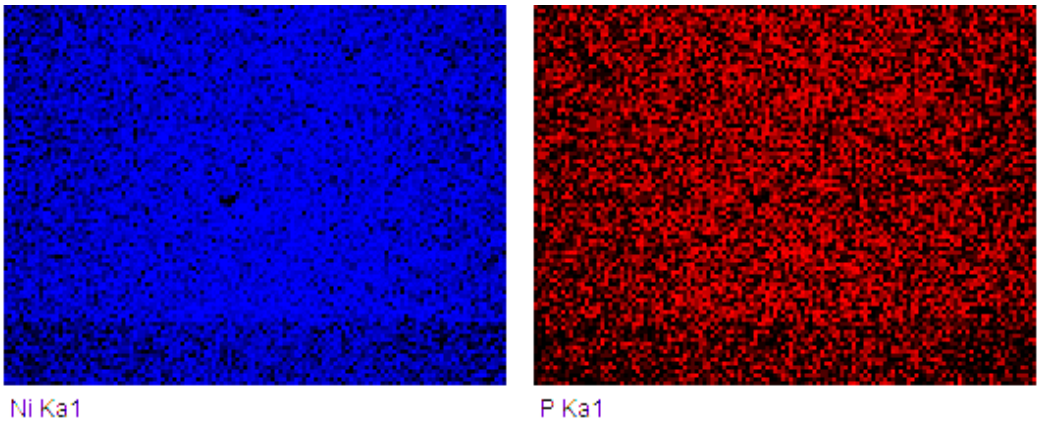

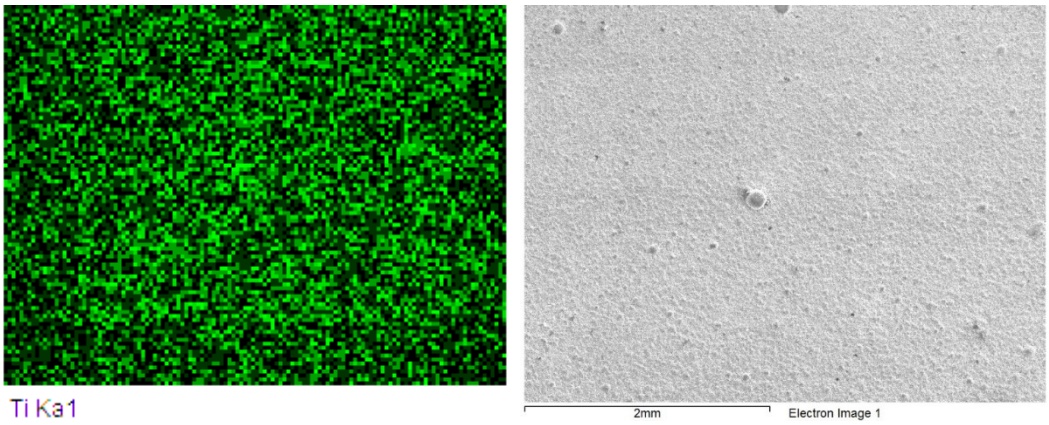

Figure 3-3 EDS Map and SEM image of Ni, Ti and P elements and surface morphology of 1 g coating surface without surfactant

In order to achieve a uniform distribution of particles within the coating matrix, it was necessary to choose a proper dispersion method during the plating process. Ultrasonic stirring and magnetic stirring were combined to achieve this dispersion. However, through SEM analysis it was determined that minimal change in dispersion was observed, and thus to simplify the coating process only magnetic stirring was used.

Temperature and pH control are extremely important to ensure not only a uniform coating but to avoid plating bath decomposition. The temperature of each plating bath was analyzed throughout the entirety of the plating process using an internal and external temperature probe. The pH was also monitored frequently throughout the duration of each coating procedure to ensure that it did not drop below desirable levels.

Composite coatings containing 0, 0.5, 1, 2, 3, 5 and 10 g nano-NiTi particles were successfully plated on low carbon pipeline steel substrates. The deposition rates of these coatings were estimated in order to gain a better understanding of how an increasing amount of NiTi in the bath affects the plating process. In order to estimate the deposition rates, coating thickness was measured using OM for all samples. 3 measurements were taken on each sample to obtain an average thickness. Figure 3-4 shows the deposition rate for concentrations of NiTi up to 10 g/L. In general, an exponential decay was seen with increasing NiTi concentrations, limiting the amount of NiTi that could be used in experimental work. As the amount of NiTi added to the plating bath increased above 3 g/L, the concentration of NiTi began to approach zero, meaning that no NiTi was being

incorporated into the matrix. As mentioned previously in Chapter 2, this trend is commonly seen in electroless Ni-P composite coatings due to particle agglomeration and saturation limiting the incorporation of any further particles. Due to the low deposition rates of the 5 and 10 g/L, these concentrations of NiTi were not pursued any further. For each experiment outlined in section 3, coatings containing 0, 0.5, 1 and 2 g NiTi were used, and plated for 2.5, 4.5, 6 and 9 hours respectively in order to achieve thicknesses ranging between 20-30 μm.

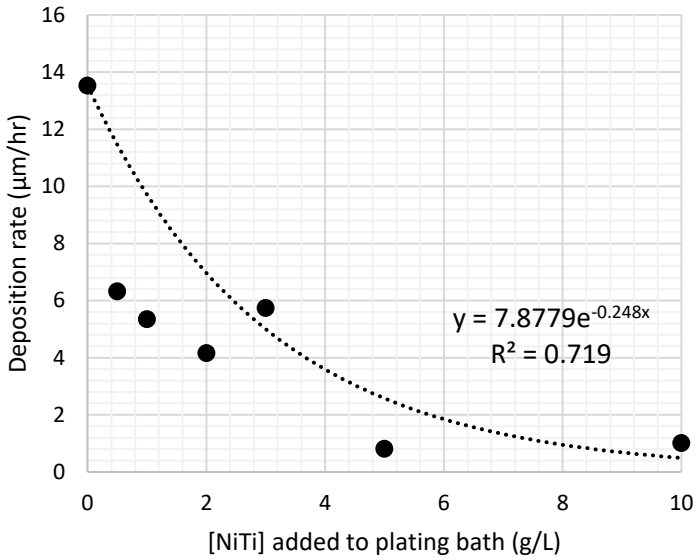

Figure 3-4 Effect of [NiTi] on coating deposition rate

3.2.2 Optimized Coating Procedure

The optimized plating process is outlined below. Each substrate was ground using 240, 320, 400, and 600 grit SiC abrasive paper and then polished using 9 μm, 3 μm and 1 μm monocrystalline diamond polish. The substrates were then degreased in acetone and cleaned in an alkaline solution at 80±5 °C. The contents of the alkaline cleaning solution used in substrate pre-treatment include 50 g/L sodium hydroxide, 30 g/L sodium carbonate, and 40 g/L sodium phosphate. Samples were then rinsed with deionized water and etched for 10 s using H_2SO_4. Samples were rinsed again with deionized water and hung

horizontally in a commercial electroless Ni-P plating bath (Figure 3-5), which contained sodium hypophosphite ($NaPO_2H_2$) as the reducing agent and nickel sulfate ($NiSO_4$) as the source of Ni. Samples were kept in the electroless bath for 30 minutes in order to form a pre-coat layer of just Ni-P. After the pre-coating, the samples were removed and put in an electroless Ni-P plating bath containing varying amounts of superelastic NiTi nano-powder. Magnetic stirring was employed at 300 RPM throughout the duration of the coating process. The temperature maintained at 88±2 °C and was adjusted accordingly. The pH was maintained between 4.8-5.2, adding NH_4OH as necessary to raise the pH.

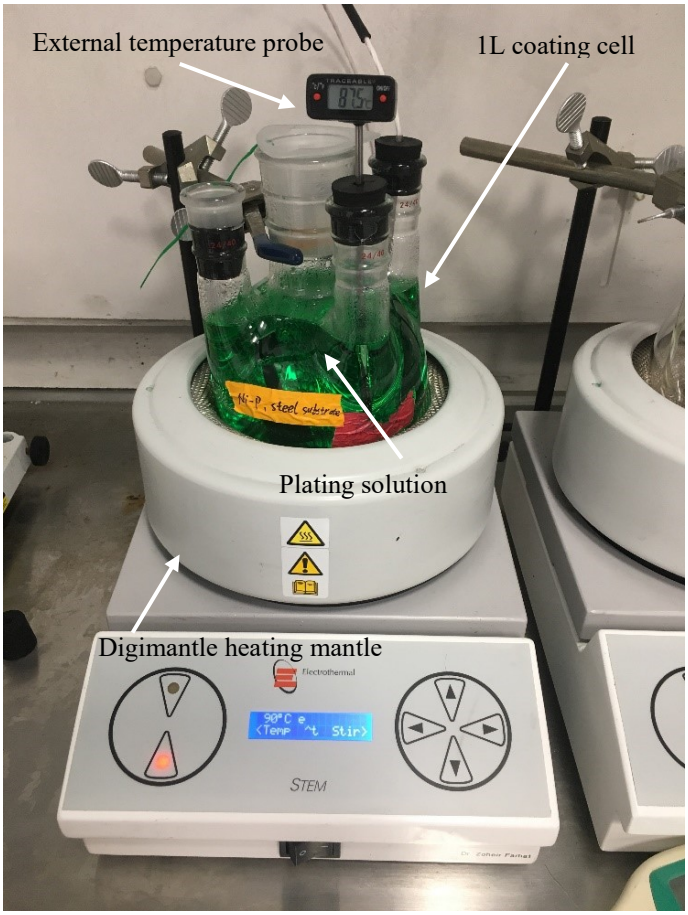

Figure 3-5 Electroless plating bath set-up used for coating samples

3.3 Coating Characterization

Samples were sectioned using Buehler isomet 1000 precision saw with CBN blade at 800 RPM and a counter load of 350 g. The phases present upon deposition within each sample were determined using a Bruker D8 Advance diffractometer. Each sample was scanned using Cu Kα radiation with a wavelength of 1.54 λ. Samples were scanned from 2θ=20-140 ° in order to ensure that all peaks would be included. Cross-sections and surfaces of each sample were examined using SEM, EDS and OM in order to determine coating thickness, integrity, morphology and wt.% NiTi in the coatings. Surface roughness was analyzed using non-contact white light profilometry. Micro-Vickers hardness was calculated by analyzing the indentations made on the cross-section of each sample to minimize the effect of the substrate, using a Micromet Vickers Hardness tester. The substrate was also tested to determine the micro-hardness. The load applied was 50 g, and the Vickers hardness (HV) was calculated using the equation below,

$$HV = \frac{1.8544F}{d^2} \qquad \text{(Equation 18)}$$

where F is the force applied (kg) and d is the average length of the diagonals of the indent (mm). An example of an indent on the coating cross-section can be seen in Figure 3-6. Prior to scratch, indentation and erosion testing, each coated sample was ground using 600 grit SiC and polished using 9 μm, and 3 μm monocrystalline diamond polish.

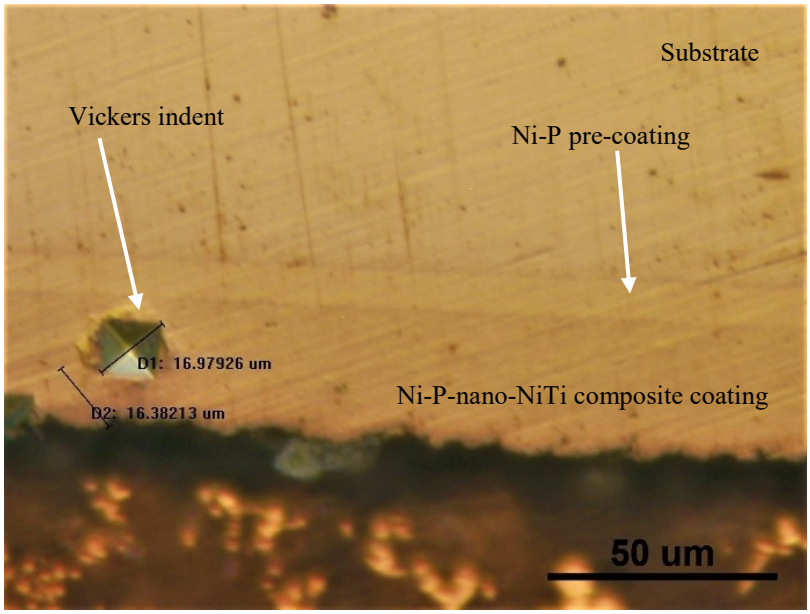

Figure 3-6 Optical micrograph showing micro-Vickers indent on coating cross-section with diagonal measurements

3.4 Scratch Testing

Monolithic Ni-P and Ni-P-nano-NiTi composite coatings were subjected to scratch testing under constant and increasing load conditions using a Universal Micro Tribometer (UMT). Each sample was scratched with a spherical diamond tip indenter, with a radius of 200 μm. The testing conditions used are listed in Table 3-2. For each test the sliding speed was 0.17 mm/s. Scratch distances were 5 mm and 10 mm for the constant load and increasing load, respectively. After testing, wear tracks were analyzed using optical microscopy, SEM, and profilometry in order to analyze wear mechanisms and volume loss. Crack initiation and propagation were monitored during testing using an acoustic emission sensor (1283 USB AE Node AE sensor).

Table 3-2 Scratch testing conditions

Test Conditions	Loads Applied (kg)	# of Passes
Constant Load	0.5, 1, 2, 4	1
Increasing Load	0.05-4.5	1
Constant Load	2	5, 10, 20, 40

Volume loss was calculated using equations 19-21 from ASM volume 18 based on the indenter radius and the scar width.

$$b = D\ \sin(\frac{\theta}{2}) \quad \text{(Equation 19)}$$

$$\theta = 2\arcsin\frac{b}{D} \quad \text{(Equation 20)}$$

$$V = \frac{D^2 t}{8}[2\arcsin\frac{b}{D} - \sin(2\arcsin b/D)\ ] \quad \text{(Equation 21)}$$

Where b = scar width, D = diameter of indenter, and t= scar length [90].

3.5 Micro-indentation Testing

Each sample was subjected to indentation using a PASCO ME-8236 miniature test frame (Figure 3-7) in order to determine the effect of powder concentration in the coating on indentation behaviour and crack formation. Samples were subject to the following loads: 600 N, 1000 N, 1500 N, 2000 N, and 2500 N, all at a loading rate of 2 mm/min. Indentation tests were carried out using a spherical WC-6Co spherical indenter. An acoustic emission sensor was attached onto the coated sample in order to measure cracking events. Each sample was analyzed using OM and SEM to examine the indents. Samples subjected to 2500 N load were sectioned and the cross-sections were examined using OM and SEM.

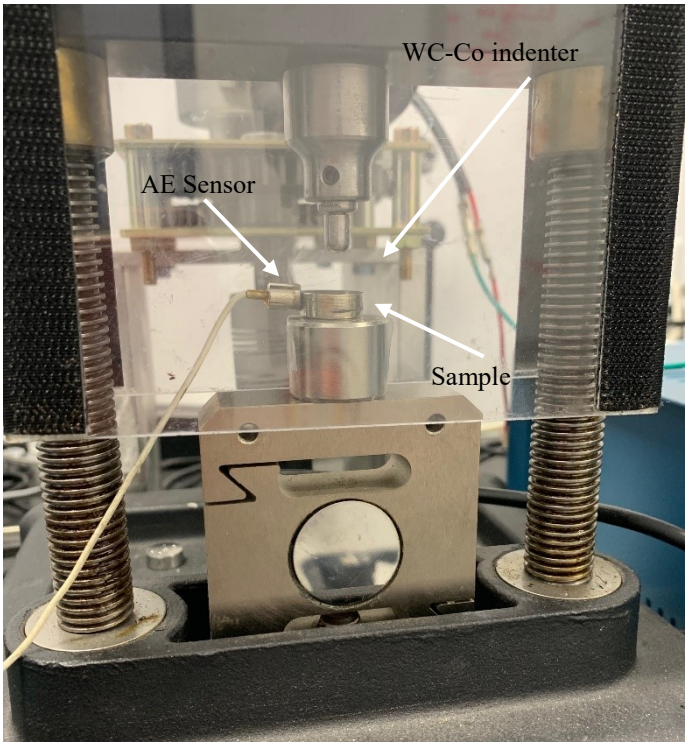

Figure 3-7 PASCO ME-8236 miniature test frame set up for indentation testing

3.6 Single Particle Erosion Testing

Coated samples were tested under several different conditions using a single particle erosion tester in order to gain an understanding of the effect of impact angle and particle speed on the erosion mechanisms. Each sample was tested at angles of 30 °, 45 °, 60 °, and 90 °. The samples were tested at low pressures (30 psi) and high pressures (60 psi).

A schematic of the apparatus used for the experiments can be found in Figure 3-8. The system is driven by a compressed air supply, of which the pressure is adjusted to vary the velocity of the particle. Air is fed to the system by means of an actuation mechanism that is triggered by a button. This results in the opening of a solenoid valve which allows air to flow through the system and drive the particle down a polycarbonate barrel. The angle at which the target sample was at was varied using the sample holder.

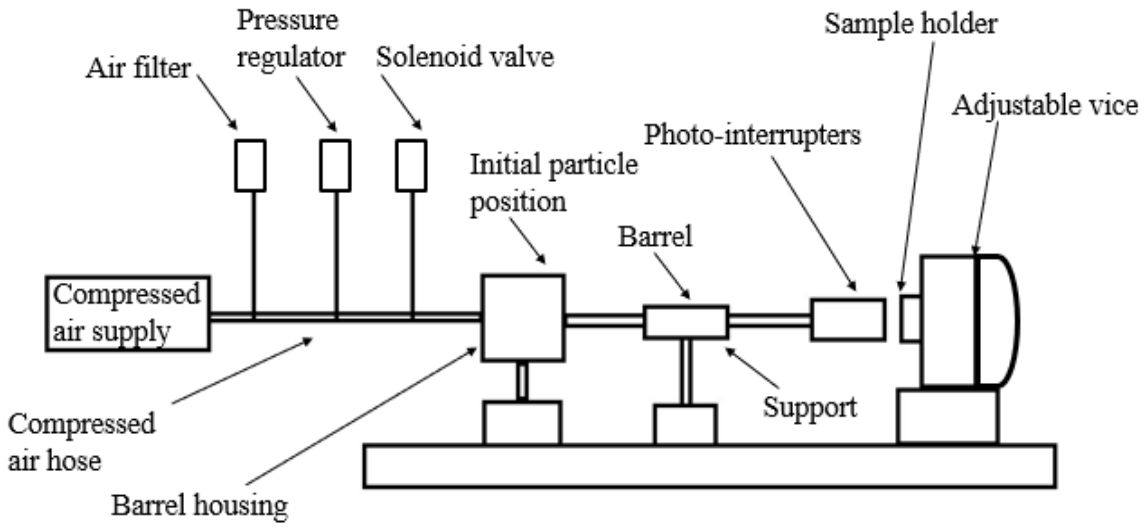

Figure 3-8 Schematic of set-up used for single particle erosion testing

Two photo-interrupters were placed at the end of the barrel, 3 cm apart. By measuring the time required for the particle to travel between the two photo-interrupters (PIs), the speed can be calculated using equation 22. A speed calibration curve was formulated by assessing the speed at pressures varying between 20-60 psi (Figure 3-9). As seen in the figure, testing pressures for this work correspond to average velocities of 35$\pm$ 3 m/s and 52 $\pm$ 4 m/s.

$$u\left(\frac{m}{s}\right) = \frac{\text{distance between PIs(m)}}{\text{time for projectile to pass both PIs (s)}} \qquad \text{(Equation 22)}$$

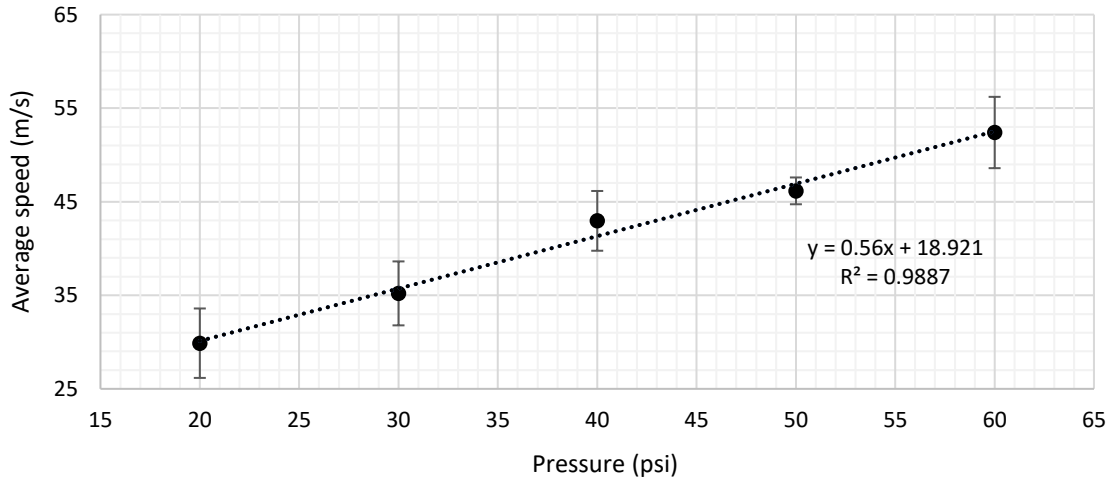

Figure 3-9 Speed calibration curve as a function of testing pressure

By assuming ideal conditions, the force of the particle can be estimated using equations 23 and 24:

$$W = Fd \quad \text{Equation (23)}$$

$$E_k = \frac{1}{2} m_p v^2 \quad \text{Equation (24)}$$

Where W is the work done creating the impact crater, F is the force, d is the distance that the particle travels, E_k is the kinetic energy of the particle based on the mass (m_p) and the velocity (v). Assuming that all kinetic energy is transformed into work that is done to create the impact crater, the impact force was found to range between 0.016-0.036N for velocity conditions 35-52 m/s respectively.

Impacted samples were examined using OM and SEM in order to determine erosion mechanisms and to investigate for toughening mechanisms. Crater depths and line profiles were examined using confocal laser microscope to determine volume loss and erosion mechanisms. Figure 3-10 shows an example of the line profile taken for the normal impact site of the 7.02 wt.% NiTi coating. For low angle impacts, the cross section was taken to be along the impact direction.

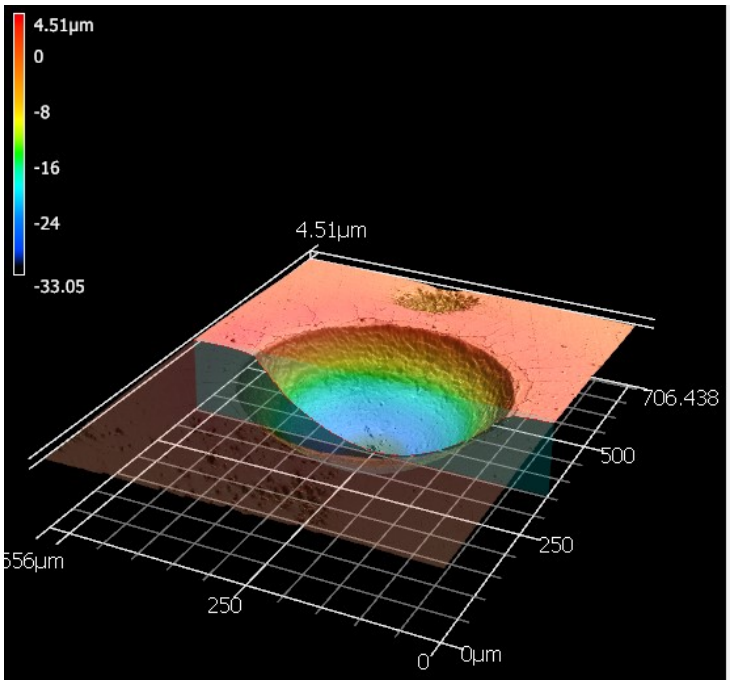

Figure 3-10 Example of line profile taken to produce depth profiles for each indent

3.7 Bend Testing

In order to measure the mechanical properties of the Ni-P monolithic and Ni-P-nano-NiTi composite coatings, three-point bend testing was performed using a PASCO ME-8237 miniature test frame (Figure 3-11). Supports spanned 40 mm apart, with the load being applied at ½ the span. Fracture events were monitored by using an AE sensor which was attached to the bending accessory to record transient elastic wave outputs during the test. Samples were placed such that the coatings were in tension during the test (i.e. not in contact with the bending accessory). All samples were placed such that the coating was in tension during testing, the configuration of which can be seen in Figure 3-12.

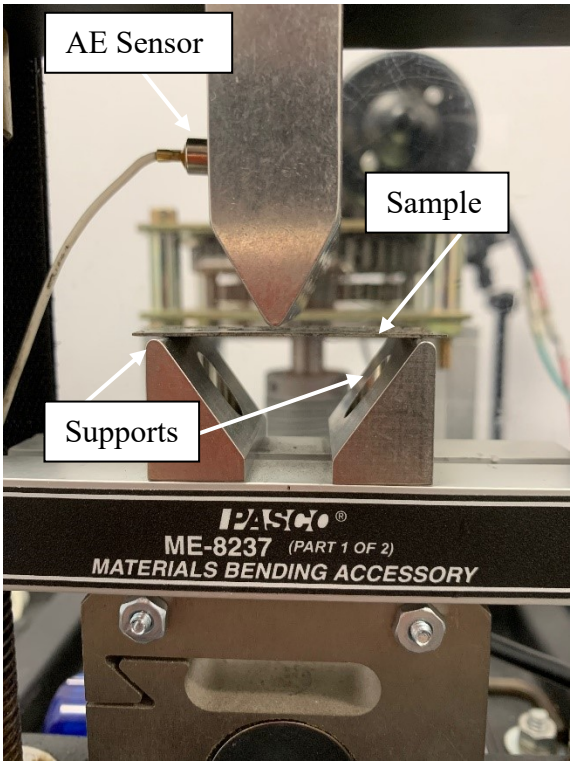

Figure 3-11 Three-point bend test set-up

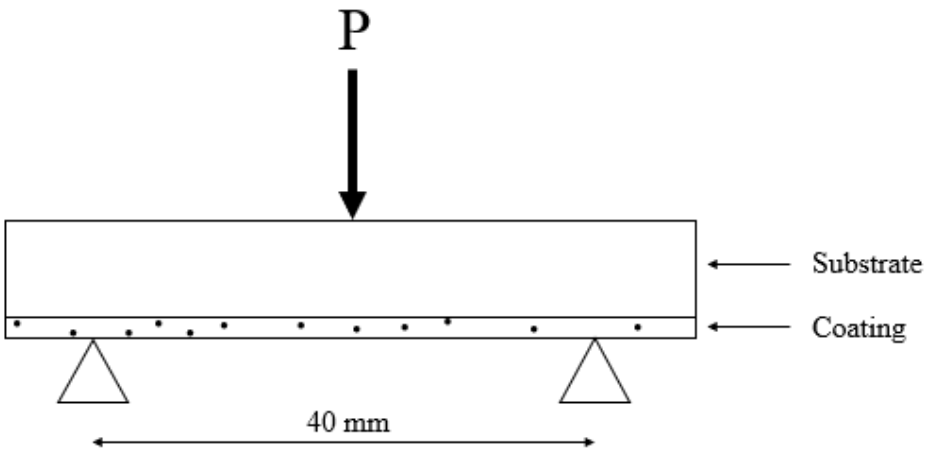

Figure 3-12 Bend test sample configuration

The elastic modulus of the bulk material is calculated using the slope of the elastic portion of the force displacement curve (k) generated during bending and the span between the supports (l) [91]:

$$E_b = \frac{l^3 k}{4b(H+h)^3}$$ Equation (25)

Where H is the thickness of the substrate, h is the thickness of the coating, and b represents the width of the sample. Bend strength can be analyzed by using equation 26 below:

$$\sigma_b = \frac{3Pl}{2b\,(H+h)^2}$$ Equation (26)

Where P is the load at the highest displacement during testing. Acoustic emission was monitored, and energy data was collected during testing in order to examine cracking events. Samples were tested at a speed of 2 mm/min until displacement reached 2.5 mm. Cracks were analyzed using OM.

4 Results and Discussion

4.1 Materials Characterization

4.1.1 Substrate

The steel was found to have a hardness of approximately 1.95 GPa through micro-Vickers indentation. An optical image of the steel disc microstructure can be found in Figure 4-1 (a). OM showed evidence of relatively equiaxed ferritic and bainitic grains for the API X100. The composition of the low carbon steel sheets was confirmed using ICP-OES and can be found in Table 4-1. The OM showed evidence of elongated ferritic and bainitic grains with carbide precipitates (Figure 4-1 (b)).

Table 4-1 Composition of bend test substrate found using ICP-OES

Element	Fe	C	S	Cu	Mn	Al	Ni	Trace elements
Wt. (%)	97.231	0.172	0.005	0.1077	0.4132	0.0294	0.0324	Balance

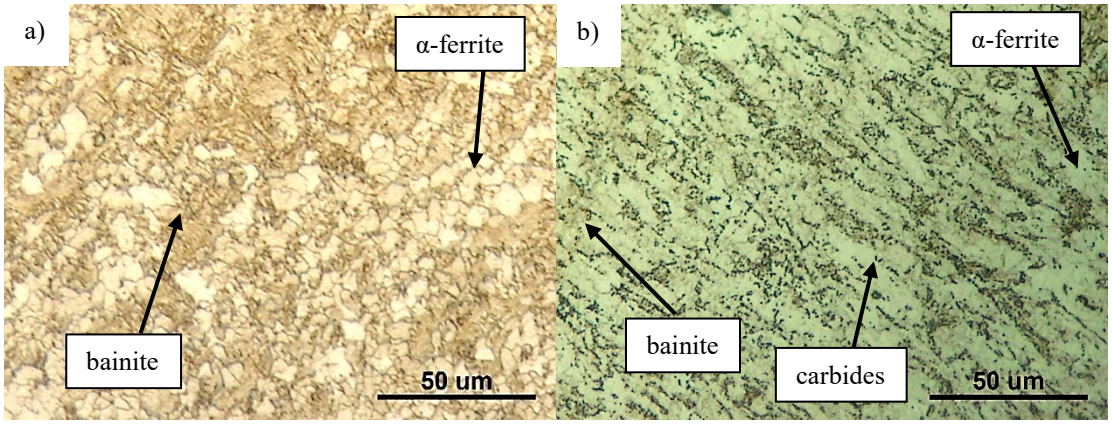

Figure 4-1 a) API X100 steel substrate for disc samples and b) low carbon steel substrate for bend samples

4.1.2 NiTi Powder

A roughly tri-modal distribution of NiTi particle size was found using laser diffraction (Figure 4-2). The volume density corresponding to these peaks was approximately 3.3 %, 2.1 %, and 3.6 % at respective size classes of 0.01-0.1 µm, 0.3-2 µm, and 3-11 µm. The D10, D50 and D90 values were found to be 0.0218 µm, 1.06 µm, and 9.51 µm respectively, giving a span of 8.992.

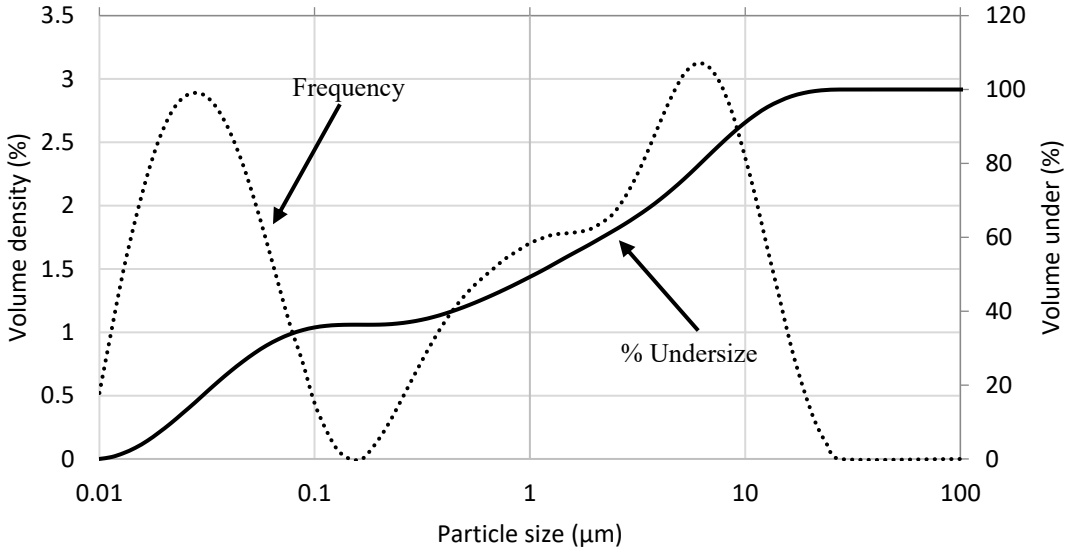

Figure 4-2 Particle size distribution

ICP-OES results can be seen in Table 4-2. It was found that the powder is NiTi-rich, containing approximately 53 wt.% Ni, and 40.25 wt.% Ti. Minor amounts of In, Sn, S and Cu were also present in the powder.

Table 4-2 Chemical composition of NiTi as received powder from ICP-OES

Element	Ni	Ti	In	Sn	S	Cu	Trace element
Wt. (%)	53.02	40.25	1.08	0.92	0.20	0.10	Balance

Figure 4-3 shows the powder morphology of the as received powder. The NiTi powder is spherical, with a wide size distribution as previously determined from particle size distribution results.

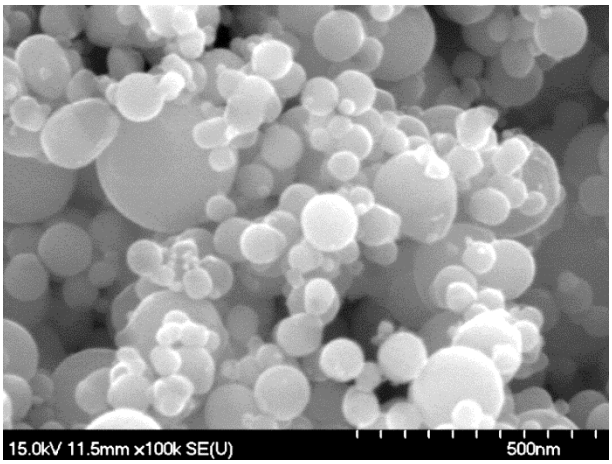

Figure 4-3 As received powder morphology showing wide size distribution and spherical morphology

4.1.3 Erodent Particle

The composition of WC-Co particles used for SPE was found to be 6%Co, with the remainder being WC (Table 4-3). Particle shape was confirmed to be spherical, as shown in Figure 4-4.

Table 4-3 Elemental composition of WC-Co particles used for SPE

Element	**C**	**Co**	**W**
Wt. (%)	14.33	6.21	79.45

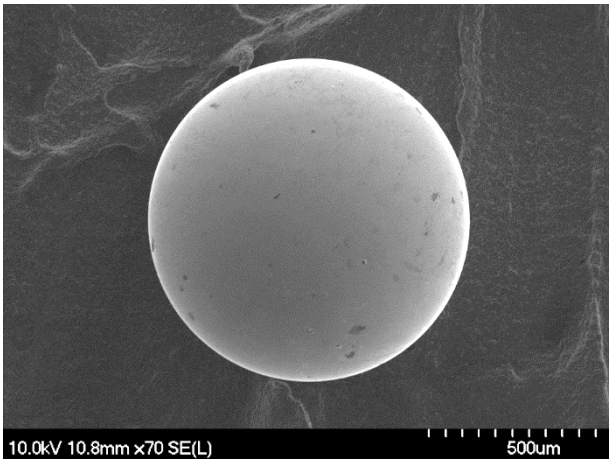

Figure 4-4 SEM image of WC-Co erodent particle

4.2 Coating Quality

4.2.1 Coating Composition

XRD traces were generated in order to identify peaks causing diffraction in each sample, which can be found in Figure 4-5. The steel substrate diffracts from the (110) and (200) Fe peaks. Diffraction patterns were also generated for the as received powder, which showed presence of superelastic, austenitic NiTi diffracting from the (110) plane. The monolithic Ni-P coating was amorphous, showing a broad peak at $2\theta = 44.506$ °. These findings are consistent with those in the literature [89, 92, 93]. Each coated sample showed evidence of an amorphous Ni-P matrix microstructure and presence of superelastic cubic NiTi diffracting at an angle of $2\theta = 42.508$ ° from the (110) plane as given by Ti0.92Ni1.08 (54 at. % Ni, 46 at. % Ti) powder diffraction file (PDF ID: 04-017-0804). Other phases in the composite coatings are difficult to detect as many of the Ni, NiTi and Fe peaks overlap and occur at low intensities.

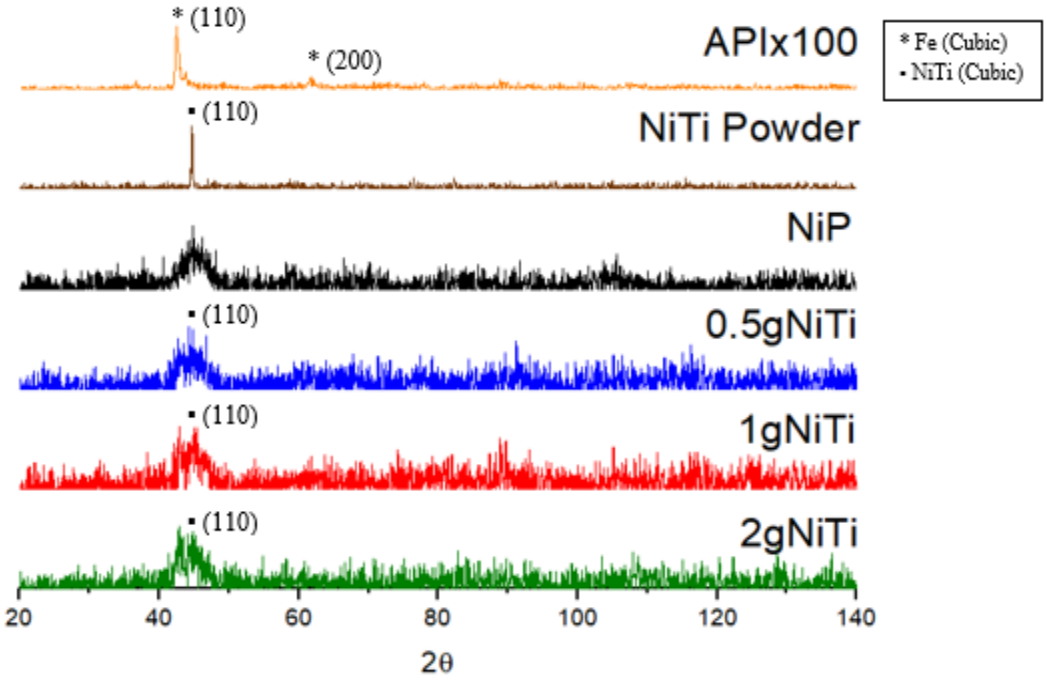

Figure 4-5 X-ray diffraction patterns with planes for substrate, superelastic NiTi nano-powder, Ni-P monolithic coating and composite coatings

EDS was used to determine the relative distribution of NiTi particles within the matrix as well as the percentage of Ti in the coatings containing 0.5, 1 and 2 g nano-NiTi in the plating bath. The amount of NiTi in the cross section was found to increase with the addition of NiTi to the plating bath, as seen in Table 4-4. The amount of phosphorous present was also determined. On average, the phosphorous content was found to be 9.9 $\pm$ 0.91 wt.%P, therefore classifying the coatings in the present work as "high phosphorous" coatings.

Table 4-4 Wt.% of Ti found in composite coating cross-sections using EDS

[NiTi] added to plating bath (g/L)	%Ti present in cross-section (wt.%)
0.5	2.21
1	2.61
2	3.02

The EDS map in Figure 4-6 (a) reveals uniform distribution of NiTi particles within the coating. Since the ratio of Ni:Ti was previously determined using ICP-OES, the amount of NiTi in the coating can be estimated. Equation 27 shows the equation used to estimate the wt.% NiTi using EDS and ICP-OES results.

$$wt.\%\ NiTi = \%Ti + \frac{53}{40}\%Ti \qquad \text{(Equation 27)}$$

Where %Ti is from EDS, and 53/40 represents the ratio of Ni:Ti as determined from ICP. It was found that the amount of Ti in the cross-section increased with increasing amounts of NiTi in the solution. However, that being said, as the amount of powder in the solution increases it is expected that it will eventually reach a limit and level off or decrease slightly, due to saturation caused by agglomeration and settling of particles, as seen in the literature [94, 95, 96]. The amount of NiTi present in the cross-section is represented graphically in Figure 4-6 (b) and was found to range between 5.14-7.02 wt.% NiTi. Therefore, the remainder of the results will refer to the coatings as 5.14 wt.% NiTi, 6.07 wt.% NiTi, and 7.02 wt.% NiTi for 0.5 g NiTi, 1 g NiTi and 2 g NiTi coating, respectively.

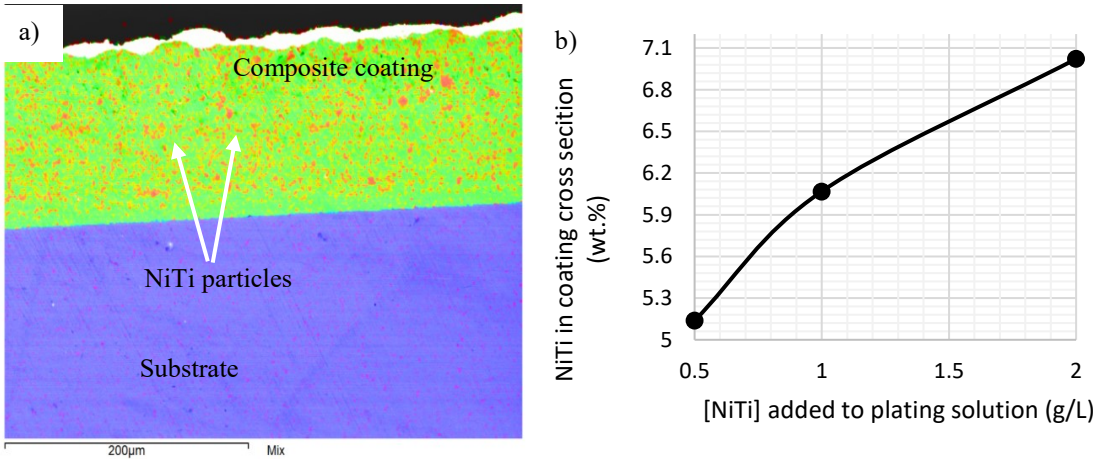

Figure 4-6 a) EDS mapping of 6.07 wt.% NiTi coating cross-section and b) amount of powder added into solution vs. amount of powder present in composite cross-section

4.2.2 Coating Integrity

Figure 4-9 provides images of the cross sections for Ni-P and Ni-P-nano-NiTi composite coatings. The coating/substrate interfaces reveal excellent bonding, and the coatings exhibit relatively uniform thicknesses as seen in the figure. Superelastic NiTi particles are clearly present. Some porosity is seen in the coating cross-section which is likely a result of the formation of hydrogen gas on the substrate during the plating procedure (Figure 4-8).

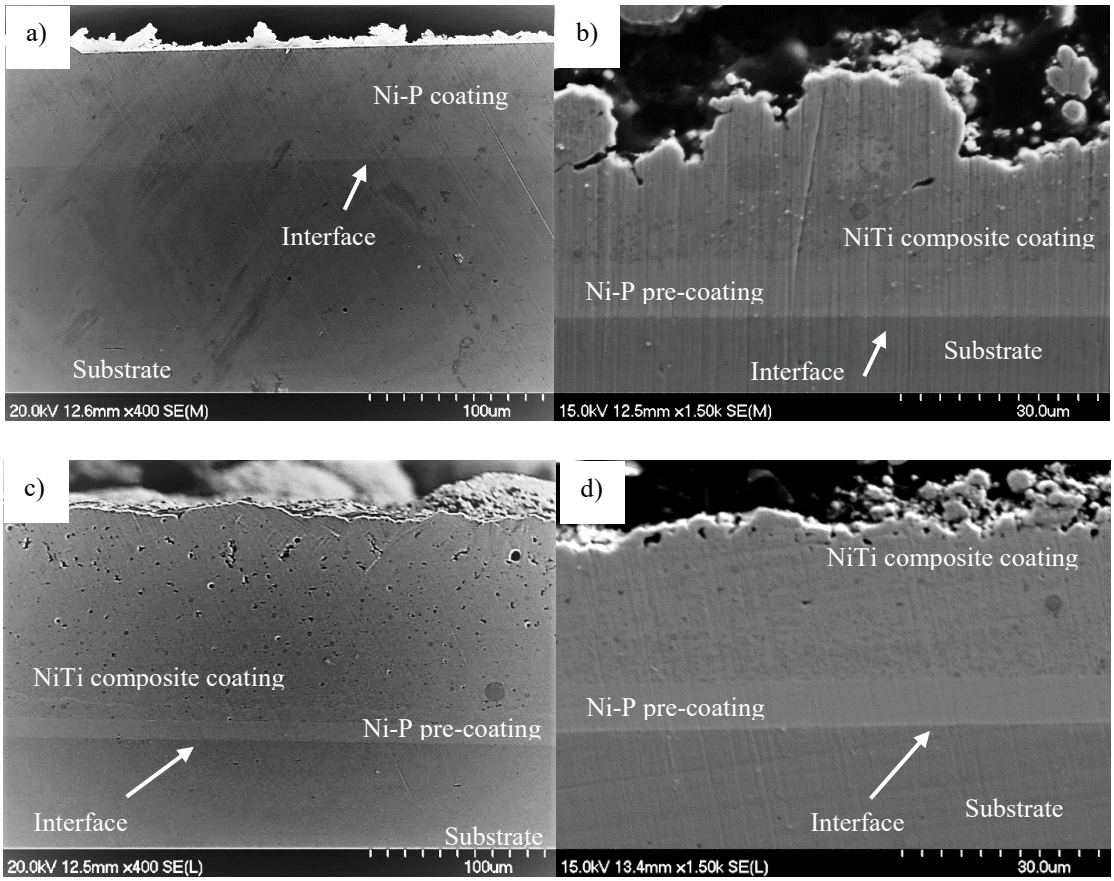

Figure 4-7 SEM images of a) monolithic Ni-P, b) 5.14 wt.% NiTi, c) 6.07 wt.% NiTi and d) 7.02 wt. % NiTi coating cross-sections

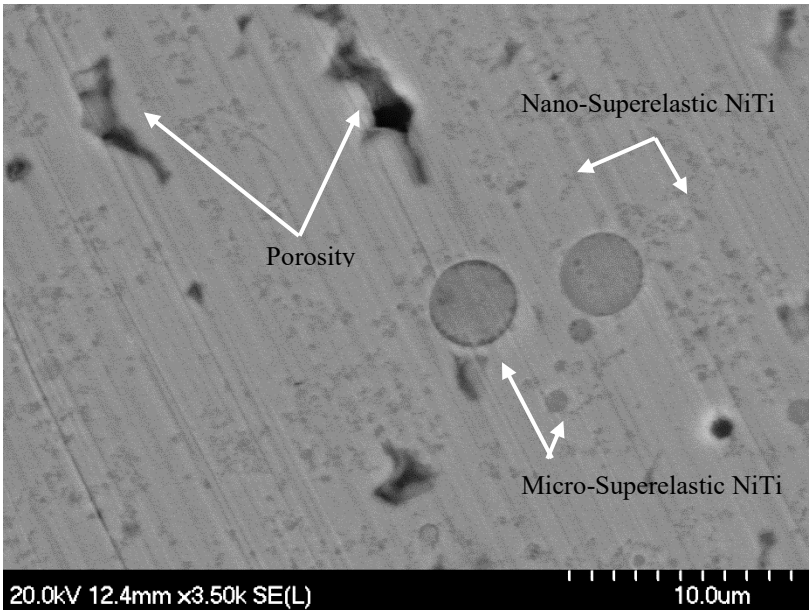

Figure 4-8 SEM of 6.07 wt.% NiTi coating showing porosity and large size distribution of particles in coating cross-section

The addition of nano-NiTi resulted in a rougher surface morphology in comparison to the Ni-P coating, as can be seen in Figure 4-9 which compares Ni-P coating to the composite coatings. These results agree with the results in the literature [97]. This increase in surface roughness was confirmed using surface profilometry. Surface profilometry scans of Ni-P and Ni-P-NiTi composite coatings are given in Figure 4-10. Surface roughness values of surfaces in Figure 4-10 were calculated using SPIP 6.0.6 image analysis software. Ra value for Ni-P coating was 1.54 μm, while the Ra value for the composites ranged from 3.3-8.1 μm. In both cases, a nodular structure was present, which is consistent with findings in the literature [98, 99, 100, 101].

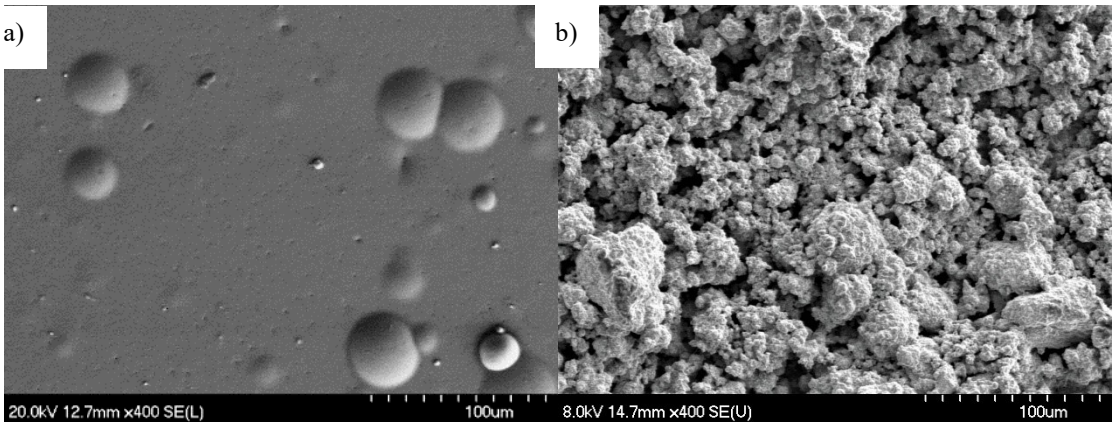

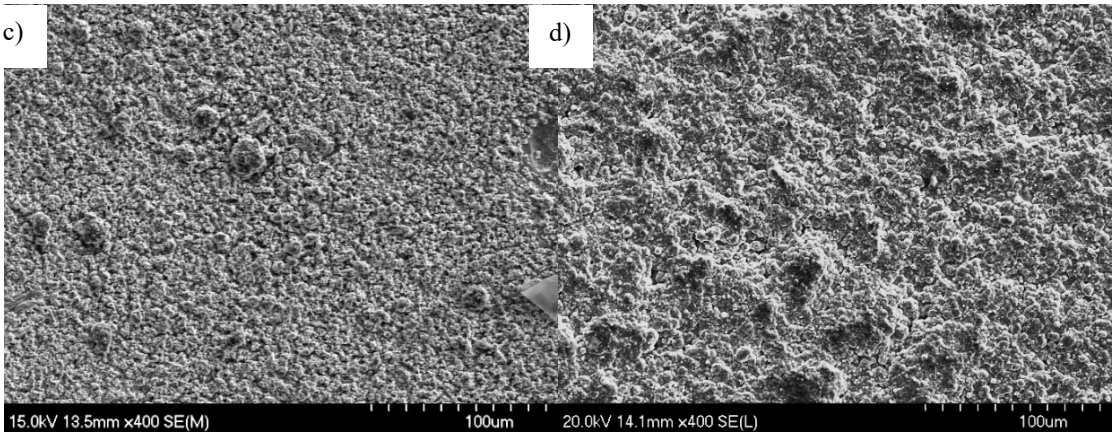

Figure 4-9 SEM images of a) monolithic Ni-P, b) 5.14 wt.% NiTi, c) 6.07 wt.% NiTi and d) 7.02 wt. % NiTi coating surfaces

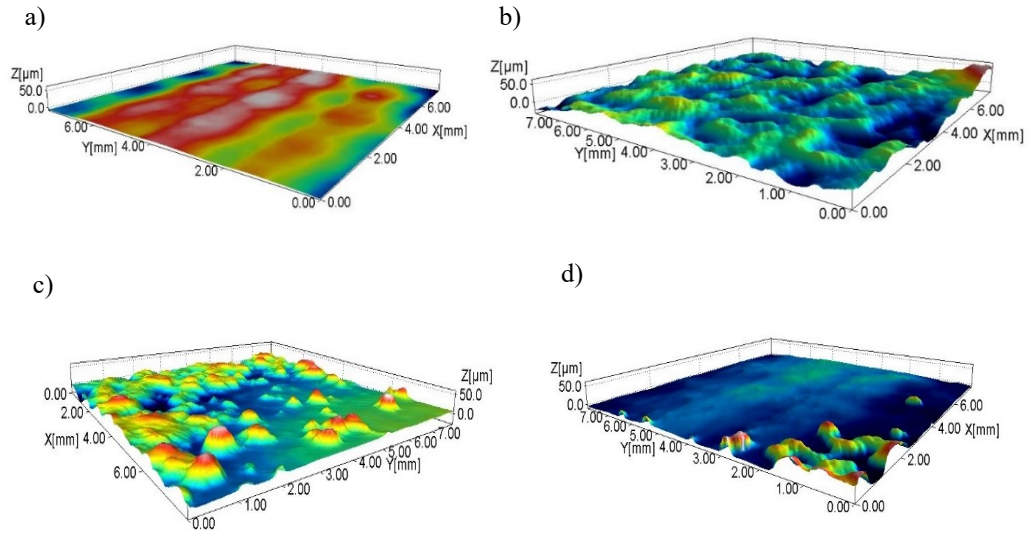

Figure 4-10 Surface topography of a) Ni-P b) 5.14 wt.% NiTi c) 6.07 wt.% NiTi and d) 7.02 wt.% NiTi coatings as deposited surfaces

4.2.3 Coating Properties

Hardness is a measure of the material's ability to resist deformation. The API X100 steel substrate has a Vickers hardness of 1.95 GPa. Ni-P coated steel has a Vickers hardness of 5.98 GPa, which is in the range of other reported values [102, 103, 104]. Vickers hardness

ranged from 4.25-4.82 GPa for the composite coatings, as seen in Figure 4-11. The addition of NiTi to the matrix resulted in minimal changes in hardness from the Ni-P coatings, however, the hardness in comparison to the substrate increased nearly three-fold. The observed slight drop in hardness of the Ni-P-NiTi composite as compared to the monolithic Ni-P coating can be explained as follows. As has been reported in the literature, the hardness of bulk superelastic NiTi ranges from 2.8-3.2 GPa [105, 106, 107]. Therefore, the addition of NiTi particles to the amorphous Ni-P is expected to decrease the hardness. However, to reiterate; the purpose of the addition of the superelastic NiTi is to enhance the toughness of the coating, even at the expense of a slight drop in hardness.

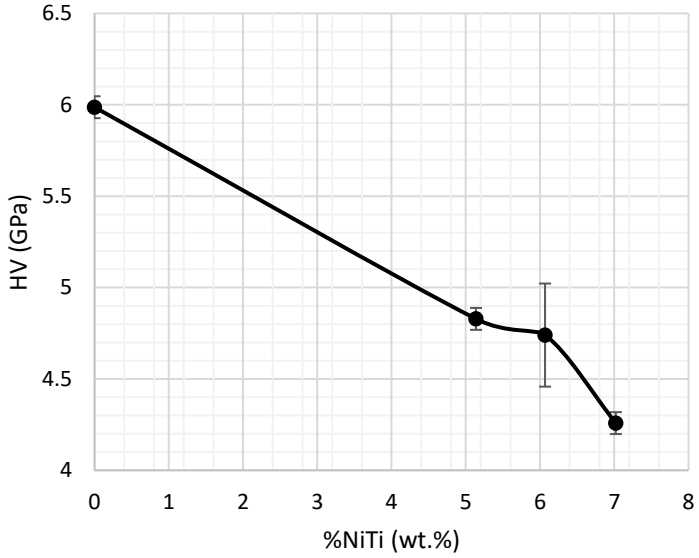

Figure 4-11 Vickers hardness as a function of wt.% NiTi in the composite coatings

The coefficient of friction (COF) was measured throughout the duration of each scratch test. As expected, the coefficient of friction increased with an increase in load due to the increase in force being applied resulting in an increase in contact area. The coefficient of friction was found to be the highest for the 5.14 wt.% and the 7.02 wt.% coatings, increasing from 0.11-0.27 and 0.13-0.27 respectively, with an increase in load from 0.5-4 kg. The 6.07 wt.% NiTi coating and Ni-P coating were found to have the lowest relative COFs, ranging from 0.13-0.22 and 0.12-0.2 respectively.

Figure 4-12 shows the effect of NiTi additions on the average COF for all constant load single pass conditions. COF for the composite coatings shows minimal change from that of Ni-P coatings, and any fluctuation can be attributed to the presence of superelastic NiTi particles on the surface affecting the indenters ability to slide smoothly across the material. COF for Ni-P is typically low due to its natural lubricity [94].

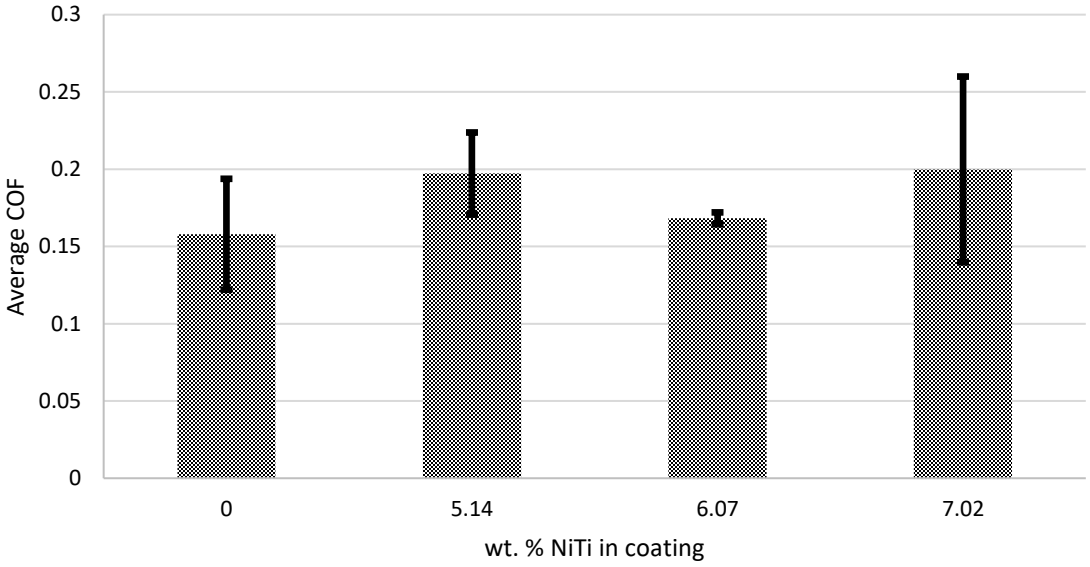

Figure 4-12 Average COF values for each coating under single pass conditions

It was found for the multi-pass conditions that as the number of repetitive passes increased, the COF increased for the 5.14 wt.% and the 7.02 wt.% NiTi coatings. However, the COFs for the 6.07 wt.% NiTi and monolithic Ni-P coating remained nearly the same for all number of passes. Figure 4-13 shows the average COF for each coating under 2 kg load for up to 40 passes. The COF followed a similar trend to that of the single pass conditions, with the 5.14 wt.% and 7.02 wt.% NiTi coatings having the highest (0.193 and 0.173 respectively), and the 6.07 wt.% NiTi and monolithic Ni-P having the lowest (0.139 and 0.11 respectively). Overall, for both conditions, COF for Ni-P coatings were slightly lower than that found from the literature (0.23) [108], however, the study used nano-scratch testing and thus the effects from the substrate were negligible, unlike the micro-scratch testing which was employed in this study.

Therefore, in general the composite coatings showed slightly higher COFs in comparison to the monolithic Ni-P coating. This is likely a result of the particles on the surface inducing roughness which increases friction between the surface and the indenter. However, the increase is very small and thus does not have a significant effect on the wear behaviour.

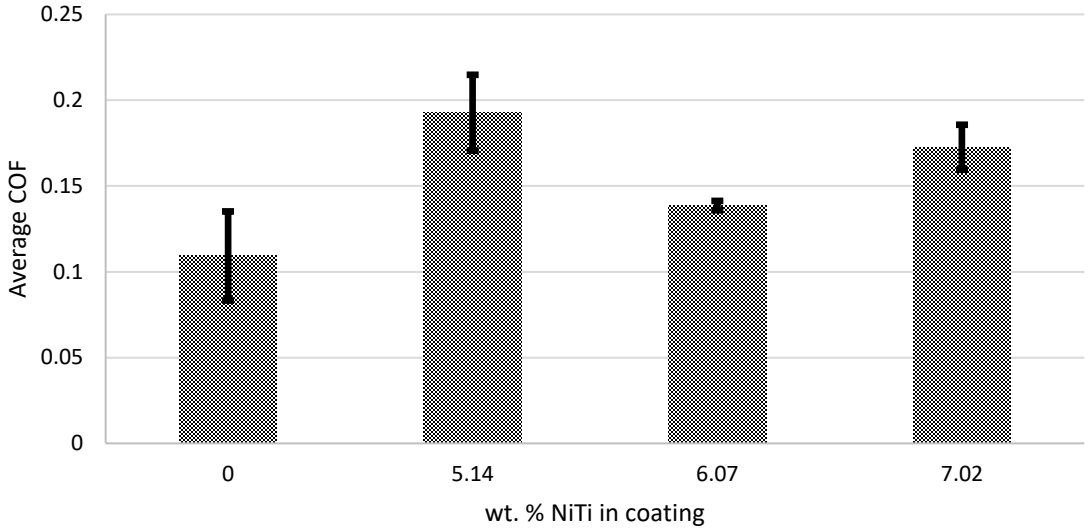

Figure 4-13 Average COF values for each coating under 2 kg multi-pass conditions

Force-displacement curves were generated during bending of each sample to aid in determination of elastic modulus and bend strength. As seen in Figure 4-14, the force-displacement curves of the monolithic Ni-P coating and the 5.14 wt.% NiTi coating are generally smooth. However, there are significant drops in force for the 6.07 wt.% NiTi and 7.02 wt.% NiTi coatings. These drops in force have been correlated to major cracking and delamination in the literature [91]. As the wt.% NiTi is increased, the force required to induce small displacements is also increased, meaning that the coatings containing higher amounts of NiTi require higher amounts of stress to deform. However, large drops in force are seen sooner with higher amounts of NiTi, which are associated with delamination. Thus, these higher forces induce enough strain to de-bond the coating at lower displacements in comparison to the monolithic coating.

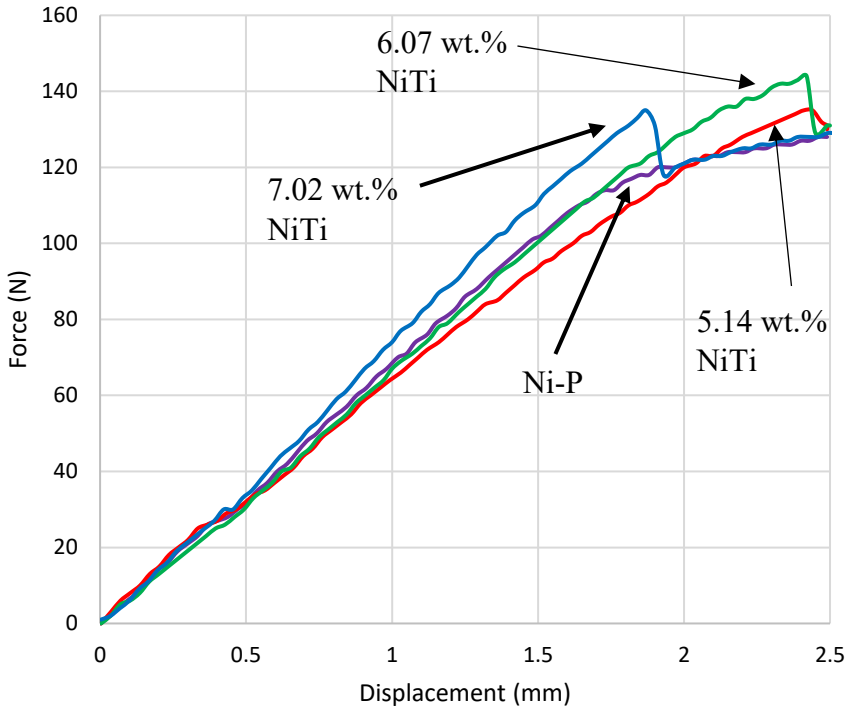

Figure 4-14 Force-displacement curves of monolithic Ni-P coating, 5.14 wt% NiTi coating, 6.07 wt.% NiTi coating and 7.02 wt.% NiTi coating

The elastic modulus was calculated based on the size of the sample and the slope of the force displacement curve. The elastic moduli for the coatings are shown in Table 4-5. The bulk modulus found for the Ni-P coating agreed with results found in the literature [2]. It was found that the composite coatings showed a decrease in elastic modulus in comparison to the monolithic Ni-P coating. As found in the literature, the elastic modulus of Ni-P and NiTi respectively are approximately 160 GPa [91], and ranges from approximately 30-75 GPa depending on the phase present [109]. Therefore, it is not unexpected that the elastic modulus would drop. This is indicative of increased toughness within the coatings. As the amount of NiTi is increased in the coating, the bulk modulus increases, meaning the coatings become stiffer due to enhanced particle incorporation.

Using the force at 2.5 mm displacement, the bend strength of the coatings was estimated. AE signals are useful in determining the displacement required to initiate the first crack, as this will correspond to a spike in energy being released. The bend strength of the coatings is also included in Table 4-5. It was found that the addition of superelastic NiTi resulted in

a decrease in bend strength in comparison to monolithic Ni-P. Similar trends were seen with the hardness data, showing that as NiTi is added to the matrix, the matrix becomes softer and more easily deformed.

Table 4-5 Experimentally calculated bulk modulus and bend strength values of monolithic Ni-P and Ni-P-nano-NiTi composite coatings.

Wt.% NiTi	E_b (GPa)	σ_b (MPa)
0	144	721
5.14	105	687
6.07	113	646
7.02	122	595

4.3 Scratch Response

4.3.1 Wear Behaviour

Scratches were analyzed microscopically using OM and SEM in order to gain a better understanding of cracking behaviour. Cracks are generally oriented perpendicular to the wear track, resembling Hertzian-type cracks, as seen in Figure 4-15. At low loads, minimal wear is seen in both the monolithic and composite coatings. As the applied load increases, more wear is seen, as expected. Monolithic Ni-P coatings showed few major Hertzian cracks (Figure 4-15 (a)). On the other hand, the composite coatings showed more frequent micro-cracks (Figure 4-15 (b), (c), (d)). This increase in cracking frequency is likely attributed to the surface roughness of the composite coatings. NiTi particles act as stress concentrations on the surface, making crack initiation easier. However, the crack energy is quickly dissipated due to the presence of superelastic NiTi particles, reducing major cracks

to micro-cracks. This behaviour was seen under constant, increasing load, and multi-pass conditions.

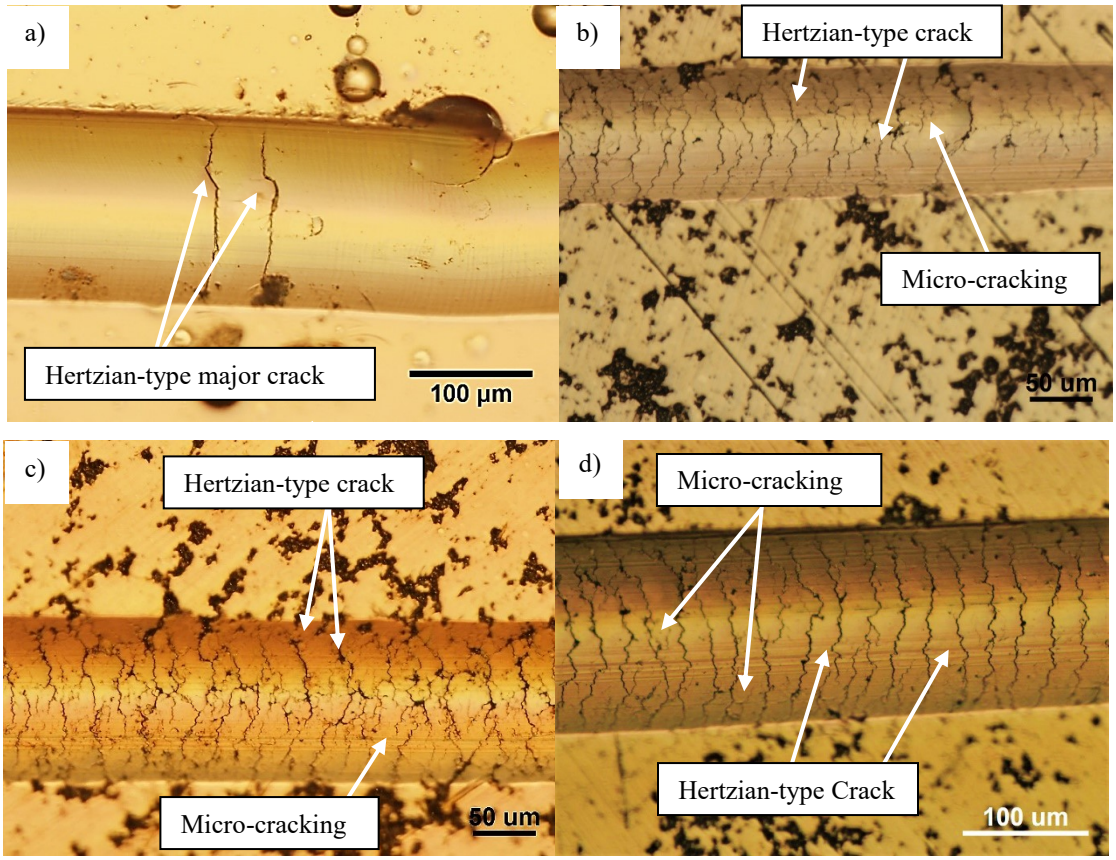

Figure 4-15 Wear track of a) Ni-P coating under increasing load showing major Hertzian-type cracks and b) 5.14 wt.% NiTi coating, c) 6.07 wt.% NiTi coating and d) 7.02 wt.% NiTi coating under increasing load showing evidence of Hertzian-type cracks and micro-cracking near the end of the wear track

As expected, the damage of the coatings increased with increasing number of consecutive passes. As seen with the increasing load samples, the monolithic coating showed evidence of major cracks, while the composite coatings showed micro-cracking as well as material pile-up. Evidence of this is shown in Figure 4-16 for the 6.07 wt.% NiTi coating. This is indicative of both ductile and brittle behaviour in the composite material, proving that toughening effects are taking place within the coatings. Wear tracks tended to be larger for the composite coatings under multiple pass conditions, likely as a result of the increased

ductility from superelastic additions, and the fact that the composite coatings had a lower hardness than the monolithic Ni-P coatings, illustrated in Figure 4-17.

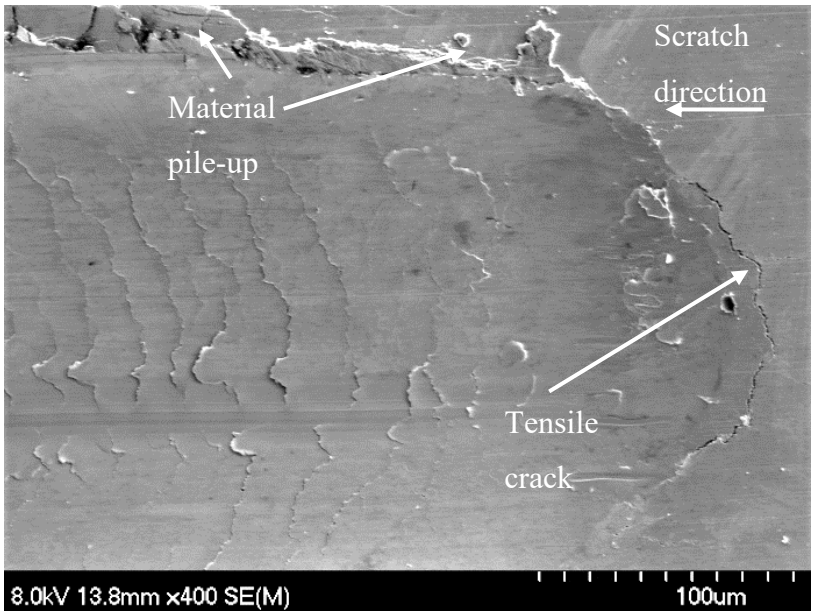

Figure 4-16 Wear track of 6.07 wt. % NiTi coated sample under 2 kg load, 40 passes showing material displacement and tensile cracks

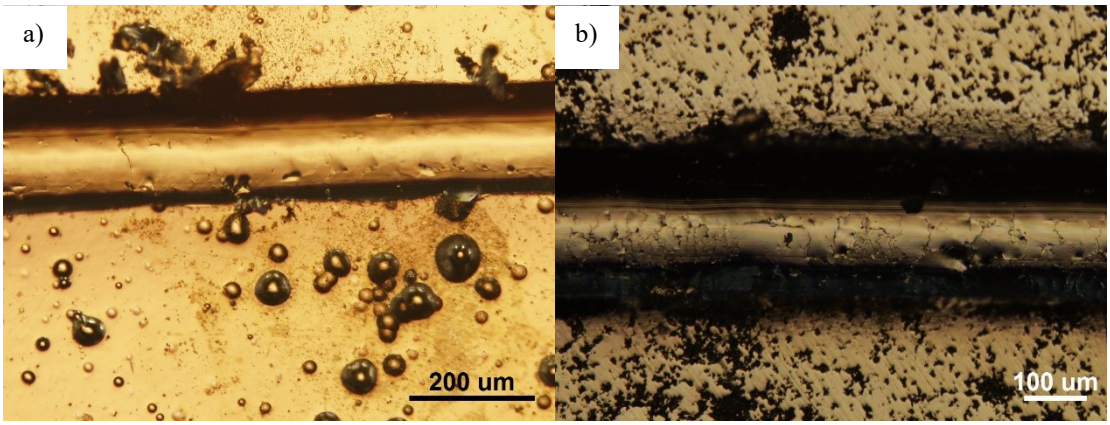

Figure 4-17 Wear track of a) monolithic Ni-P coating and b) 7.02 wt.% NiTi coating under 2 kg load, 40 passes

4.3.2 Volume Loss

3D profilometry was done to determine the width of each wear track. Volume loss was calculated using equation 21. Pile-up effect at scratch edges was eliminated when volume loss was calculated. In general, the volume loss increased for all coatings with increasing load under single pass conditions. The volume loss for a single pass at varying loads is displayed graphically in Figure 4-18. Each sample showed minimal change in between 0.5 kg and 1 kg. However, in general, the volume loss showed higher increases with subsequent increase in load, as expected. The 5.14 wt.% NiTi coating showed the highest volume loss at high loads, followed by the monolithic Ni-P coating, the 7.02 wt.% NiTi coating, and the 6.07 wt.% NiTi coating respectively.

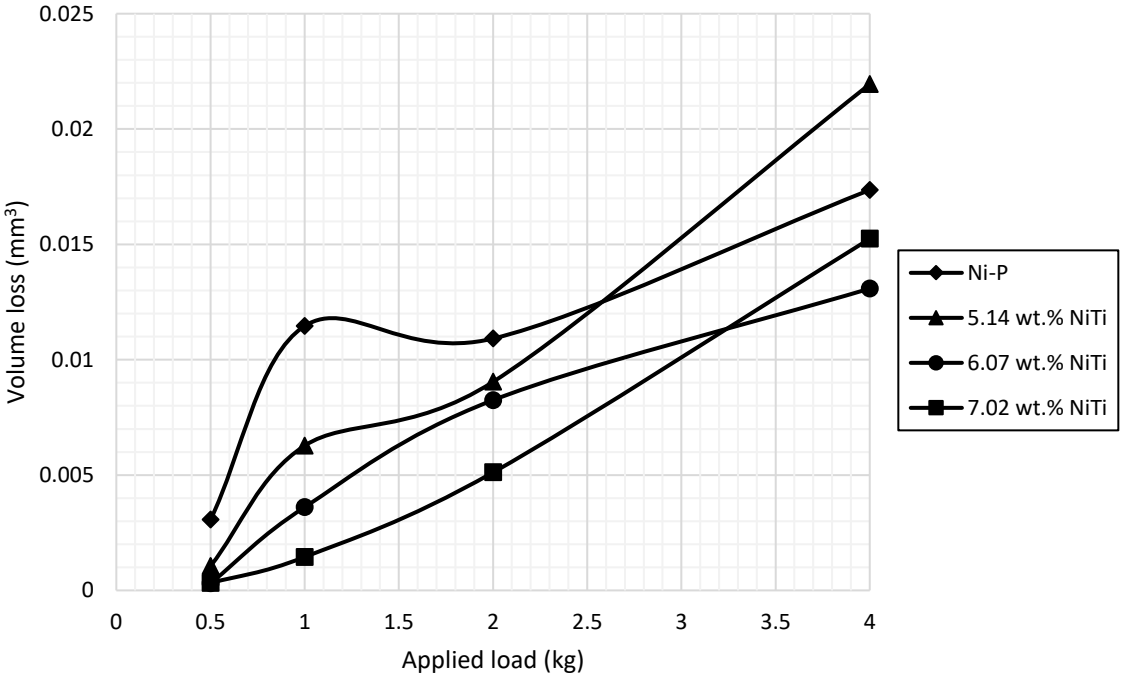

Figure 4-18 Volume loss as a function of load for single pass scratch test at varying constant loads

Volume loss was also determined for multi-pass conditions as a function of sliding distance, as shown in Figure 4-19. As seen with the constant load, volume loss increased

with increasing sliding distance. This data shows that under multiple passes, volume loss increases with increasing amounts of % NiTi.

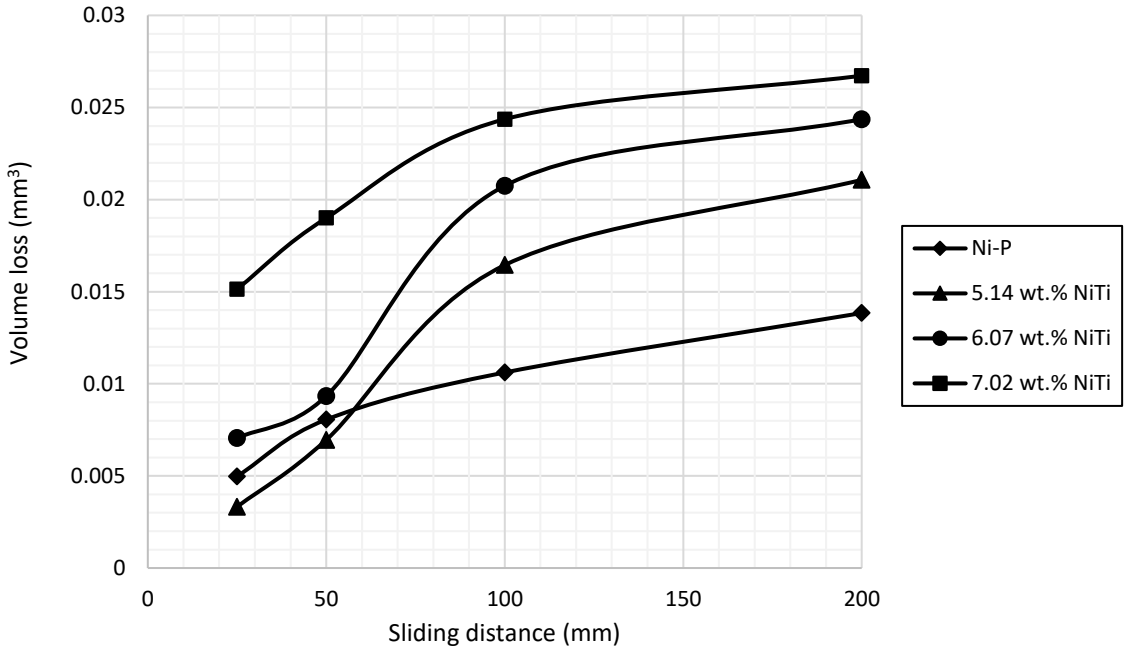

Figure 4-19 Volume loss as a function of sliding distance and %NiTi in the coating

Figure 4-20 shows the depth profiles for each sample under multi-pass conditions, generated from profilometry scans. At lower number of passes the depth profiles are quite similar. However, as the number of passes increases, the composite coating shows much deeper profiles suggesting that more material is being removed, more consistent with a ductile, softer material. Since the composite coatings were tougher than the monolithic Ni-P coatings, the dominant mechanism of wear is material removal. On the other hand, for the monolithic coatings, the dominant mechanism of wear is brittle fracture. Therefore, rather than material being removed, the sliding energy of the scratch test indenter is converted into crack initiation and propagation It is also important to note that the 7.02 wt.% NiTi shows the most evidence of pile-up of all of the coatings, even at lower number of passes, suggesting that it's ductility is higher—likely a result of the fact that the concentration of NiTi is the highest.

Therefore, is likely that at lower loads or a single pass, the testing energy is still in the elastic region, and thus both the monolithic coating and the composite coating are able to

elastically recover during testing. Due to the enhanced toughness, the composite coatings are able to recover more than the monolithic Ni-P. However, under multiple passes the force being exerted on the surface is likely above the yield strength of coating. As the monolithic coating has higher hardness, it is able to resist deformation better than the composite coatings, which can account for the lower wear track depth seen above. However, as seen above the monolithic Ni-P coatings are subject to severe brittle fracture, which does not contribute to metal loss. So, volume loss may not be the best method when comparing damage of brittle materials to more ductile ones.

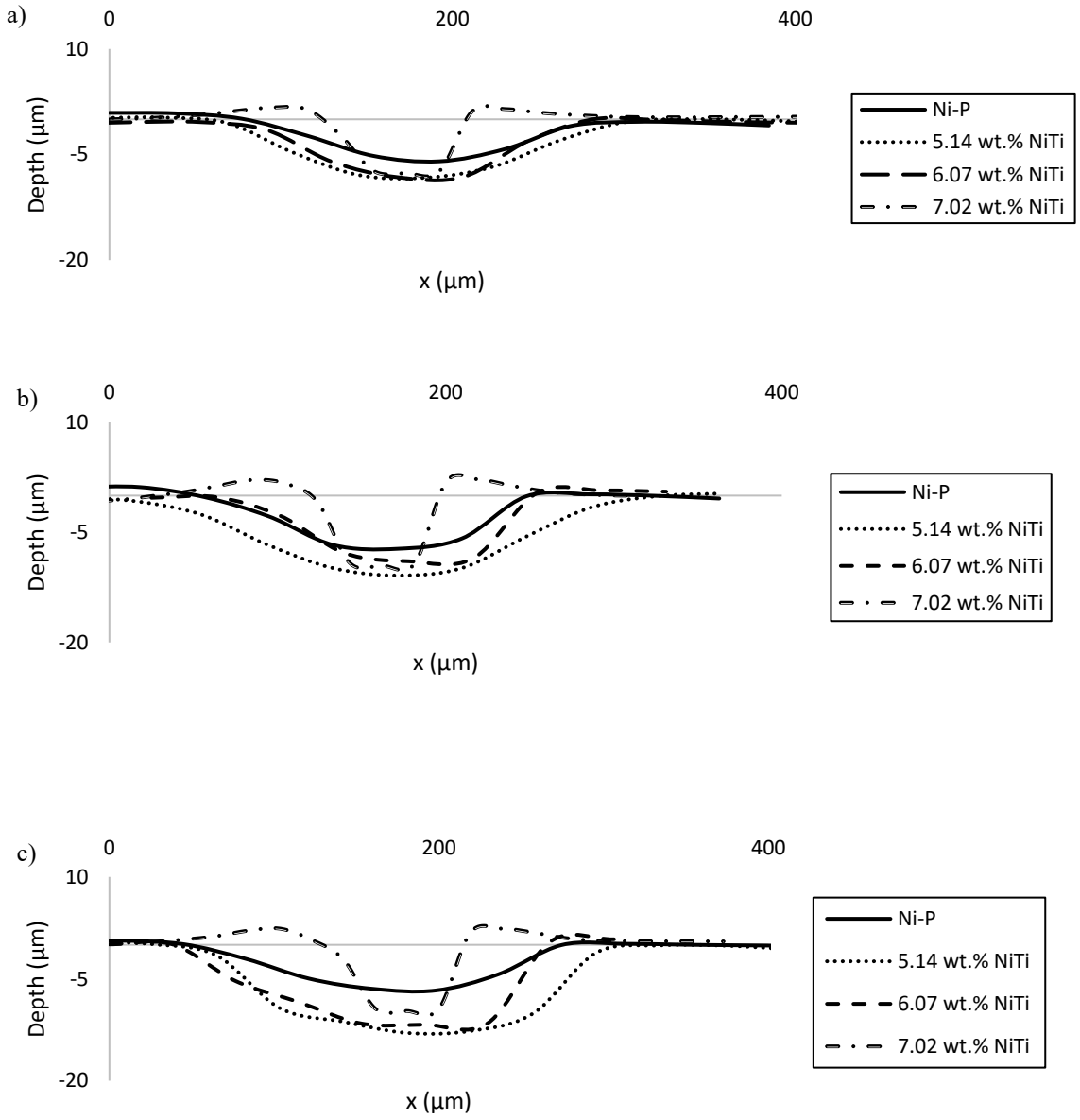

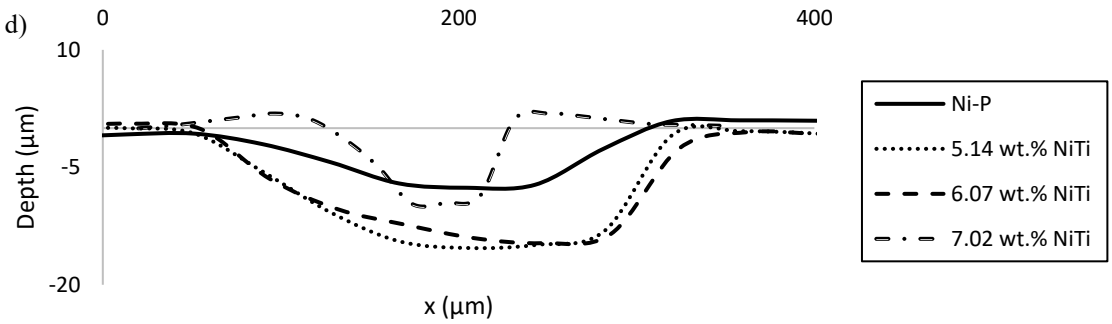

Figure 4-20 Scratch track depth profiles for multi-pass scratches under a) 5 passes, b) 10 passes, c) 20 passes and d) 40 passes

4.3.3 Acoustic Emission

Acoustic signals (AE) were measured during each test in order to monitor the presence of any microscopic activity during scratching. As expected, with higher constant loads, AE signals were higher for all coatings, due to the fact that higher stresses are being applied, resulting in more energy for crack initiation and propagation. Figure 4-21 shows the acoustic emission signals for each sample under 1 kg constant load. The Ni-P coating showed the highest peaks at around 7 V. The next highest was the 7.02 wt.% NiTi, however the recorded voltage was much lower at around 3 V, followed by the 6.07 wt.% and 5.14 wt.% respectively which both remained under 1 V. This trend was seen under each loading condition.

AE data in Figure 4-21 reveals two main types of signals. The first being low noise signal, which is likely associated with micro-cracking of the coating within the scratch tracks as previously seen in Figure 4-15. The low noise could also be attributed, in part, to surface topography. Coatings containing NiTi particles are likely to produce these low signals as the indenter goes over a particle. The second type of signal is characterized by a high noise level spike. This high-level signal is attributed to the formation of major cracks. In the present data, it is clear that the composite coatings did not show high AE signal. However, the 7.02 wt.% NiTi composite seems to show higher and more frequent signals than the

other two composite coatings. This can be correlated to the higher number of NiTi particles in the coating. It can be stated that the reason for low noise levels associated with the composite coating, as compared to monolithic Ni-P coating, is mainly due to micro-cracking of the coating. This is consistent with micro-cracking toughening mechanism operating in these composite coatings seen in OM images. On the other hand, the monolithic Ni-P coating shows high and sharp AE signals, which indicated major cracking of the coating as observed by OM. AE data for each coating under 0.5 kg, 2 kg, and 4 kg can be found in Appendix B.

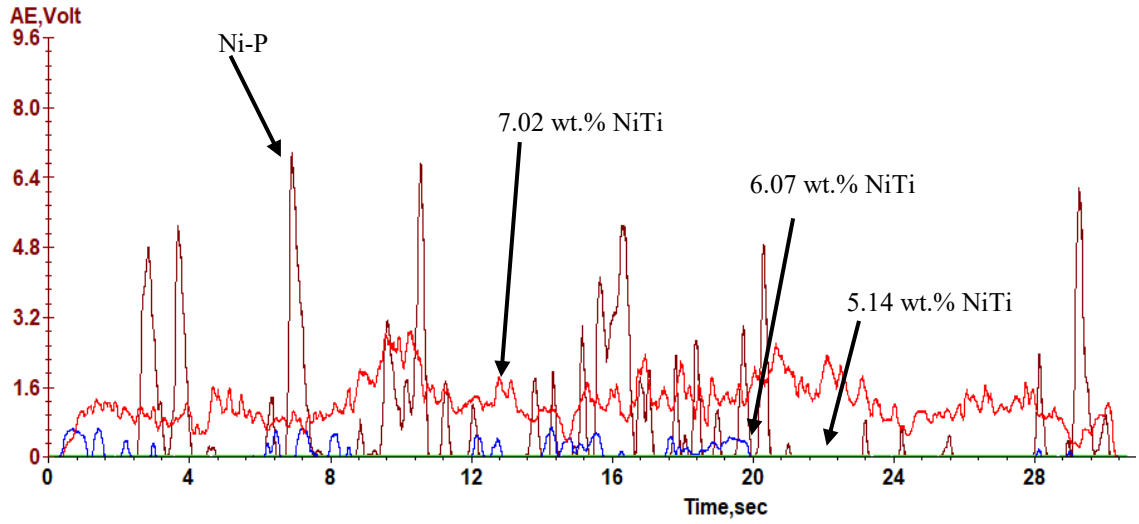

Figure 4-21 Acoustic emission signals under 1 kg constant load for Ni-P, 5.14 wt.% NiTi, 6.07 wt.% NiTi, and 7.02 wt.% NiTi coatings.

Similar AE signals were seen under increasing load conditions. As with the constant load conditions, the AE signals were the highest for the monolithic Ni-P coating, representative of major cracking in the coating. On the other hand, the composite coating showed much lower noise signals, as illustrated in Figure 4-22. Signals for the 5.14 wt.% NiTi and 6.07 wt.% NiTi coating are so low relative to the Ni-P coating that they are not visible on the same scale. As seen previously with constant load conditions, it is seen that composite coatings containing higher amounts of NiTi have higher, more frequent noise signals than coatings containing lower amounts. Again, this is likely due to the fact that there is a higher concentration of particles on the surface, affecting the indenters ability to slide smoothly

over the coating surface. It is also interesting to note that the Ni-P coating experiences high AE signals much sooner than the composite coatings, meaning that the Ni-P coating cracks more easily (i.e. under lower loads) in comparison to the composite coatings.

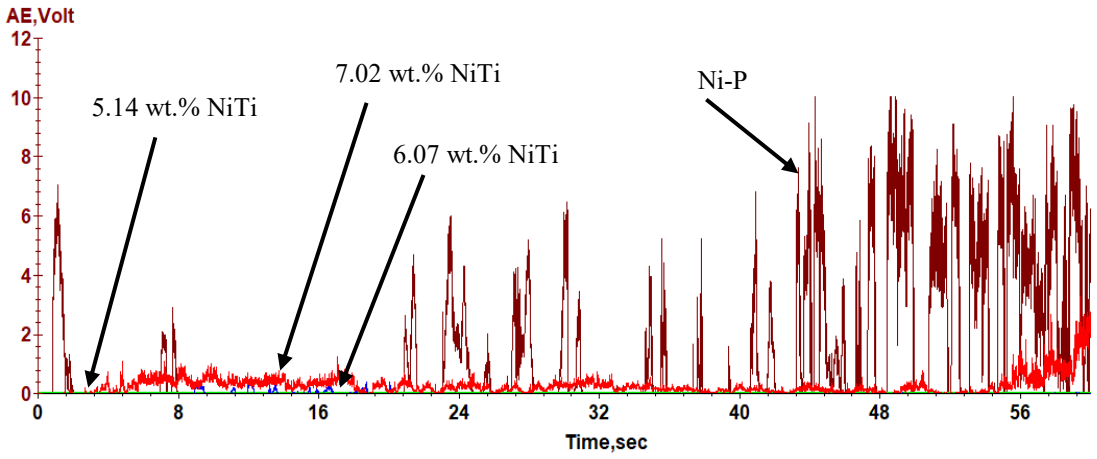

Figure 4-22 Acoustic emission signals for monolithic Ni-P, 5.14 wt.% NiTi, 6.07 wt.% NiTi and 7.02 wt.% NiTi coatings under increasing load conditions

In general, under scratch conditions, monolithic Ni-P is subject to major cracks within the matrix, extending past the edge of the wear track (Figure 4-23 (a)). These cracks are generated by tensile stresses that are generated behind the indenter, concave to the scratch direction. On the other hand, as shown in Figure 4-23 (b) for the Ni-P-nano-NiTi composite coating, several smaller Hertzian-type micro-cracks are seen, all contained within the wear track. Material pile-up is seen at the opposite edge of the wear track, indicating some ductility.

a)

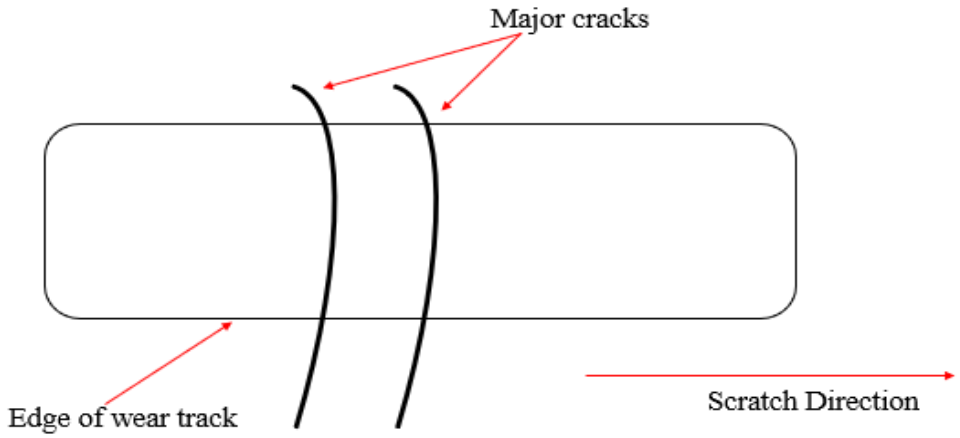

b)

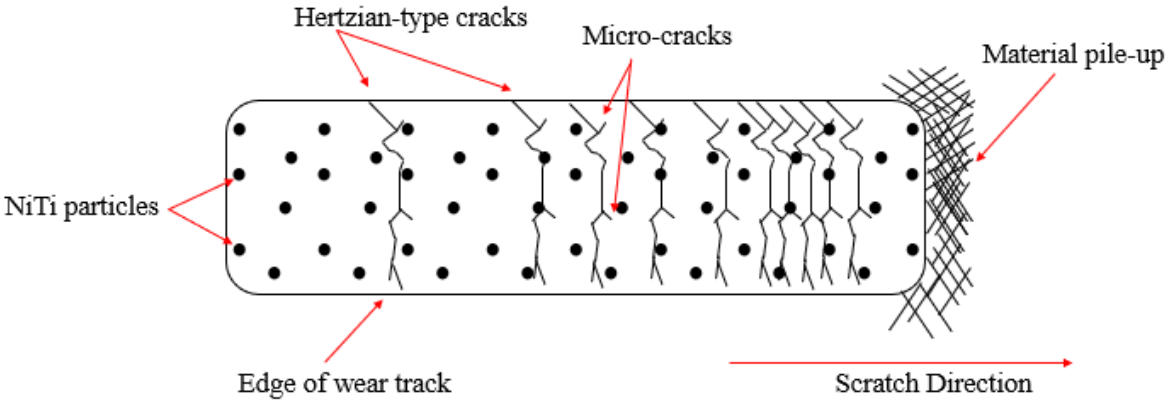

Figure 4-23 Schematic of scratch behaviour in a) monolithic Ni-P coating and b) Ni-P-nano-NiTi composite coatings showing proposed wear mechanisms

4.4 Indentation Behaviour

4.4.1 Load-Depth Curves and Acoustic Emission Signals

Load-depth (P-h) curves were generated for each coated sample at low and high loads in order to examine the indentation behaviour. Acoustic emission was recorded in order to

gain a better understanding of cracking behaviour and events of the composite coatings in comparison to the monolithic Ni-P coating. As evident in P-h curves in Figure 4-24 (a) and (c), the monolithic coating showed high acoustic emission noise beginning near 150 µm penetration depth and continuing for the duration of loading and unloading. This high activity likely correlates to the delamination and cracking seen in the optical images (Figure 4-24 (b), (d)). On unloading, minimal activity was seen under low loads, however, more activity was seen under higher loads. Cracking during loading is attributed to the energy release associated with the formation of radial and cone cracks [110].

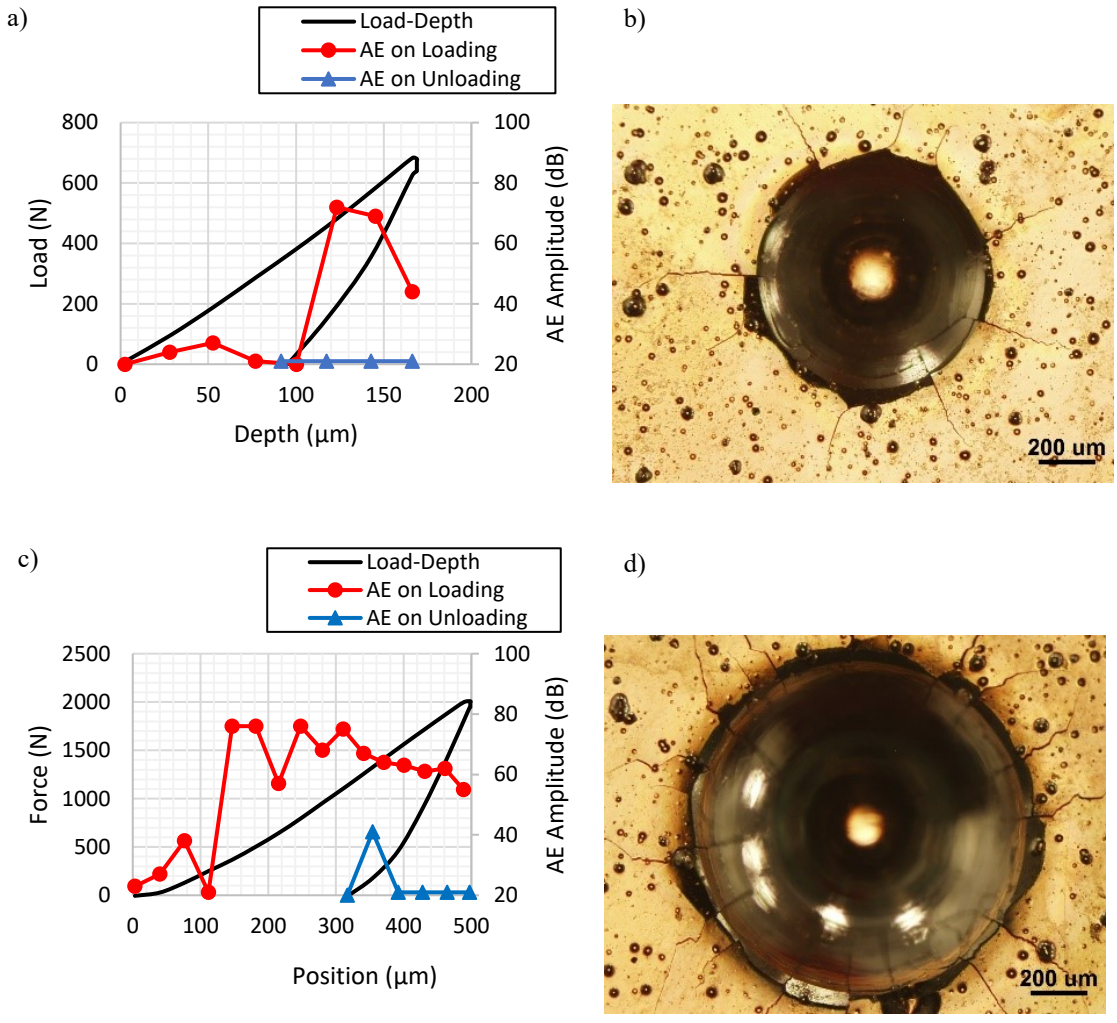

Figure 4-24 Load-depth curves for monolithic Ni-P coating under a) 600 N and c) 2000 N, and OM images of indent sites under b) 600 N and c) 2000 N

On the other hand, for the composite coatings (Figure 4-25-Figure 4-27), penetration depths and acoustic emission activity was found to be much lower than those of the monolithic Ni-P coating, particularly under low loads. Under 600 N load, there is no distinct increases in acoustic emission. From the OM image of this indentation it is clear that there are no major cracks, and, unlike the monolithic coatings, pile-up is present indicating some ductility. Slight increases in AE can be attributed to the formation of small radial cracks or delamination of the coating at higher loads.

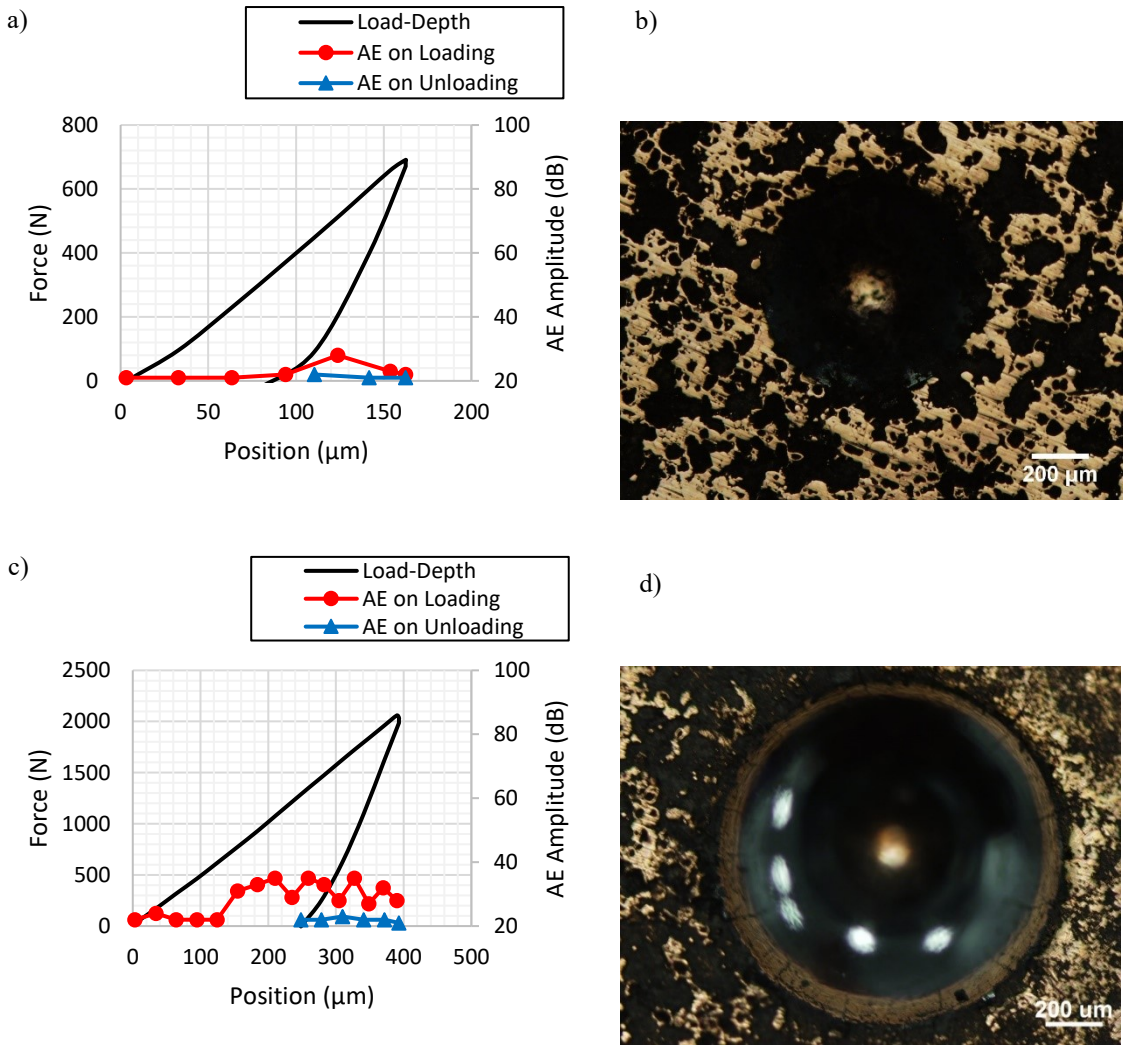

Figure 4-25 Load-depth curves for 5.14 wt.% NiTi coating under a) 600 N and c) 2000 N and OM images of indent sites under b) 600 N and d) 2000 N

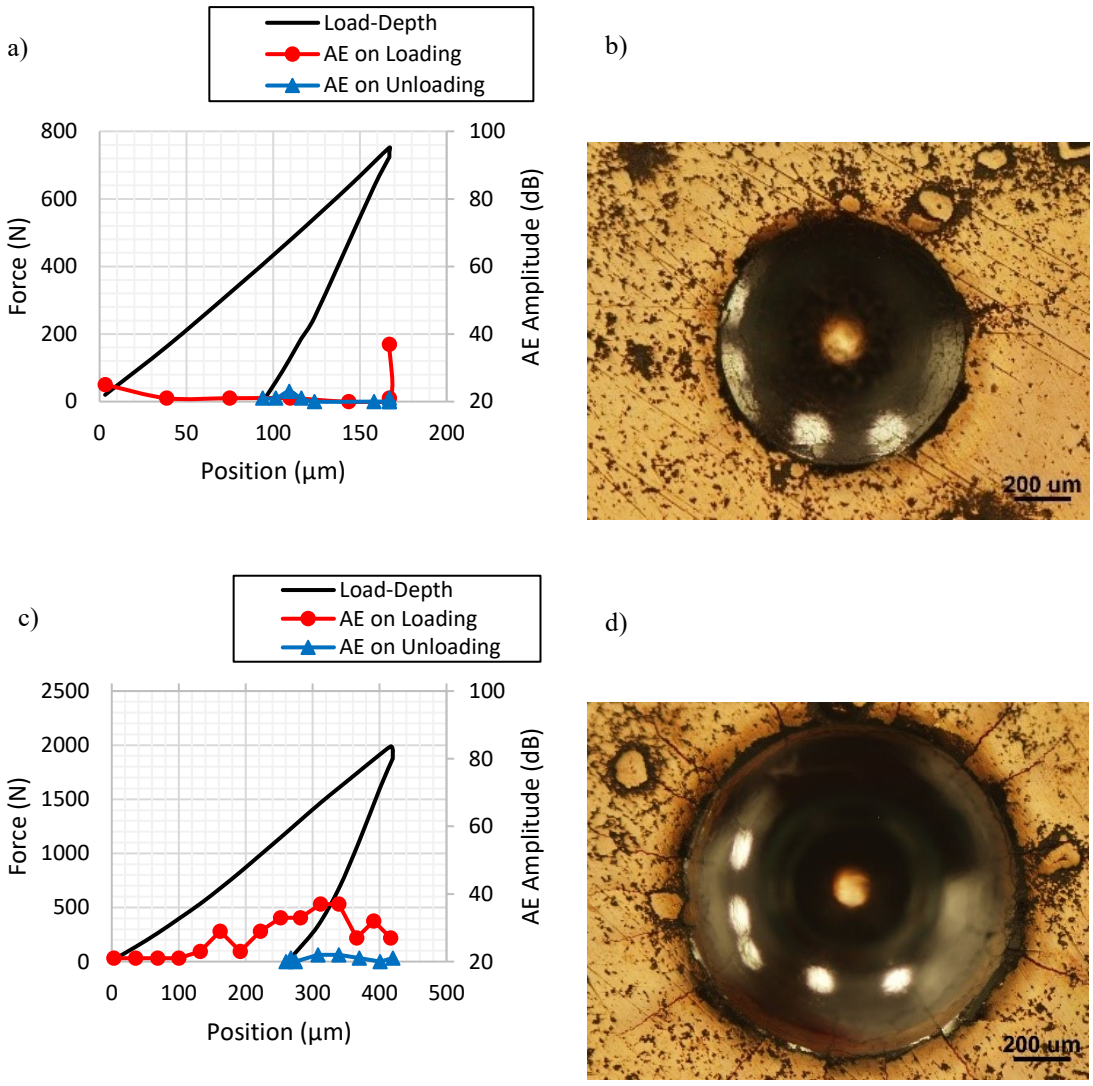

Figure 4-26 Load-depth curves for 6.07 wt.% NiTi coating under a) 600 N and c) 2000 N and OM images of indent sites under b) 600 N and d) 2000 N

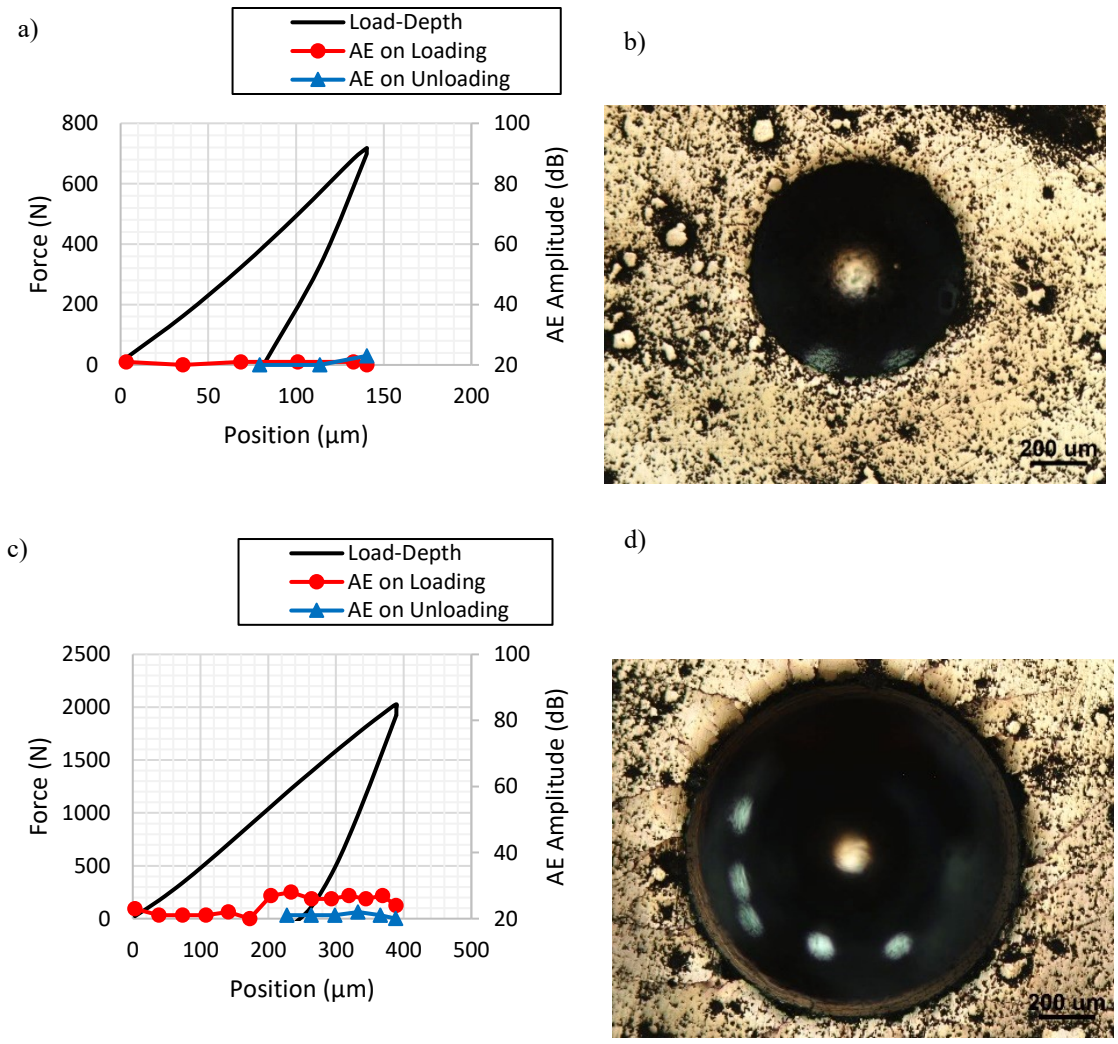

Figure 4-27 Load-depth curves for 7.02 wt.% NiTi coating under a) 600 N and c) 2000 N and OM images of indent sites under b) 600 N and d) 2000 N

At lower loads, the penetration depth of the composite coatings is lower than that of the monolithic Ni-P coating. However, as the maximum load applied increases, the penetration depths of the composite coatings approach (and even surpass) that of the monolithic coating. This can be seen in Figure 4-28- Figure 4-32. It is likely that at lower loads, both the monolithic coating and the composite coatings remain in the elastic region and the addition of superelastic NiTi particles aids the coating in absorbing the force applied by the indenter, thus limiting the depth that the indenter is able to penetrate. However, due to the fact that the Ni-P coating has the highest hardness, it is able to withstand higher

deformation loads than the composite coatings, which can attribute to relatively lower penetration depths at higher loads.

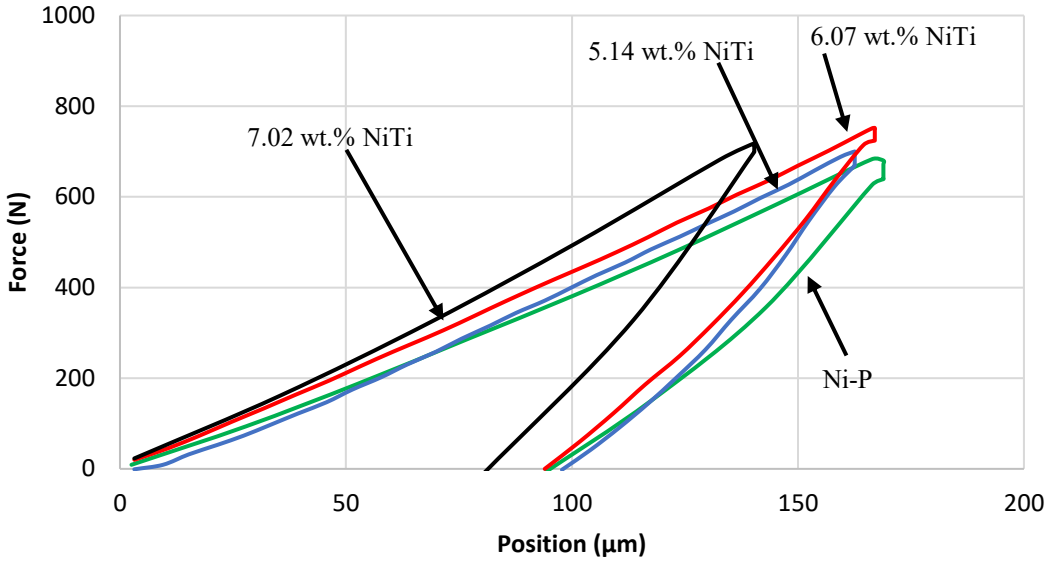

Figure 4-28 Load-depth curves for all coatings under maximum 600 N load

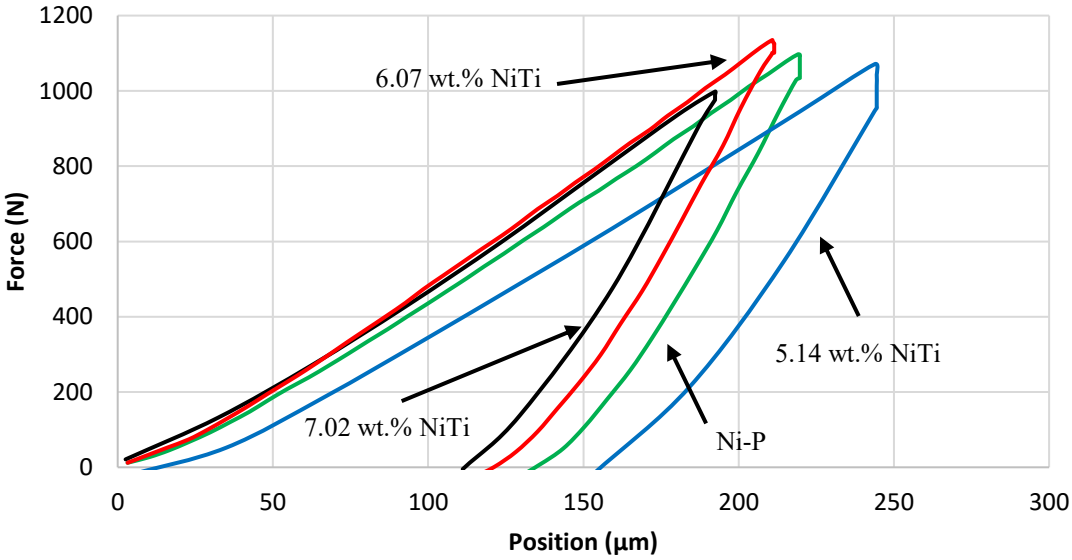

Figure 4-29 Load-depth curves for all coatings under maximum 1000 N load

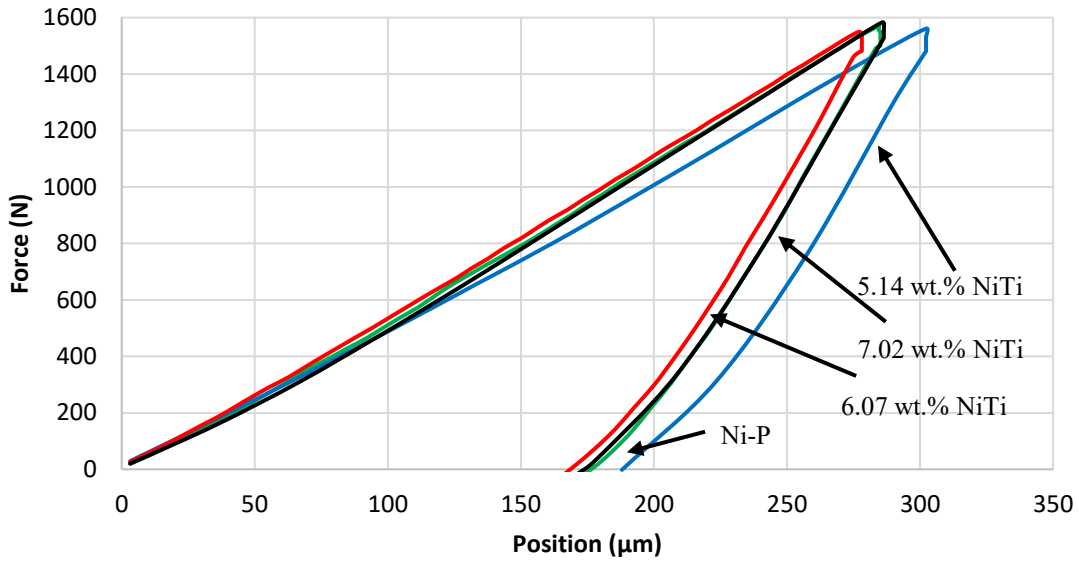

Figure 4-30 Load-depth curves for all coatings under maximum 1500 N load

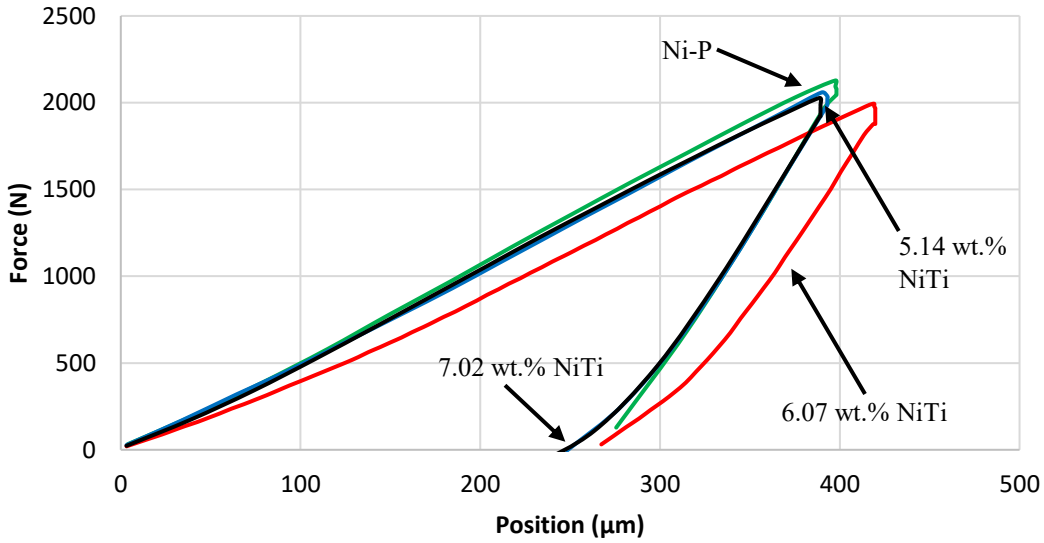

Figure 4-31 Load-depth curves for all coatings under maximum 2000 N load

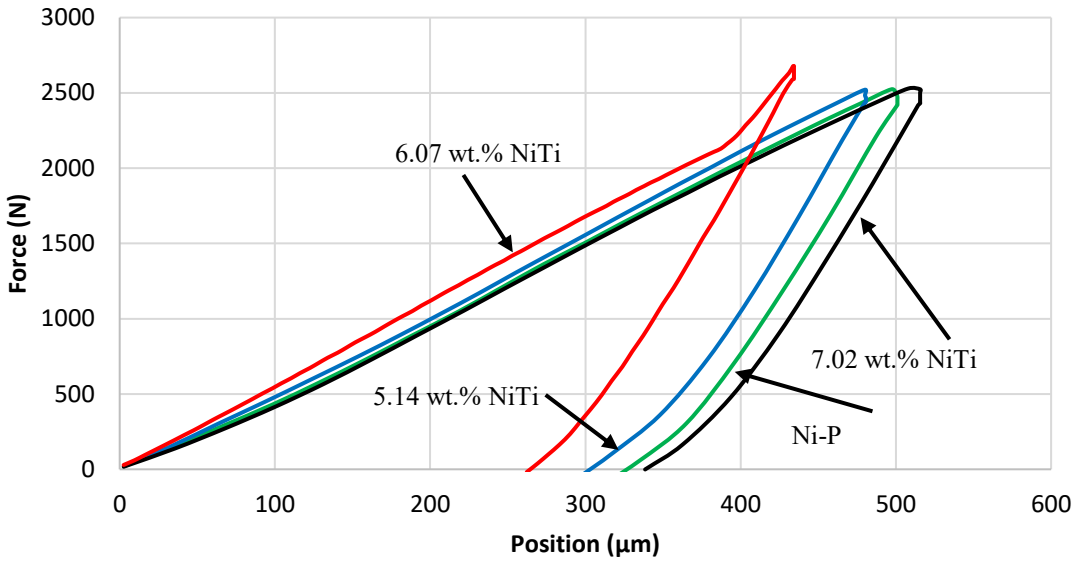

Figure 4-32 Load-depth curves for all coatings under maximum 2500 N load

4.4.2 Crack Initiation

All samples showed an increase in acoustic activity with an increase in load. As seen above, higher AE events (and thus cracking events) initiated sooner in the monolithic Ni-P coating than in the composite coatings, indicating that the monolithic coatings required lower loads to crack. The change in amplitude was examined in order to determine the applied load that corresponded to the initiation of cracking. Figure 4-33 depicts the relationship between the NiTi content in the coating and the load at which the first major crack occurred under a maximum load of 2000 N. Acoustic emission signals of the first crack are also displayed. It is clear that the amplitude (severity) of cracking drops with the addition of % NiTi and the force required to initiate cracking increases making crack initiation more difficult. This general trend was seen for all coatings across all testing loads.

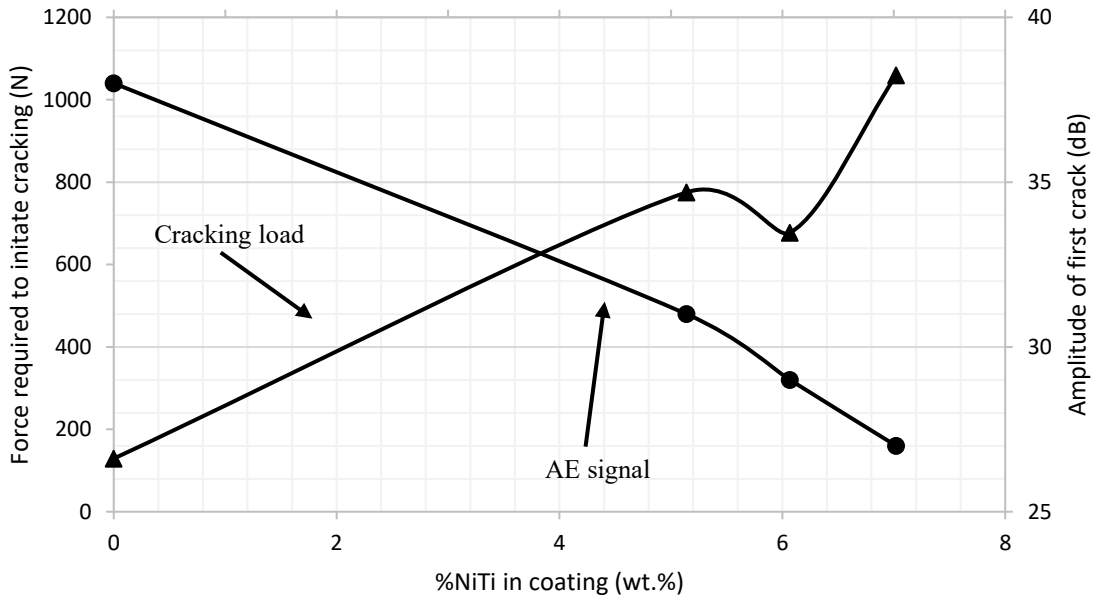

Figure 4-33 Load and acoustic emission signal of first major crack as a function of NiTi content in the coating concentration under a maximum load of 2000 N

All composite coatings were able to withstand much higher loads before major cracking occurred in comparison to the Ni-P coatings. It should also be noted that the amplitude specifically at the onset of major cracking is significantly reduced with the addition of the superelastic particles, which can be correlated to a reduction in the size of the cracks, leading to evidence of toughening. As well, the high amplitude seen with the Ni-P samples is likely also attributed to delamination, as the energy required to debond the coating is higher than that to produce cracks and therefore the cracking event would exhibit higher dB of energy. The general trend in Figure 4-33 clearly reveals the effect of the addition of NiTi particles to Ni-P coating, i.e., the initial cracking force drops, and AE signal rises with the increase in the number of incorporated particles. Furthermore, it is found that the coatings containing 5.14 wt.% and 7.02 wt.% NiTi required slightly higher forces to initiate cracking in comparison to the coating with 6.07 wt.% NiTi. It is believed that in general, toughness increases with increasing wt.% NiTi. However, the relatively small drop of ≈10% in the force required to initiate cracking in the 6.07 wt.% NiTi coating may be due to experimental scatter as a result of localized stress concentration on the roughened

surface, that is associated with the composite coatings. Surface defects may affect the cracking sensitivity of the coatings.

4.4.3 Cracking Behaviour

Figure 4-34 shows the cracking behaviour of the monolithic Ni-P and Ni-P-nano-NiTi composite coating. Radial cracks appear to be the most dominant cracking mode in each coating. Ring cracks and delamination were also present, with ring cracks predominantly found inside the indentation site, and delamination found on the indentation edge. It was found that the Ni-P coating exhibited large radial cracks and delamination at low static loads. As increasing amounts of nanosized NiTi powder were added, more plastic deformation was seen due to localized shear bands in the amorphous Ni-P matrix at the edge of the indentation [111]. This was also accompanied by less cracking and coating delamination. This reiterates the findings from the AE signals, where lower noise signals indicate less severe cracking and higher noise signals indicate more severe cracking and delamination.

As shown in Figure 4-34 (a), (c) below, the monolithic coating cracked completely through the coating all the way to the substrate. This, coupled with delamination results in failure and removal of the coating. However, the addition of superelastic NiTi can limit the number cracks propagating directly down to the substrate. Rather, they only propagate through the composite layer, and in most cases do not reach the pre-coating layer. For the coating containing 5.14 wt.% NiTi as shown in (Figure 4-34 (b), (d)) there is still instances of major cracks propagating through the entirety of the coating, with some being arrested in the composite layer. On the other hand, for the 6.07 wt.% coating, the cracks do not propagate further than the composite layer. In the case of the 7.02 wt.% NiTi coating, behaviour was similar. This increased effect of reduction in crack propagation is likely directly related to an increase in % NiTi in the coating. For lower amounts of superelastic particles (i.e. 5.14 wt.% NiTi) there are toughening effects, however the brittle nature of the Ni-P matrix still dominates. As more superelastic particles are incorporated into the matrix, the toughening effects become greater, eventually limiting any cracks to directly

beneath the indenter where stresses are highest. Indentation cross sections of the 6.07 wt.% NiTi and 7.02 wt.% NiTi coatings can be found in Appendix B.

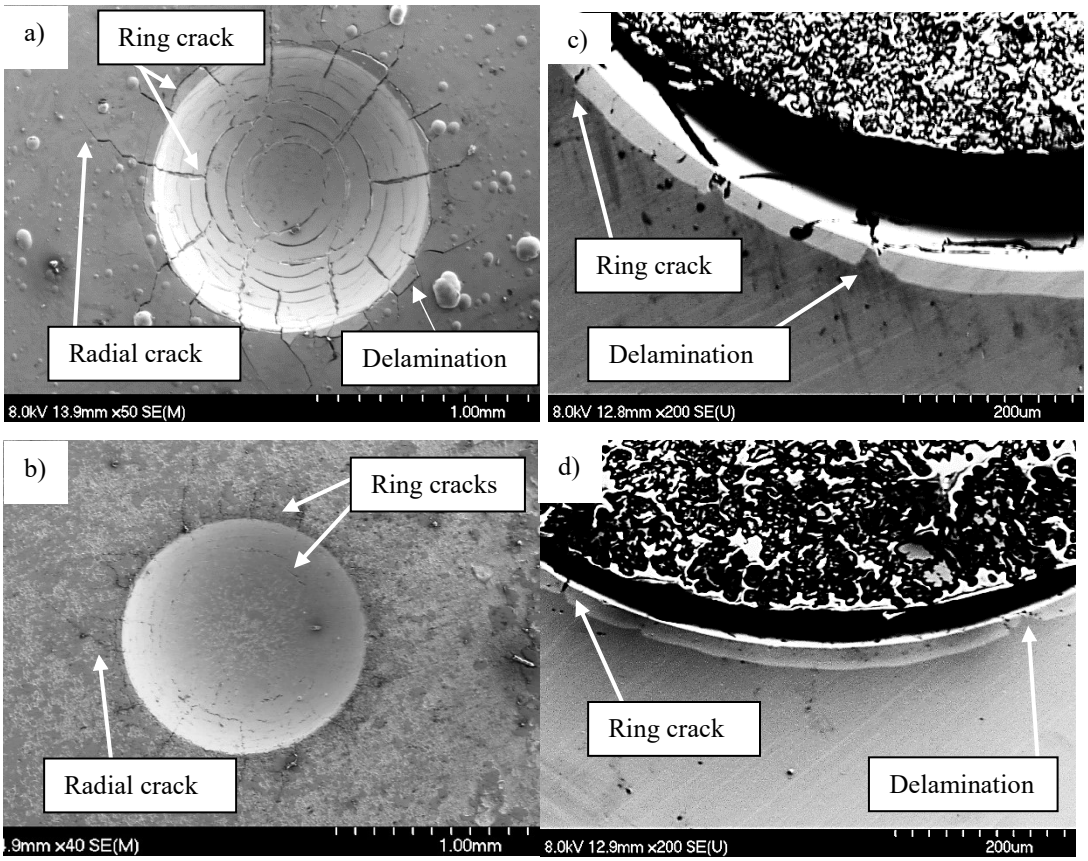

Figure 4-34 SEM of indentation surface and cross section under maximum load of 2500 N of a) Ni-P coating surface, b) 5.14 wt.% NiTi coating surface, c) Ni-P coating cross section and d) 5.14 wt.% NiTi coating cross section showing cracking patterns

4.5 Erosion Behaviour

4.5.1 Volume Loss

Volume loss was determined for each sample under all single particle impact conditions. Figure 4-35 (a) shows the effect of impact angle on volume loss at operating velocity of 35 m/s for all coatings. Minimal change in volume loss was seen with a change in angle,

suggesting that at lower velocities, impact angle has minimal effect on material removal. At low velocities the eroding particle has lower energy, hence, it's ability to induce permanent deformation and fracture is limited. The ratio of elastic to plastic deformation is high, i.e., a significant portion of the impact energy is consumed in deforming the coatings elastically. This trend has also been seen for materials in solid particle erosion [64]. Figure 4-35 (b) shows the correlation between volume loss and impact angle for each coating tested at 52 m/s. In comparison, samples tested at 35 m/s had smaller impact craters relative to the samples tested at 52 m/s, which is similar to results found in the literature [64, 112]. The 5.14 wt.% NiTi and 7.02 wt.% NiTi coatings experienced the highest volume loss at 90°, which is typical of brittle materials [113]. On the other hand, the 6.07 wt.% NiTi coating exhibited the highest volume loss at 45 °, consistent with the behaviour of ductile materials. Therefore, in terms of material removal, the 6.07 wt.% coating can be classified as the most tough relative to the other coatings being studied. Furthermore, even at a low impact velocity of 35 m/s, the 6.07 wt.% NiTi coating exhibits a ductile behaviour (Figure 4-35 (a)). Here, the maximum erosion volume loss takes place at an impact angle of 45 ° and drops as the impact angle is increased to 90 °. However, the ductile characteristics at low speed is less pronounced than at high speeds.

a)

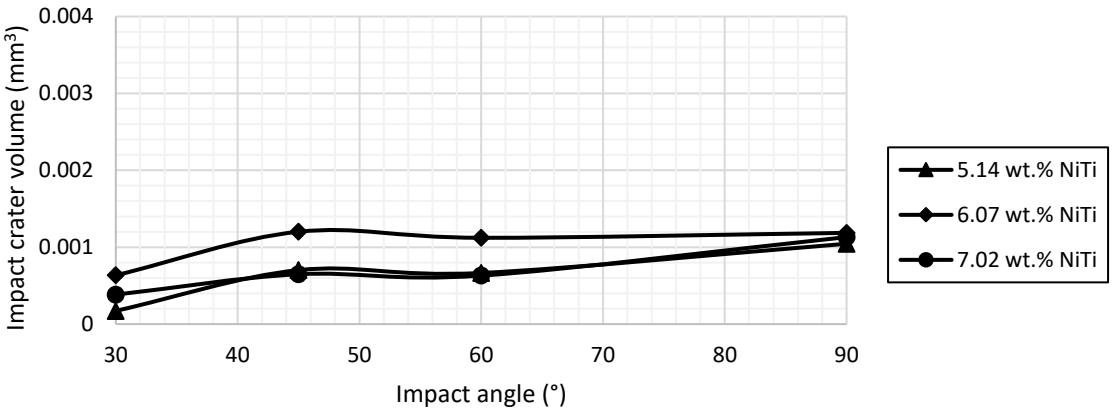

b)

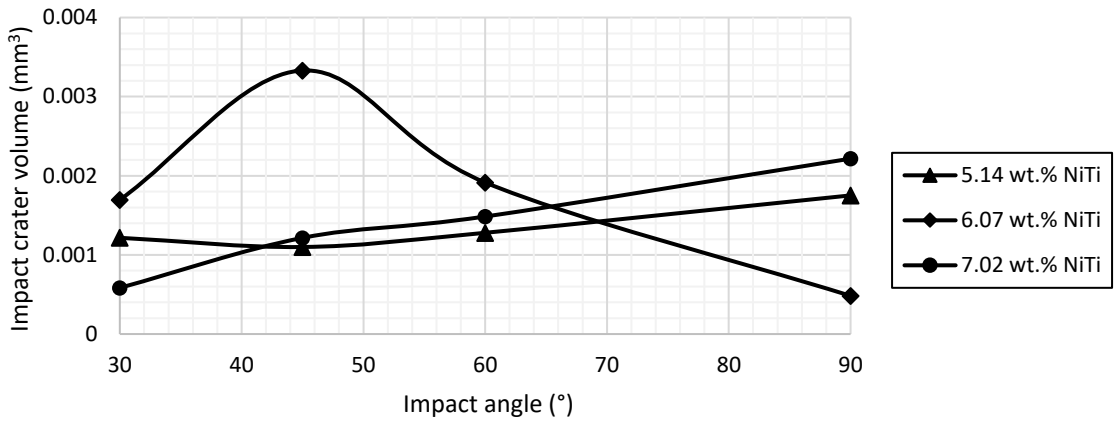

Figure 4-35 Volume loss as a function of impact angle with average testing velocity of a) 35 m/s and b) 52 m/s

From the volume loss results, it is clear that the 6.07 wt.% NiTi coating performed better under these conditions in terms of toughness. It is likely that the 5.14 wt.% NiTi coating did not contain enough superelastic NiTi to drastically change the behaviour. On the other hand, the 7.02 wt.% NiTi coating likely contained too many nano-particles, leaving the samples subject to agglomeration and higher stress concentrations on the surface. This could result in more fracture, consistent with a brittle material. Therefore the 6.07 wt.% NiTi contained the optimal concentration of NiTi particles for erosive conditions.

4.5.2 Erosion Mechanisms

As samples tested at 35 m/s showed less damage than those tested at higher speeds, select SEM/ OM was done on low (30 °) and high (90 °) angle impact sites at 52 m/s testing speed to examine and determine the erosion mechanisms. The impact crater subjected to high impact angle is circular, while that impacted at low angle is elliptical in shape, as seen in Figure 4-36. The size of the normal impact crater is larger than that of the low angle impact, as expected, due to the fact that more energy was transferred to forming the crater, whereas

in the case of the low angle impact, some of that initial kinetic energy is dissipated due to frictional forces [114, 115].

Evidence of cracking was seen in the composite coatings, as evident in the optical images in Figure 4-36. Cracks appear to be shallow and concentrated in the vicinity of the impact crater. Radial and ring cracks are present at both low and high angle impacts in the Ni-P matrix. It is believed that the ring cracks are Hertzian-type. This type of crack forms on the surface just outside the contact area where the radial stress reaches its maximum tensile value [116, 117]. Radial cracks also develop on the surface but are caused by the maximum tensile hoop stress [118]. Hoop stress becomes positive (tension) on the surface during elastic-plastic contact which applies in this scenario [119]. Both radial and ring cracks initiate when the applied load exceeded a critical value. In a recent study, Yonezu et al investigated fracture mechanisms of electroplated Ni-P on steel under static indentation conditions [120]. They suggested that ring crack formation alters the subsequent stress distribution during indentation, as a result tensile hoop stress develops upon unloading. They also proposed that radial cracks initiate near the ring crack tip at the coating/substrate interface. This phenomena is similar to that occuring during single particle impact of the composite coatings. The 5.14 wt.% NiTi coating shows predominantly Hertzian cracks, while coatings containing higher amounts of NiTi show significant Hertzian and radial cracks.

It is interesting to note that at lower angles (i.e. 30 °), Hertzian cracking occurs at the initial point of contact but not on the other side of the crater where the impacting particle leaves the surface. This is similar to cohesive failure during sliding contact, where Hertzian-type cracks are a result of tensile stress behind the indenter [121]. Radial cracks do not appear on the side of the crater where the initial impact takes place, but are clearly seen on the opposite side. This finding suggestes that cracking pattern is incident angle dependent in erosive processes. Here, the behaviour could be attributed to the changes in the stress distribution during low angle impact. In the case of higher impact angles (i.e. 90 °), Hertzian and radial cracking is present around the perimeter of the impact crater similar to static indentation loading examined in section 4.4. There is also a closed crack network inside the crater as a result of erodent particle induced compaction.

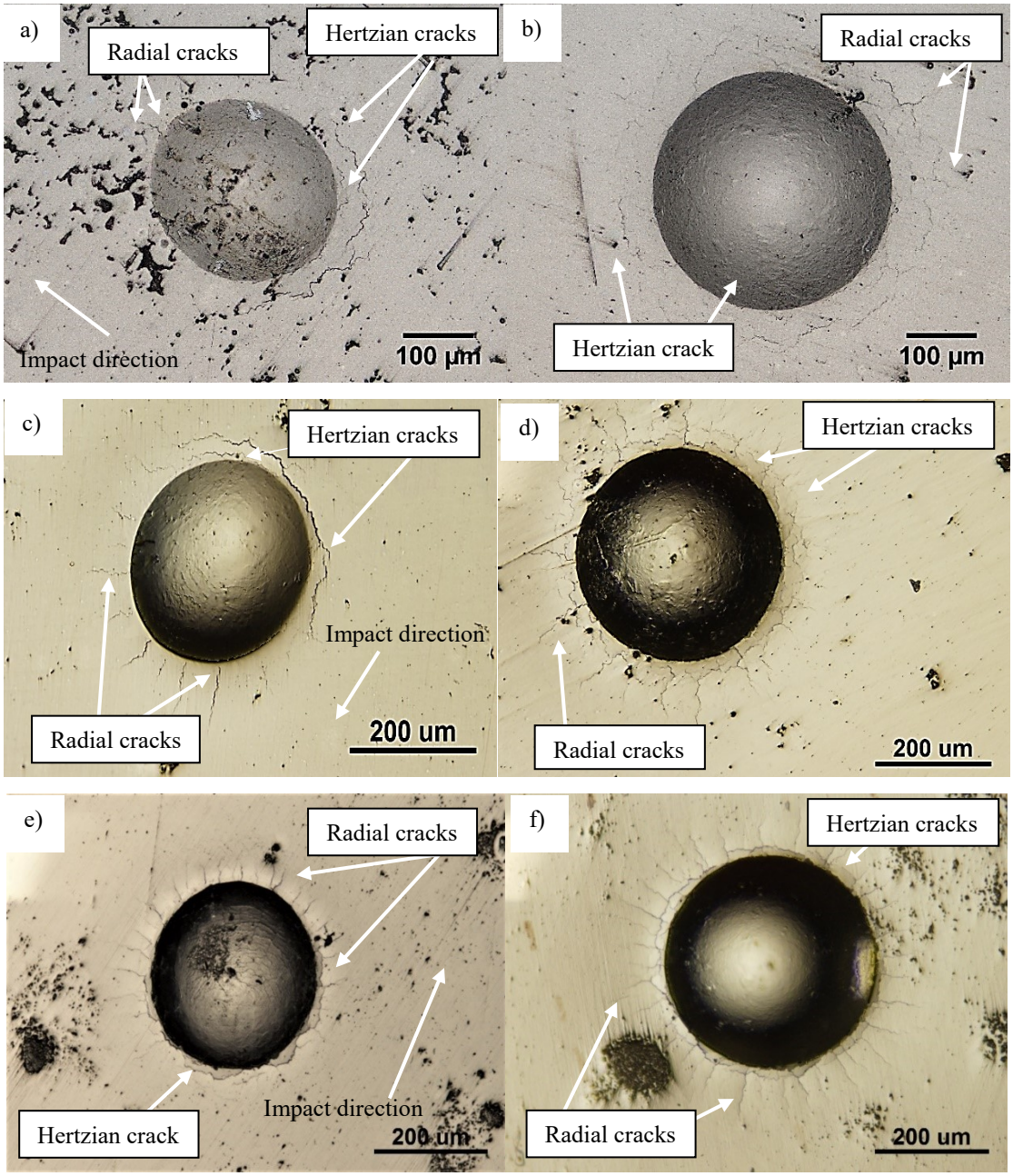

Figure 4-36 Erosion behaviour showing evidence of Hertzian and radial cracking in a), c), e) low angle and b), d), f) high angle impact for 5.14 wt.%, 6.07 wt.% and 7.02 wt.% NiTi coatings respectively

Crater depths are higher at normal impact due to the fact that nearly all energy is transformed into work being done to form the crater, while at lower angles frictional forces reduce the total energy being transferred from the erodent particle to the surface [115, 122]. It is evident from the crater images and profiles in Figure 4-37-Figure 4-39 that the impact

craters formed by squeezing the material outside the crater. At low impact angles, pile-up forms in front of the impacting particle as it contacts the coating surface. This can be seen in the line profile at the center of the crater and along the major axis of the elliptical crater. Here, it is clear that pile-up is formed as the erodent particle displaces the coating during impact.

The normal impact reveals that material build-up forms evenly around the edges of the crater, as seen in the line profiles. Similar to low angle impact, material build up induces tensile stresses around the crater and assist in initiating Hertzian type cracks (seen in the optical images above). As described earlier, the cracks on coatings subjected to both low and high impact angles appear to be shallow and occur at the top surface layers where tensile stresses are highest. The coating containing 7.02 wt.% NiTi exhibits the highest crater depths in comparison to coatings with lower amounts of NiTi. Similar instances have been seen with both scratch and indentation behaviour at high loads, as the hardness of the 7.02 wt.% NiTi coating is lower than that of the coatings containing less NiTi and therefore it is more susceptible to deformation.

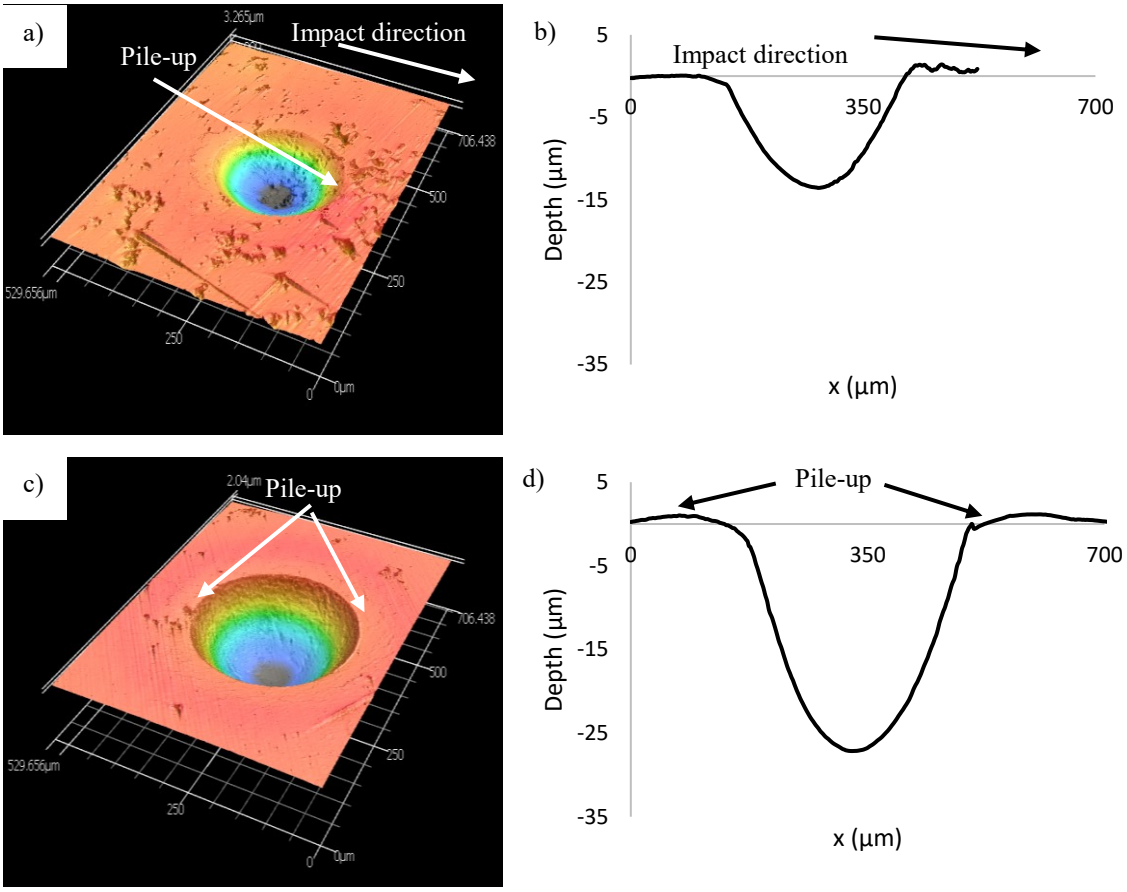

Figure 4-37 Respective 3D surface and depth profiles of a), b) low impact and c), d) high impact for 5.14 wt.% NiTi coating

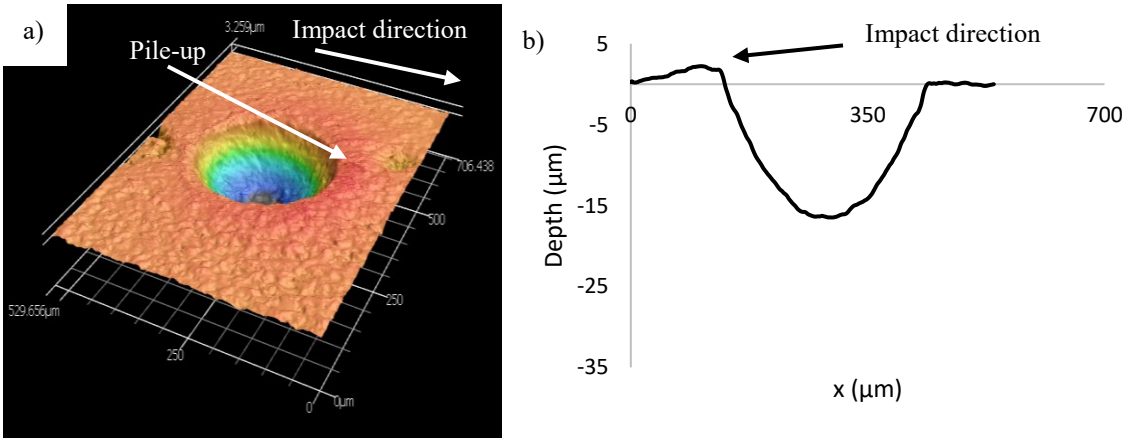

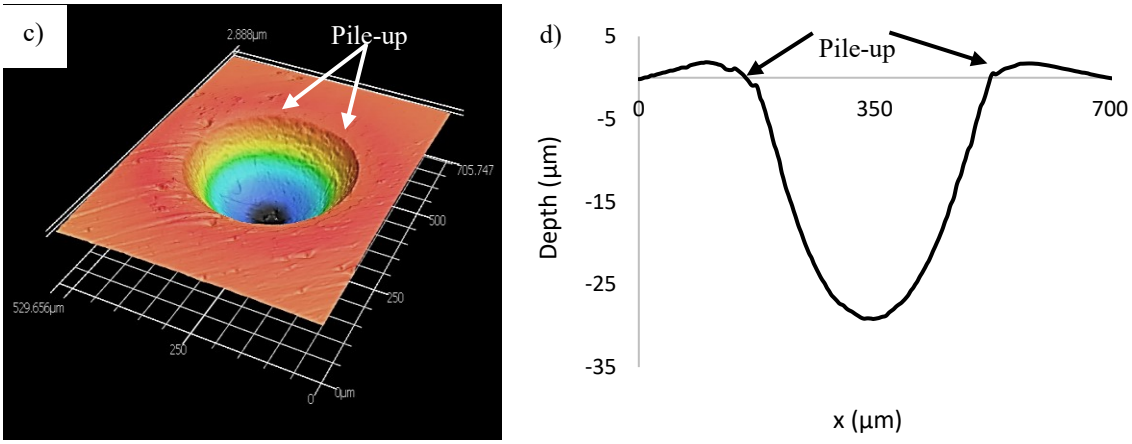

Figure 4-38 Respective 3D surface and depth profiles of a), b) low impact and c), d) high impact for 6.07 wt.% NiTi coating

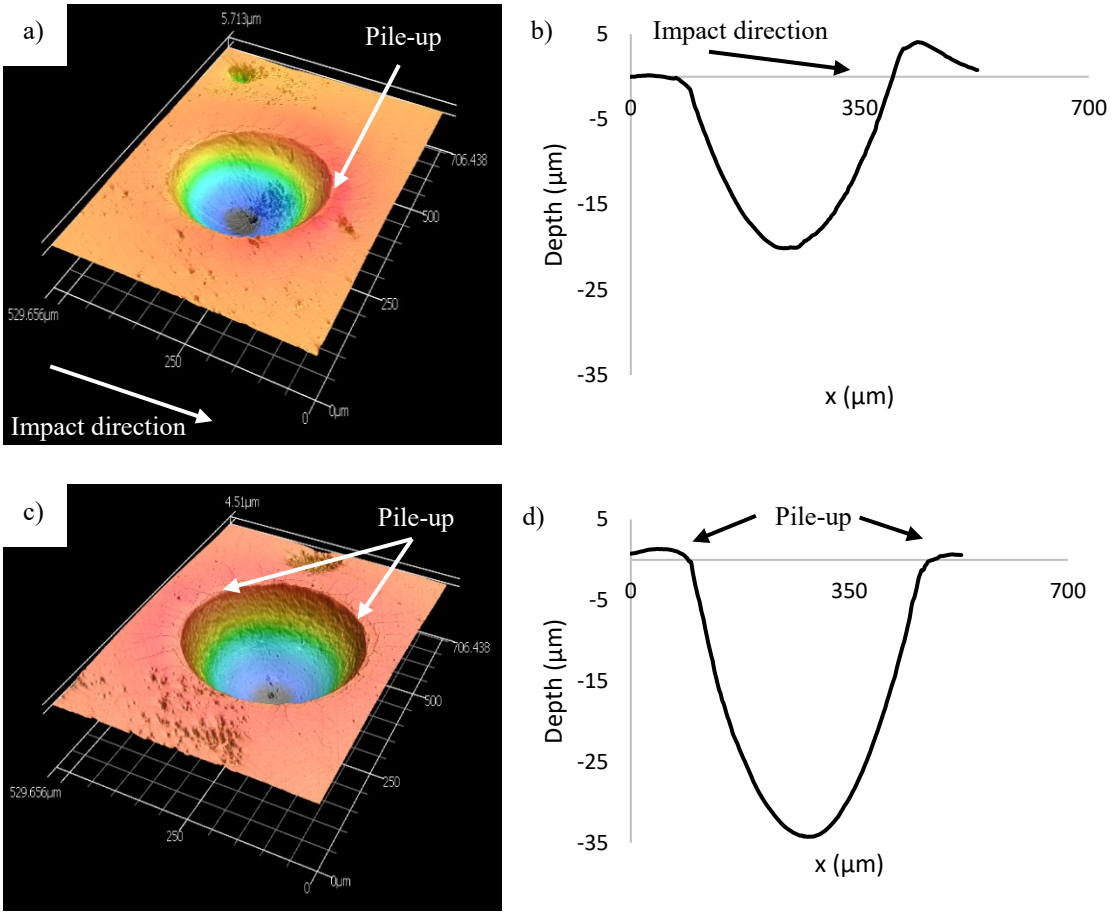

Figure 4-39 Respective 3D surface and depth profiles of a), b) low impact and c), d) high impact for 7.02 wt.% NiTi coating

Severe damage inside the crater was observed in the 7.02 wt.% NiTi, in comparison to the other coatings, further solidifying the assumption that higher amounts of NiTi result in higher stress concentrations on the surface, resulting in higher probability of brittle fracture. In Figure 4-40, severe cracking is seen both inside and outside of the impact site, with delamination occurring within the impact site.

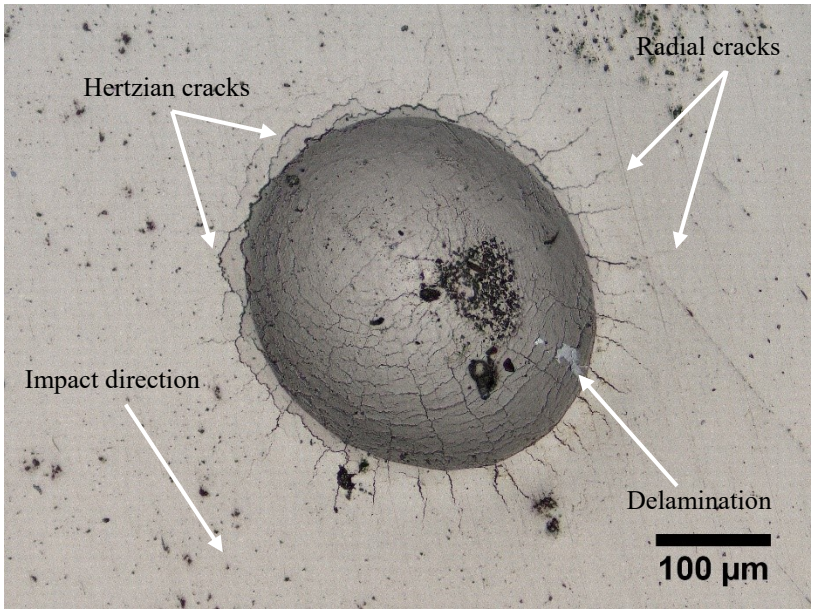

Figure 4-40 Confocal microscope image of 7.02 wt.% NiTi coating under low angle impact showing severe cracking and delamination

As mentioned above, evidence of closed cracks was seen in the inside of the impact sites. An example of this can be seen in Figure 4-41. Upon initial impact, cracks begin to initiate and propagate at stress concentrations throughout the matrix. As the particle pushes through the surface, two things may occur. The first, being that due to the compression forces, the cracks that form on initial impact eventually close shut as the particle travels through the material. Secondly, these cracks are forced to close due to the stress associated with volume expansion of the superelastic particles during transformation from austenite to martensite (discussed in more detail in section 4.7).

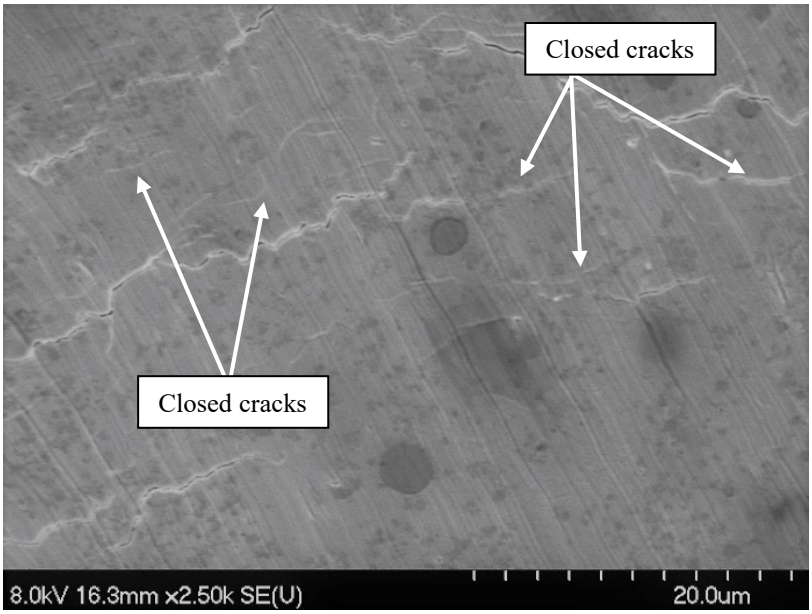

Figure 4-41 Network of closed cracks in impact crater of 6.07 wt.% NiTi coating under normal impact

Erosion and toughening mechanisms of the Ni-P-nano-NiTi composite coatings are summarized in the following schematics. Under low angle impact, the composite coated surface shows evidence of Hertzian fracture upon initial impact (Figure 4-42(a)), followed by the propagation of radials in the direction of impact. It was found that upon normal impact (Figure 4-42 (b)), where the highest energy is transferred to producing the impact crater, an intricate network of Hertzian and radial cracks are seen in the composite coatings. These mechanisms for both angles are also coupled with toughening mechanisms due to the addition of superelastic NiTi, including crack deflection/ bridging, micro-cracking and transformation toughening which will be discussed in more detail in further sections. The following sequences of events has been derived from the present study for the composite coatings:

1. WC-Co particle hits the coated surface inducing stress on the surface
2. Material is squeezed to the side of the impact in order to form an impact crater
3. Hertzian cracks initiate and propagate in the Ni-P matrix, which has low fracture toughness
4. The change in stress distribution due to Hertzian cracking initiates radial cracking and propagation in the Ni-P matrix

5. As the particle travel through the material, high compression forces can cause cracks inside the stress field to close
6. Cracks continue to propagate until they come into contact with superelastic NiTi particles which either bridge, deflect, or close the cracks completely inside and outside of the contact stress field

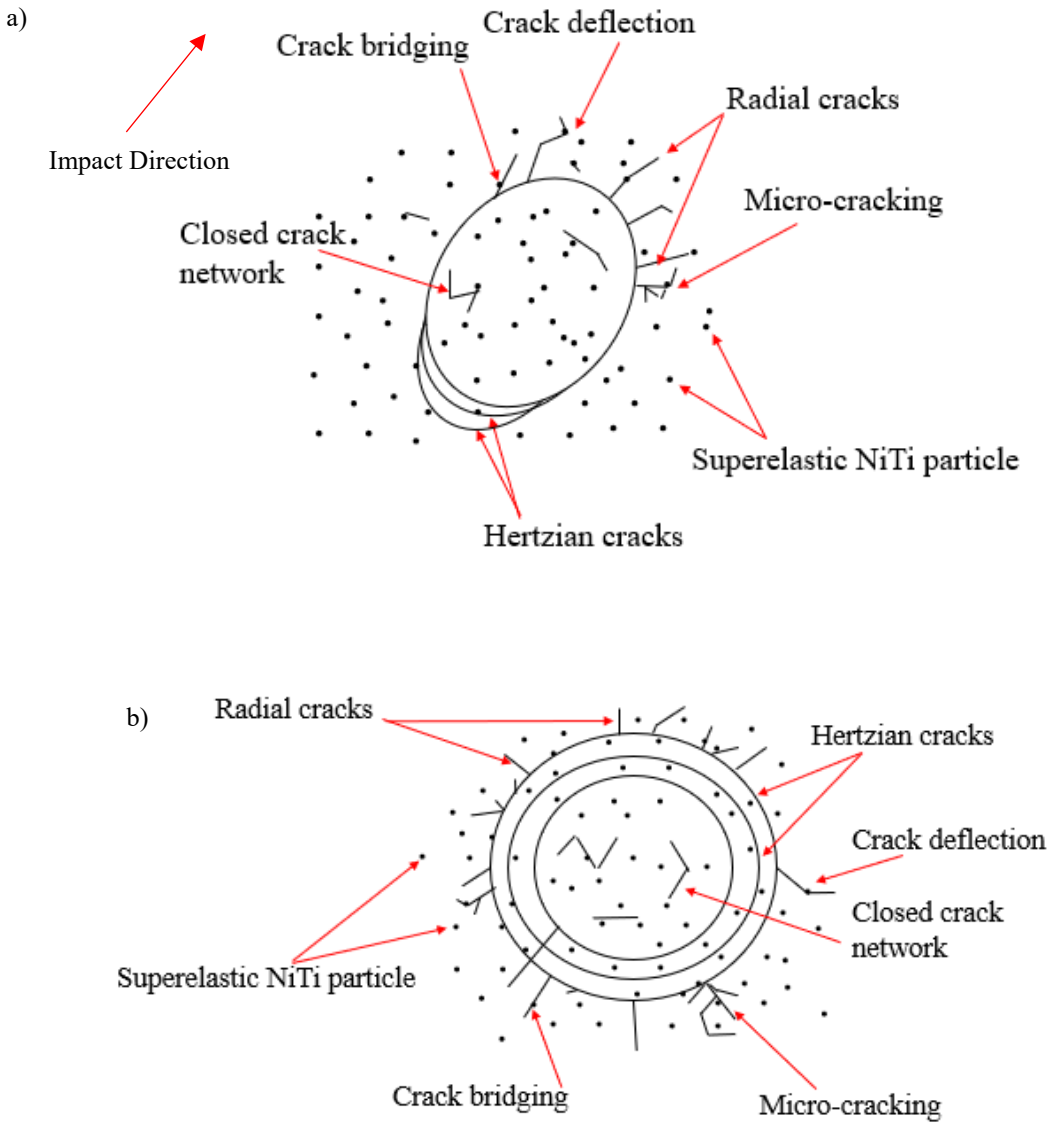

Figure 4-42 Schematic of erosion and toughening mechanisms of composite coated surface under a) low angle impact and b) normal impact

4.6 Bending Performance

4.6.1 Examination of Acoustic Emission Signals

Acoustic emission was monitored during bend testing in order to identify any cracking or failure events in the coatings. The monolithic Ni-P coating shows large spikes in acoustic emission beginning at shortly after 1.5 mm displacement (Figure 4-43 (a)). These large spikes are due to energy being released during cracking in the coating. Cracking is frequent due to the brittle nature of the monolithic coatings. The addition of superelastic NiTi subdued the acoustic emission energy, as shown in Figure 4-43 (b), (c) and (d). The 5.14 wt.% NiTi coating still showed spikes in acoustic emission energy (indicating cracking), however, the magnitude of the energy was less than that of the monolithic Ni-P coating, suggesting that cracks are less severe. The spikes in AE are also less frequent than that of the monolithic coating, meaning fewer cracks are propagating throughout the coating. The onset of cracking is delayed in comparison to the monolithic coating, showing that the composite coating requires higher strain to initiate cracking. This indicates an increase in fracture toughness in comparison to the monolithic coating.

The 6.07 and 7.02 wt.% NiTi coatings showed minimal activity at low displacements, however, at higher displacements the coatings experienced delamination. This is represented in the AE signals as large spikes in energy, much higher than those observed in the monolithic Ni-P coating during cracking (approximately 3000 J). Minimal cracking was seen prior to delamination in both coatings. This suggests that the coatings did not fail due to the coating reaching a critical stress during testing, rather they likely failed due to high residual stresses in the matrix. This is further supported by the fact that this delamination occurs sooner with the addition of further wt.% NiTi. Higher particle concentrations result in higher amounts of stress concentrations within the coating and these high stress concentrations make cracking and coating failure easier. Anazi et. al found that high concentrations of oxidized particles in HVOF AMDRY 9954 coatings were causes of high stress concentrations resulting in easier crack initiation [123]. So, the bonding of the coatings will fail before the coatings themselves fail. Therefore, it can be

determined that the addition of superelastic NiTi results in an increase in the toughness in comparison to the monolithic Ni-P coating to a certain extent. However, the concentration of NiTi must be optimized to avoid debonding while diminishing crack severity.

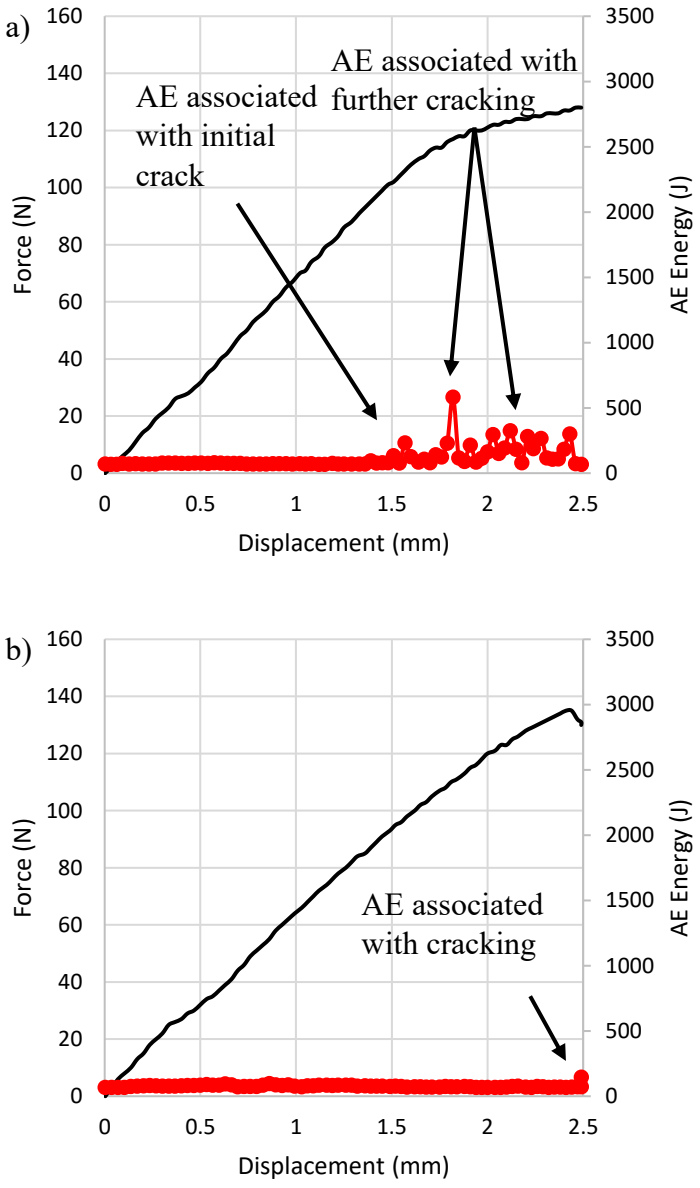

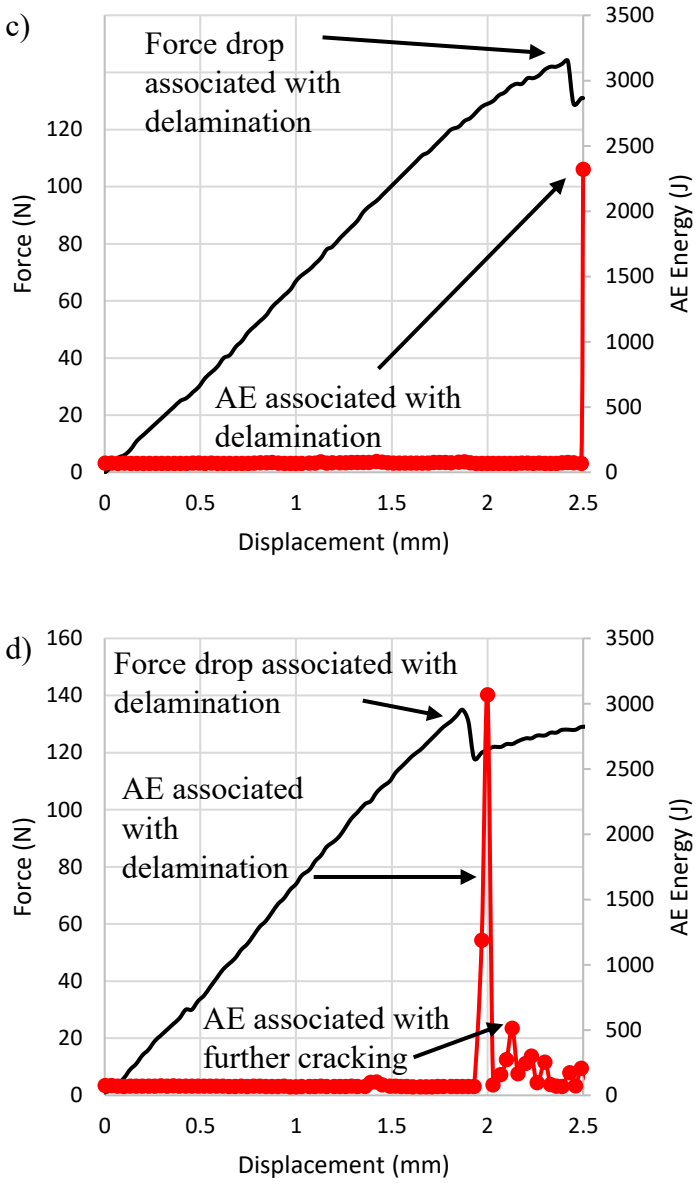

Figure 4-43 Load-displacement curves with AE energy for a) monolithic Ni-P coating, b) 5.14 wt.% NiTi coating, c) 6.07 wt.% NiTi coating, and d) 7.02 wt.% NiTi coating

4.6.2 Optical Confirmation of Cracking Events

The use of optical microscopy to analyze the coatings after testing confirmed the presence of cracks and delamination as previously indicated from the data above. Figure 4-44 shows the orientation of cracks on the coating surface extending into the substrate. Figure 4-45 (a), (b), (c), (d) show optical images of cracks on the coating surface (in the x direction of Figure 4-44).

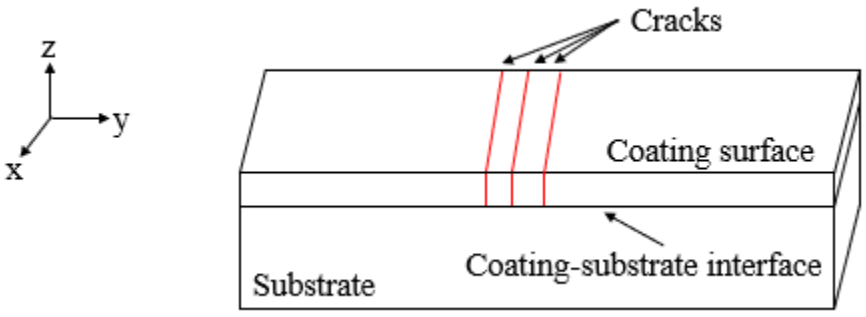

Figure 4-44 Schematic showing orientation of cracks on coating surface

As seen in Figure 4-45 (a), the monolithic coating showed evidence of major cracking. No visible cracks were seen on the 5.14 wt.% NiTi coating surface (Figure 4-45 (b)), however as mentioned above there are changes in acoustic emission, which leads to the conclusion that in comparison to the monolithic coating the cracks are micro-size and are not visible on the same scale compared to the monolithic Ni-P. As discussed previously, the addition of 6.07 wt.% NiTi to the matrix results in delamination due to high residual stresses responsible for poor adhesion, with presence of some micro-cracks as seen in Figure 4-45 (c). Due to the higher amount of NiTi present, there is a higher amount of stress concentrations present and thus crack initiation is easier. Similar failure modes were seen with the 7.02 wt.% NiTi coating showing predominantly delamination (Figure 4-45 (d)), therefore confirming the fact that higher amounts of NiTi induce higher amounts of stress within the coating therefore leading to premature bonding failure in comparison to coatings with less NiTi incorporated into the matrix. Small micro-cracks were also seen within the coatings which reiterates the fact that higher stress concentrations on the surface increase the likelihood of cracking. Therefore, for bending applications NiTi content should be kept

low in the coatings to minimize probability of major cracking and reduce the risk of delamination from the substrate.

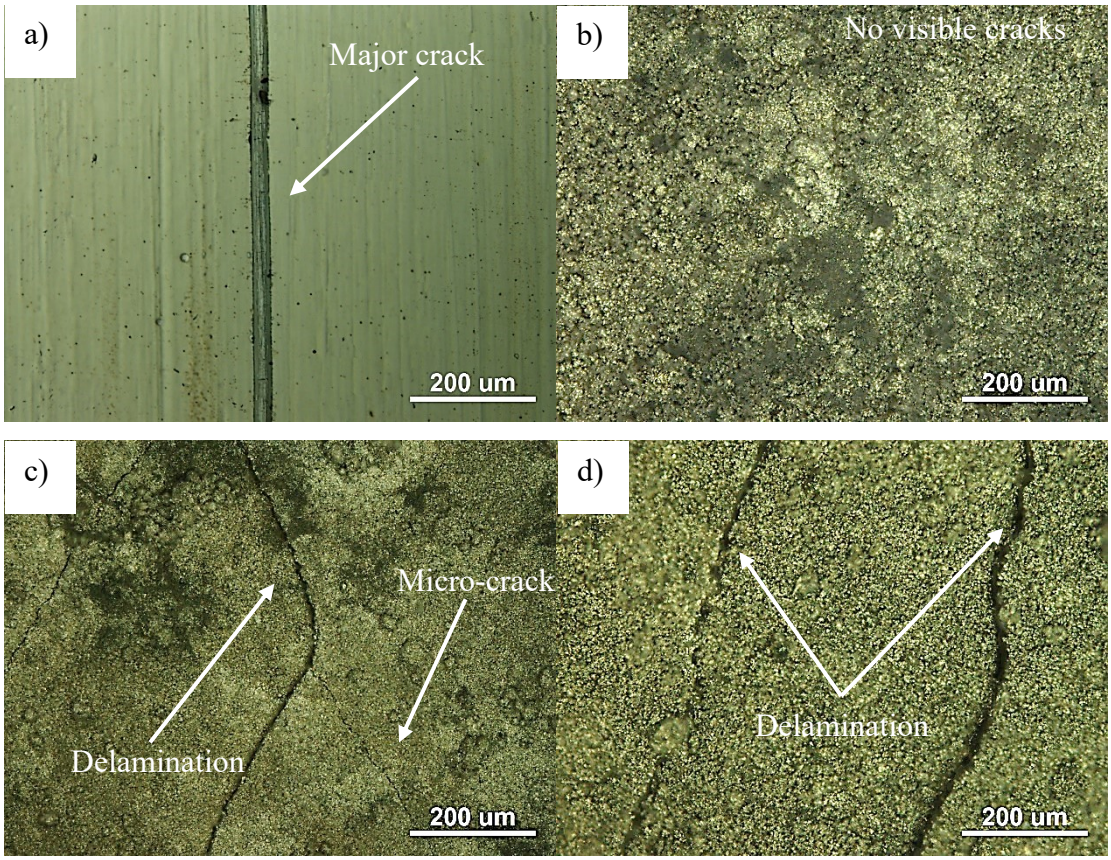

Figure 4-45 Optical image of surface of a) monolithic Ni-P coating, b) 5.14 wt.% NiTi, c) 6.07 wt.% NiTi and d) 7.02 wt.% NiTi under 2.5 mm displacement

4.7 Evidence of Toughening

Through extensive SEM analysis on the composite coating samples after testing done in sections 4.2-4.4, several toughening mechanisms were identified, including crack bridging, crack deflection, crack arresting, micro-cracking, and transformation toughening. As the cracks initiate through the Ni-P matrix, the propagation energy is significantly reduced by these mechanisms. Without superelastic additions, the matrix would be subject to further

crack propagation and failure. The aforementioned mechanisms are discussed in detail below.

4.7.1 Crack Bridging, Deflection, and Arresting

Bridging and deflection of cracks was identified in the samples containing superelastic additions. As a crack attempts to propagate, its propagation is hindered or arrested by the presence of superelastic NiTi particles. Due to the high ductility that is a result of the reversible martensitic transformation that these particles undergo, they are capable of absorbing higher amounts of energy in comparison to the brittle Ni-P matrix [124]. Thus, energy at the crack wake will be consumed by the particles upon interaction as the energy previously used for crack propagation will be used to plastically deform the second phase particles. After this, the crack will have less energy for continuation of propagation, reducing its severity. Both toughening mechanisms have been seen in the literature when micro and nano-sized particles are added to a ceramic matrix, with the additions clearly dictating the crack path [125, 126].

Figure 4-46 (a) shows evidence of crack bridging in the 5.14 wt.% NiTi coating under 600 N static indentation load. As the load is applied to the coating surface, tensile stresses are generated as a result of contact between the surface and the indenter, causing crack formation. Presence of superelastic NiTi particles hinder these cracks from growing into major cracks by absorbing the propagation energy. In some cases, where propagation energy is lower, the superelastic NiTi particles can absorb enough of the energy to arrest the crack. An example of this was seen in the 7.02 wt. %NiTi coating under 1500 N static indentation (Figure 4-47).

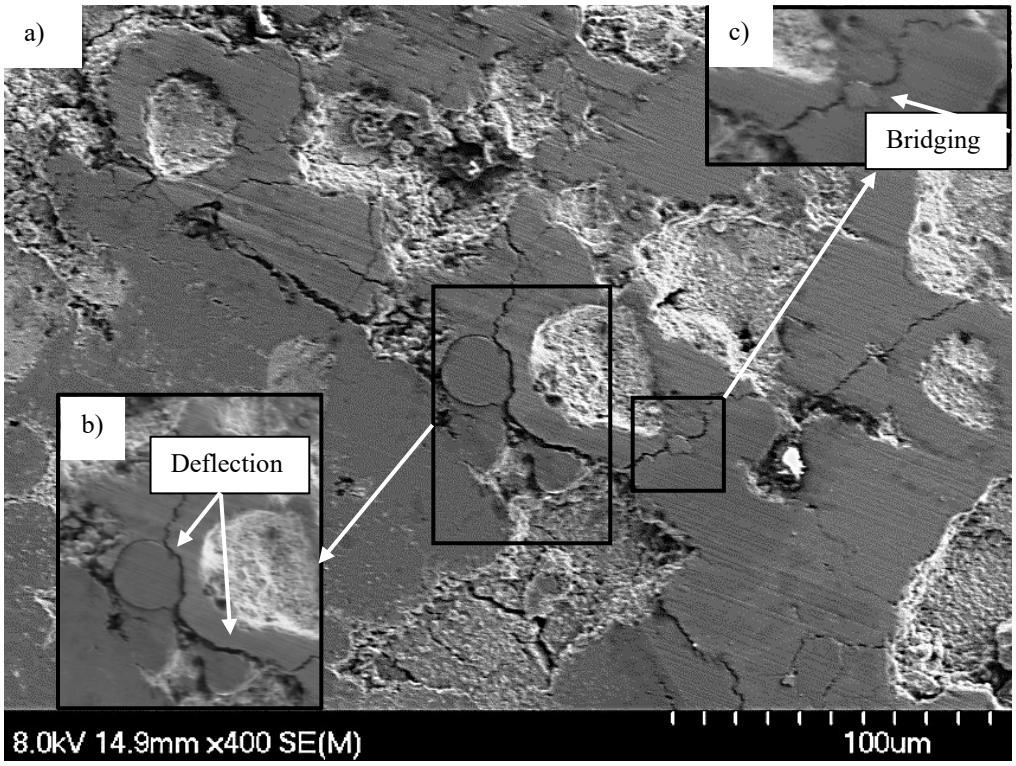

Figure 4-46 a) SEM image of indentation of 5.14 wt.% NiTi coating under 600 N showing crack b) deflection and c) bridging

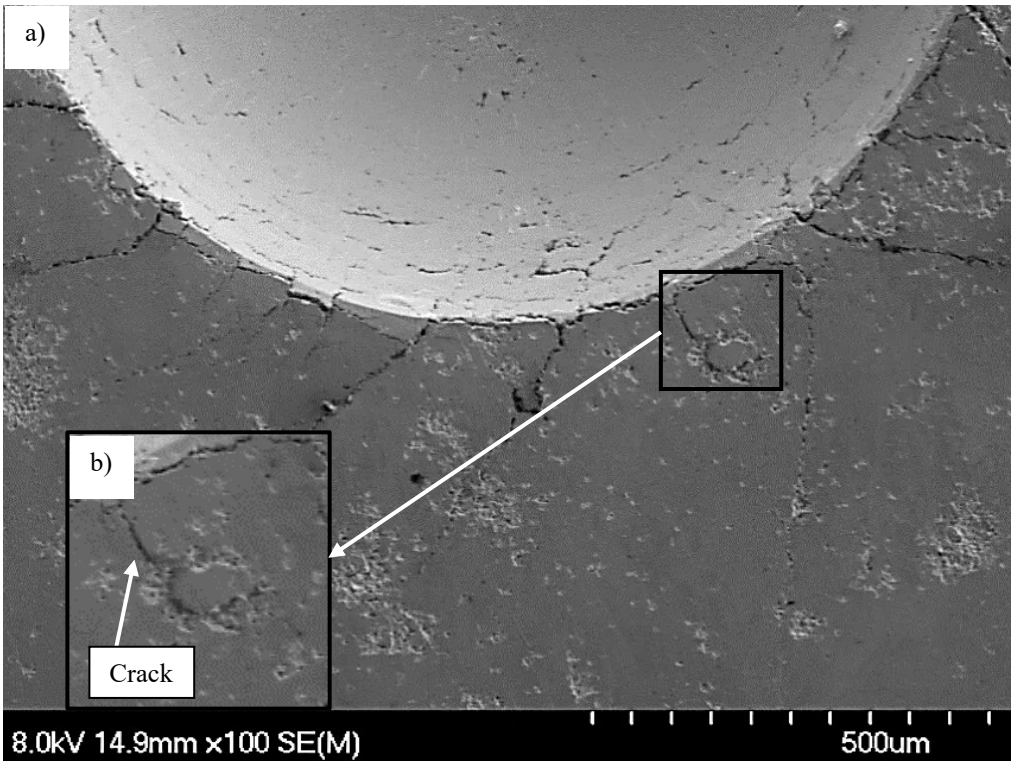

Figure 4-47 a) SEM of indentation of 7.02 wt.% NiTi coating under 1500 N max load b) example of crack arresting

Similar instances were seen during single particle erosion testing. Figure 4-48 (a) shows evidence of crack deflection in the erosion impact crater due to the presence of a NiTi particle. Presence of NiTi particles was confirmed using EDS mapping, as seen in Figure 4-48 (b). Crack bridging was also seen in the composite coatings (Figure 4-49, Figure 4-50). This, like crack deflection, reduces the severity of the crack as the NiTi particle once again absorbs propagation energy by acting as a barrier to crack propagation.

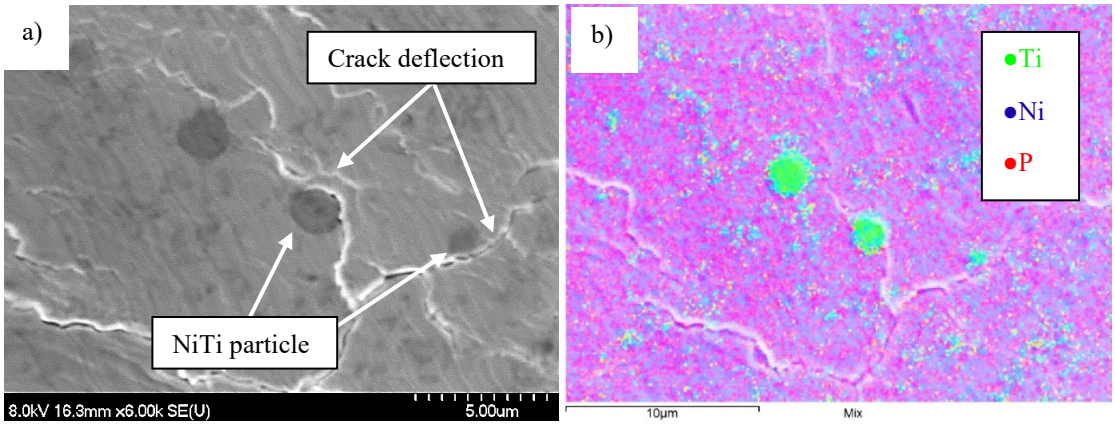

Figure 4-48 (a) SEM image and (b) EDS map of evidence of crack deflection in 6.07 wt.% NiTi composite coating under normal impact

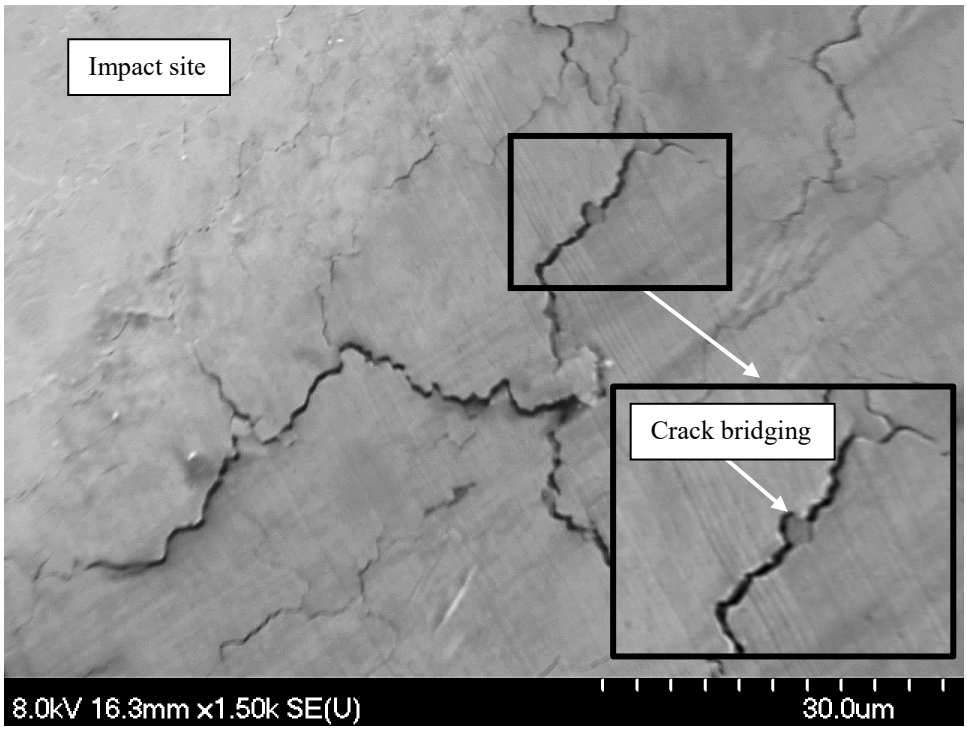

Figure 4-49 Evidence of crack bridging in 6.07 wt.% NiTi composite coating under normal impact

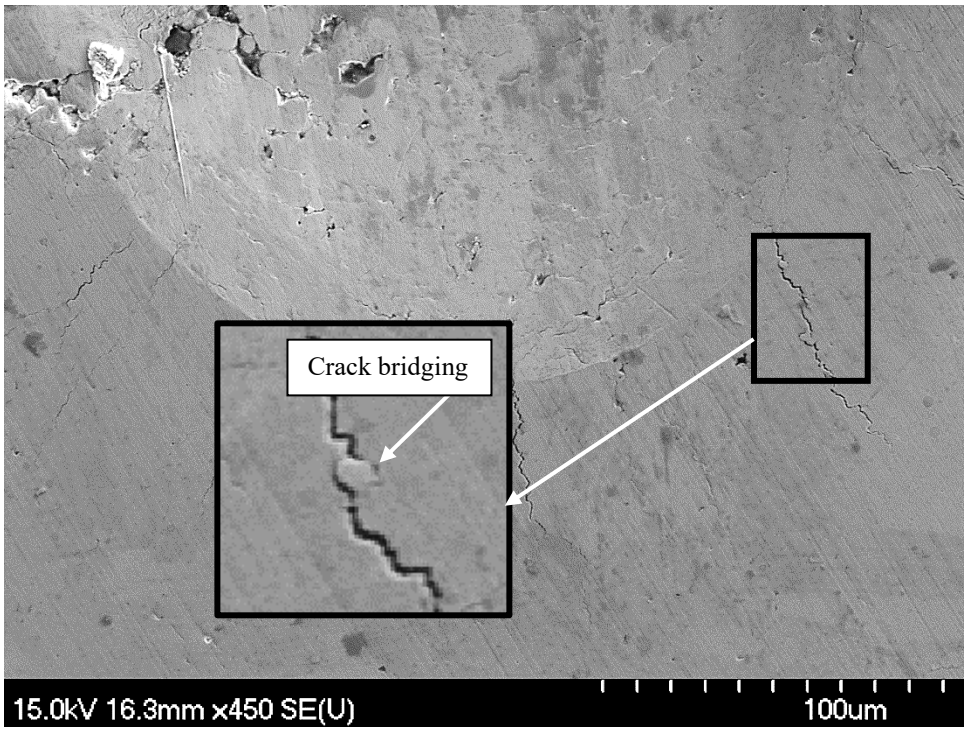

Figure 4-50 Evidence of crack bridging in 6.07 wt.% NiTi coating under single particle impact at 60 ° impact

4.7.2 Micro-cracking

While the formation of major cracks in materials is typically undesirable, it has been found that the formation of micro-cracks near the initial crack site can be beneficial in increasing fracture toughness in brittle materials [127, 128]. In composites, micro-cracking has been found to be beneficial in reducing energy that would otherwise propagate major cracks. The dominant toughening mechanism seen under scratch test conditions was micro-cracking. Figure 4-51 shows evidence of micro-cracking within the wear track of the 5.14 wt.% NiTi coating under increasing load conditions. As shown in Figure 4-51 (a), micro-cracks branch from the larger cracks, which aids in reducing the severity a single propagating crack. These smaller cracks prevent catastrophic failure should the coating be subjected to high tensile stresses. Evidence of bridging by NiTi particles is also observed

(Figure 4-51 (b)), indicating the simultaneous effects of several different toughening mechanisms within the coatings.

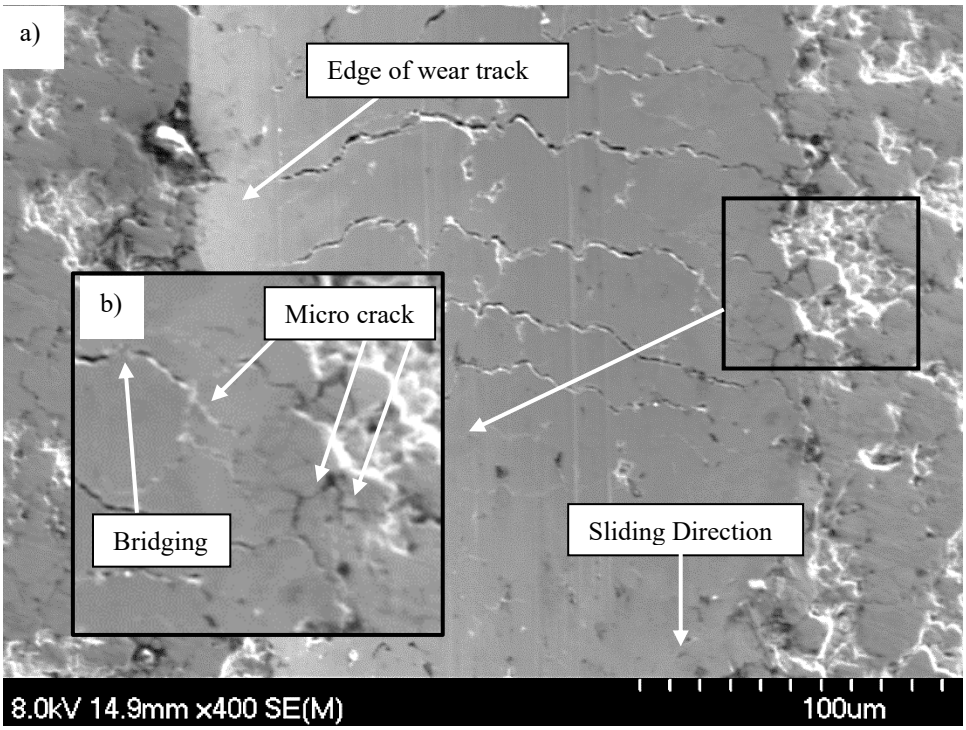

Figure 4-51 a) Wear track of increasing load on 5.14 wt.% NiTi coating and b) evidence of micro-cracking and crack bridging

Micro-cracking effects in the coatings can be quantitatively analyzed by calculating the crack density. In order to evaluate the effect of the NiTi on the toughness of the coatings, crack density was measured for static indentation tests. Four radial cracks were measured for each load for each sample and an average length (R) was measured with respect to the radius of the indent (a) using optical microscopy. As expected, crack length was found to increase with load. It was found that the 5.14 wt.% NiTi had the lowest R/a value on average, followed by the 7.02 wt.% NiTi and finally the 6.07 wt.% NiTi coating. In general, the composite coatings had a lower R/a value than the monolithic Ni-P coating, meaning that the presence of NiTi particles can limit the length of cracks in Ni-P matrix. This is represented graphically in Figure 4-52. The highest standard deviation was seen with the coating containing the highest amounts of NiTi. Having more NiTi results in more stress concentrations on the surface which results in a higher probability of crack initiation.

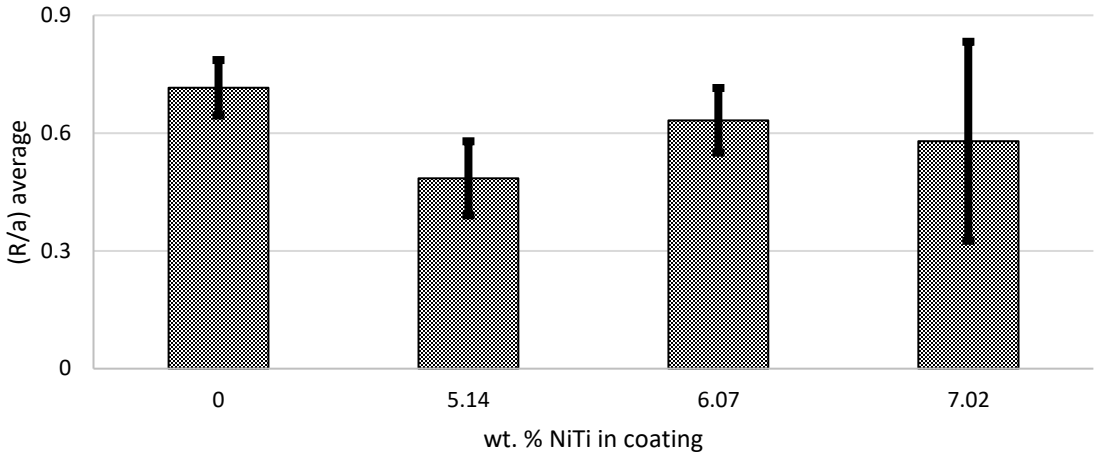

Figure 4-52 Effect of wt.% NiTi in coating on average length of radial cracks with respect to indent radius

Micro-cracking was observed in the composite coatings at both high and low angle conditions under single particle impact. Evidence of this can be seen in Figure 4-53. The presence of superelastic NiTi particles in the matrix may break up larger cracks into micro-cracks. In the process of crack deflection and bridging, larger cracks may break up into finer cracks with lower propagation energy.

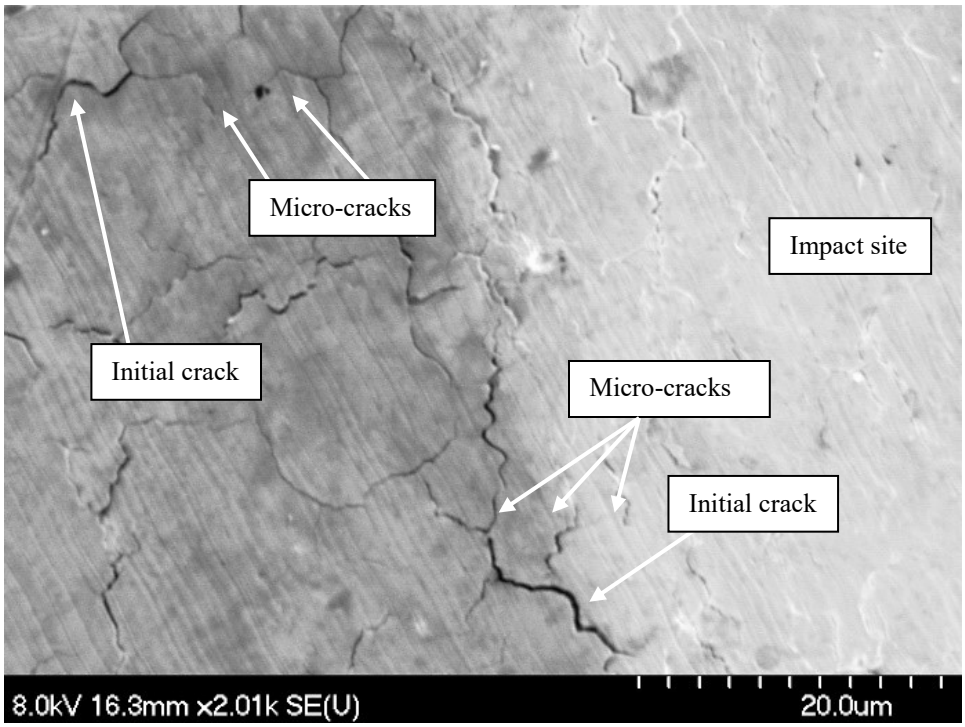

Figure 4-53 SEM image of extensive network of micro-cracks observed at the edge of impact site of 6.07 wt.% NiTi under normal impact

4.7.3 Transformation Toughening

In order to initiate the reversible martensitic transformation, the contact stress during testing must be greater than the transition stress. In the literature, this stress has been reported to be approximately 410 MPa at room temperature [129]. Transformation toughening was expected to take place during scratch, indentation and erosion testing, due to the fact that the Hertzian contact stresses used during scratch, indentation and single particle erosion testing are higher than those required to initiate the austenite to martensite phase transformation (σ_{fs}). The mean contact pressure during testing was calculated using Hertzian contact theory for the elastic contact between a sphere and an elastic half-space, given by equations in Chapter 2. For the case of the elastic contact between a sphere and a half space, R is assumed to be the radius of the indenter.

For scratch testing, assuming that v = 0.29, E = 198 GPa for Ni-P [130], and v'=0.20 E = 1050 GPa for the diamond indenter [131], then the mean contact pressure will range between 2.87-12.85 GPa which is higher than that of the stress required to initiate the transformation from austenite to martensite, leading to transformation toughening during testing. For indentation testing, where E = 600 GPa, and v = 0.26, the mean contact pressure was found to range between 11.64-18.73 GPa for the given indentation loads. Lastly, for single particle impact (based on WC and Ni-P values above), the p_m was found to range between 460-600 MPa and therefore is high enough to initiate the reversible transformation as well.

By examining the coatings under SEM, it was noticed that in many cases, cracks would not be deflected or bridged by the particles, rather they would surround the particles without ever coming into contact with the second phase. It is believed that this is due to a compression field that is generated around the particles whilst undergoing a volumetric change due to the stress induced martensitic transformation from austenite to martensite. This compression force can cause the cracks near the particles to close, providing evidence of transformation toughening. This is important in order to avoid crack propagation and has been seen in ZrO_2 alloys that are capable of undergoing the same martensitic transformation [132, 133, 134]. Evidence of transformation toughening was seen under several different conditions, including micro-Vickers indentation as well as single particle impact.

An example of this can be seen in the 6.07 wt.% NiTi coating under 50 g micro-Vickers load in Figure 4-54. During indentation, the stresses generated are high enough to initiate cracking and the reversible martensitic transformation. As the indenter moves further into the material and the crack tries to propagate, the superelastic NiTi particles are simultaneously undergoing a volumetric change caused by the increase in stress. This distortion in crystal lattice results in a compressive strain field surrounding the particles, and thus as the cracks try to propagate further, they are stopped and even closed by this field.

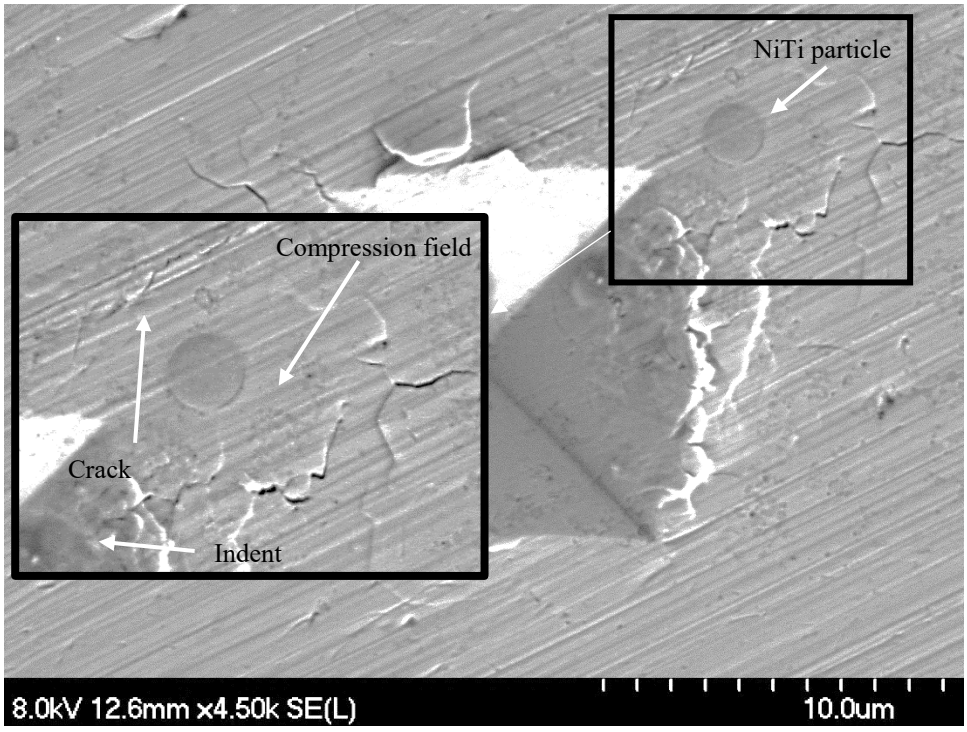

Figure 4-54 Example of transformation toughening in coating cross-section initiated by micro-Vickers indentation loads

This mechanism was also seen under single particle impact, as shown in Figure 4-55. As the particle shown is within the impact site, it is likely that the compression force discussed in section 4.5.1 worked in combination with transformation toughening to close the crack shown. The fact that the cracks are surrounding the superelastic NiTi particle (insert of Figure 4-55) provides a strong indication that a compression field around the particle prevents the cracks from propagating through this field. When a crack attempts to propagate through or near a particle, the tensile stress is high enough around the crack such that the transition stress is reached, and the particle undergoes a change from austenite to martensite.

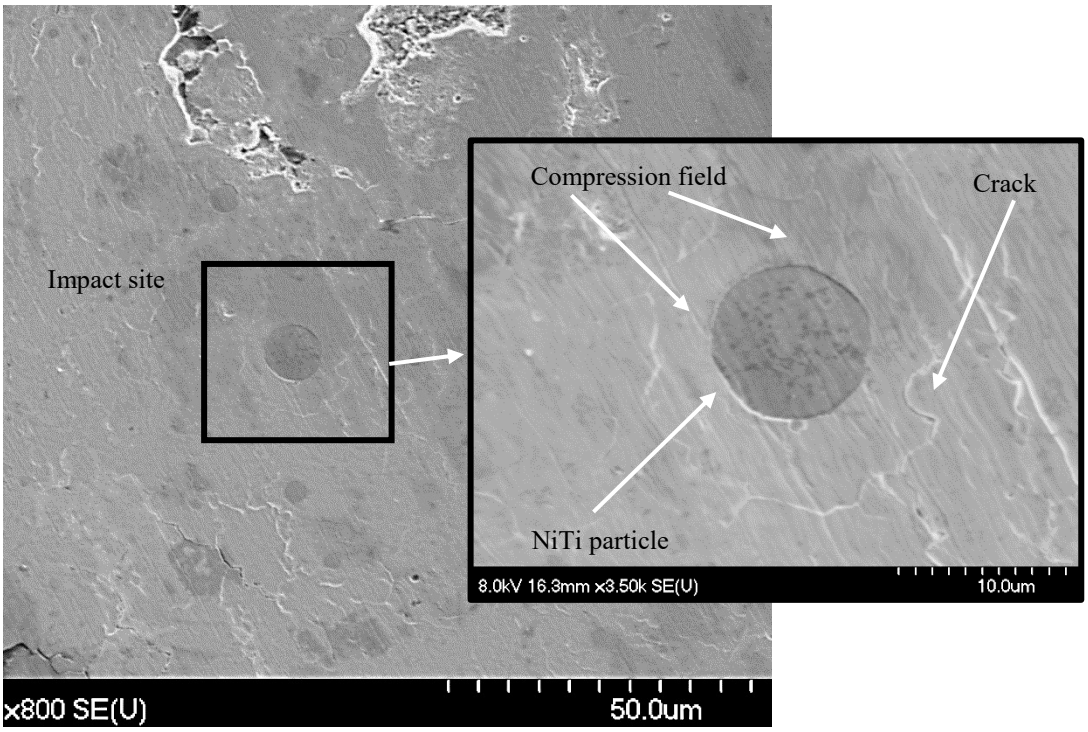

Figure 4-55 Closed crack network surrounding NiTi particle in 6.07 wt.% NiTi composite coating

All toughing mechanisms outlined above from superelastic NiTi have the ability to absorb crack propagation energy, diminishing the energy at the crack wake that normally would result in major cracking in the matrix. These mechanisms have been found to work simultaneously which amplifies the toughening effect further.

5 Conclusions and Recommendations

In the present work, electroless Ni-P coatings with 5.14 wt.%, 6.07 wt.%, and 7.02 wt.% nano-NiTi additions were successfully plated on API X100 pipe steel. The addition of these ductile reinforcements results in toughened coatings which hinder major crack propagation through the electroless Ni-P matrix. To characterize the coatings, the following tests were conducted:

1. Characterization of as deposited coating (XRD, SEM, EDS, profilometry)
2. Scratch testing under constant load single pass, constant load multi-pass, and increasing load conditions
3. Hertzian indentation testing under a varying amount of loads
4. Single particle impact at varying angles and velocities
5. Bend testing at 2.5 mm deflection

Characterization of these composite coatings showed presence of the austenitic superelastic phase, excellent bonding and uniform coating thickness. The addition of second phase particles resulted in an increase in surface roughness of the coatings. Therefore, a fine polish prior to use is necessary for these coatings in industrial applications to limit stress concentrations and in turn the initiation of cracks. Hardness, elastic modulus, and bend strength were all found to decrease with the addition of superelastic particles, therefore enhanced toughness of these coatings comes at the expense of strength and hardness.

It was found that scratch and indentation behaviour of the composite coatings are superior to that of the monolithic Ni-P coating due to increased cracking resistance. Addition of superelastic NiTi was found to decrease crack density and length, with pile-up observed adjacent to the wear track or indentation site, indicative of both ductile and brittle behaviour. Composite coatings showed higher material removal under larger loads and sliding distances as a result of lower hardness in comparison to the monolithic coatings. AE signals confirmed major cracking events within the monolithic coating (high noise signals) and micro-cracking events within the composite coatings (low noise signals).

Single particle erosion testing revealed evidence of a combination of both ductile and brittle erosion mechanisms with cracking and pile-up being present near the indent sites. Coatings containing 6.07 wt.% NiTi exhibited ductile behaviour in terms of material removal (highest at lower angle impacts) while the other coatings showed brittle behaviour with highest material removal at normal impact. Therefore, the optimal concentration for erosive conditions was the 6.07 wt.% NiTi coatings which showed enhanced toughness.

Bend test showed that the addition of superelastic NiTi delayed the onset of major cracking of the coatings in comparison to monolithic coating, however delamination occurred sooner due to the high stresses within the coating. This was confirmed with high noise AE signals and evidence in optical images. Therefore, for applications requiring similar conditions as were tested, concentration of NiTi should be kept low to prevent debonding of the coating.

Evidence of crack bridging, arresting, deflection, micro-cracking, and transformation toughening was observed in the coatings under the aforementioned testing conditions. As a result, these composite coatings successfully toughen the otherwise brittle Ni-P matrix, making them ideal for applications where high dent resistance is required.

It is recommended that the following work be done to further the understanding of the behaviour of these newly developed composite coatings:

1. Corrosion and erosion-corrosion resistance must be examined and compared to monolithic Ni-P coatings
2. Production of stand-alone coatings to determine coating properties without influence of a substrate
    a. Tensile testing of stand-alone coatings to determine mechanical properties
    b. Notched testing to determine fracture toughness
3. Annealing of composite coatings
    a. Examination of effect of annealing on residual stresses
    b. Effect of residual stress relaxation on hardness and wear resistance
    c. Precipitation of phases at various temperatures and the effect on coating properties

Publications produced from the present work include:

Accepted:

MacLean, M. et al., "Fabrication and investigation of scratch and indentation behaviour of new generation Ni-P-nano-NiTi composite coating for oil and gas pipelines," *Wear*, vol. 425-427, pp. 265-276, 2019.

Under Review:

MacLean, M. et al. "Erosion and toughening mechanisms of electroless Ni-P-nano-NiTi composite coatings on API X100 steel under single particle impact", *Tribology International*

Conference Presentation:

"Fabrication and investigation of scratch and indentation behaviour of new generation Ni-P-nano-NiTi composite coating for oil and gas pipelines", Poster Presentation, 22nd Wear of Materials Conference, Miami Florida, April 14-18, 2019

References

[1] I. Hutchings and P. Shipway, Tribology - Friction and Wear of Engineering Materials, Cambridge: Butterworth-Heinemann, 2017.

[2] C. Wang, *Indentation and Fracture Behaviour of Electroless Ni-P-based Composite Coatings,* Halifax: Dalhousie University, 2017.

[3] T. C. Bayram, N. Orbey, R. Y. Adhikari and M. Tuominen, "FP-based formulations as protective coatings in oil/gas pipelines," *Progress in Organic Coatings ,* vol. 88, pp. 54-63, 2015.

[4] O. Paul and A. M. Mohamed, "Erosion-corrosion in oil and gas industry: A review," *International Journal of Metallurgical & Materials Science and Engineering,* vol. 4, no. 3, pp. 7-28, 2014.

[5] Canadian Energy Pipeline Association, "Transmission Pipeline Industry Performance Reports," Canadian Energy Pipeline Association, Calgary, 2018.

[6] Canadian Energy Pipeline Association, "2017 Annual Transmission Pipeline Industry Performance Report," Canadian Energy Pipeline Association , 2017.

[7] I. Taubkin, A. V. Sukhov and T. Rudakova, "Analysis of the behaviour of a protective polymer coating for gas pipelines under the action of applied heat," *International Polymer Science and Technology,* vol. 32, no. 2, pp. 22-32, 2005.

[8] E. M. Fayyad, A. M. Abdullah, M. K. Hassan, A. M. Mohamed and G. Jarjoura, "Recent advances in electroless-plated Ni-P and its composites for erosion and corrosion applications: a review," *Emergent Materials,* vol. 24, no. 1-3, pp. 3-23, 2018.

[9] R. Taheri, *Evaluation of Electroless Nickel-Phosphorus (EN) Coatings,* Saskatoon, Saskatchewan, 2003.

[10] W. Wang, W. Zhang, Y. Wang, N. Mitsuzak and Z. Chen, "Ductile electroless Ni-P coating onto flexible printed circuit board," *Applied Surface Science,* vol. 367, pp. 528-532, 2016.

[11] D. C. Lagoudas, Ed., Shape Memory Alloys - Modeling and Engineering Applications, New York , New York : Springer, 2008.

[12] Products Finishing , "Electroless Nickel Plating," 2 18 2011. [Online]. Available: http://www.pfonline.com/articles/electroless-nickel-plating. [Accessed 09 06 2017].

[13] J. Lu and Y. Feng, "Measurement of orthophosphite concentration in electroless nickel plating baths by sodium ion electrodes," *Metal Finishing ,* vol. 107, no. 10, pp. 23-26, 2009.

[14] R. Taheri, I. Ogoucha and S. Yannacopoulos, "The tribological characteristics of electroless NiP coatings," *Wear,* vol. 249, pp. 389-396, 2001.

[15] B. Jiang, S. Jiang, A. Ma and Y. Zheng, "Effect of Heat Treatment on Erosion-Corrosion Behavior of Electroless Ni-P Coatings in Saline Water," *Materials and Manufacturing Processes,* vol. 29, pp. 74-82, 2014.

[16] J. Sudagar, J. Lian and W. Sha, "Electroless nickel, alloy, composite and nano coatings - A critical review," *Journal of Alloys and Compounds,* vol. 571, pp. 183-204, 2013.

[17] Techmetals Metal Finishing & Performance Coatings, *The Engineering Properties of Electroless Nickel Coatings,* 1980.

[18] N. Dadvand, *Investigation of the Corrosion Behavior of Electroless Nickel-Boron and Nickel-Phosphorous Coatings in Basic Solutions,* Halifax, 2002.

[19] O. Mendoza Gonzalez, *Preparation, characterization, surface chemistry and corrosion properties of Ni-TM-P alloys produced by autocatalytic reduction,* College Station, 1991.

[20] R. Parkinson, *Properties and applications of electroless nickel,* Nickel Development Institute .

[21] J. Ryhanen, *BIOCOMPATIBILITY EVALUATION OF NICKEL-TITANIUM SHAPE MEMORY METAL ALLOY,* Oulu, 1999.

[22] R. R. Adharapurapu, *Phase Transformations in Nickel-Rich Nickel-Titanium Alloys: Influence of Strain-Rate, Temperature, Thermomechanical Treatment and Nickel Composition on the Shape Memory and Superelastic Characteristics,* San Diego: University of California, 2007.

[23] H. Schuerch, *CERTAIN PHYSICAL PROPERTIES AND APPLICATIONS OF NITINOL,* Washington, 1968.

[24] K. Otsuka and C. Wayman, Shape Memory Materials, Cambridge : Cambridge University Press, 1998.

[25] D. Saletti, S. Pattofatto and H. Zhao, "Measurement of phase transformation properties under moderate impact tensile loading in a NiTi alloy," *Mechanics of Materials,* vol. 65, pp. 1-11, 2013.

[26] J. Hashemi and W. F. Smith, Foundations of Materials Science and Engineering, New York : McGraw-Hill, 2006.

[27] R. Neupane, *Indentation and Wear Behavior of Superelastic TiNi Shape Memory Alloy,* Halifax, 2014.

[28] C.-W. Chan, "A study on the corrosion fatigue behaviour of laser-welded shape memory NiTi wires in a simulated body fluid," *Surface and Coatings Technology,* vol. 320, pp. 574-578, 2017.

[29] C. Dellacorte, "Launch Load Resistant Spacecraft Mechanisms Bearings Made From NiTi Superelastic Intermetallic Materials," in *42nd Aerospace Mechanisms Symposium*, Baltimore, 2014.

[30] C. Shen, Z. Wu, Z. Gao, X. Ma, S. Qiu and Y. S. T. Liu, "Impact protection behavior of NiTi shape memory alloy wires," *Materials Science and Engineering: A,* vol. 700, pp. 132-139, 2017.

[31] K. C. Chen, "NiTi - Magic or Phase Transformations?," in *American Society for Engineering Education Annual Conference & Exposition*, 2003.

[32] R. Richman, A. Rao and D. Kung, "Cavitation erosion of NiTi explosively welded to steel," *Wear,* pp. 80-85, 1995.

[33] K. Ashbee, M. Bassett and A. Jardine, "Effects of cooling rate on the shape memory effect thermodynamics of NiTi," *Journal of Materials Science,* vol. 23, pp. 4273-4281, 1988.

[34] T. Inamura, M. Mitsuhara, S. Motomura, M. Nishida and Y. Soejima, "In situ scanning electron microscopy study of the thermoelastic martensitic transformation in Ti-Ni shape memory alloy," *Acta Materialia,* vol. 103, pp. 352-360, 2016.

[35] D. Li, "Development of novel tribo composites with TiNi shape memory alloy matrix," *Wear,* vol. 255, pp. 617-628, 2003.

[36] G. Ates and M. Kok, "The effect of addition of various elements on properties of NiTi-based shape memory alloys for biomedical applications," *The European Physical Journal Plus,* vol. 132, no. 185, p. 6, 2017.

[37] L. Ploof, "Electroless Nickel Composite Coatings," *Advanced Materials and Processes,* p. Oriskany , 2008.

[38] J. Balaraju, T. Sankara Narayanan and S. Seshadri, "Electroless Ni-P composite coatings," *Journal of Applied Electrochemistry,* vol. 33, pp. 807-816, 2003.

[39] M. Islam, M. R. Azhar, N. Fredj, T. D. Burleigh, O. R. Oloyede, A. A. Almajid and I. S. Shah, "Influence of SiO2 nanoparticles on hardness and corrosion resistance of electroless Ni-P coatings," *Surface & Coatings Technology,* vol. 261, pp. 141-148, 2015.

[40] J.-P. Celis and S. K. Ghosh, "Plating of Nano-composites - Overview and Trends," in *High Performance Coatings for Automotive and Aerospace Industries*, New York, Nova Science Publishers, Inc. , 2010, pp. 227-299.

[41] A. Afshar and S. Sadreddini, "Corrosion resistance enhancement of Ni-P-nano SiO2 composite coatings on aluminum," *Applied Surface Science,* vol. 303, pp. 125-130, 2014.

[42] G. Deniz, S. Sen and U. Sen, "Structural Characterization of Titanium Nitride Coatings on AISI M2 Steel," in *Nitrides and Oxynitrides III : Proceedings of the 5th International Symposium on Nitrides*, Eskisehir, Trans Tech Publications , 2007, pp. 219-224.

[43] I. R. Mafi and C. Dehghanian, "Studying the effects of the addition of TiN nanoparticles to Ni-P electroless coatings," *Applied Surface Science,* vol. 258, pp. 1876-1880, 2011.

[44] W. Huang, L. Yu and X. Zhao, "Preparation and characterization of Ni-P-nanoTiN electroless composite coatings," *Journal of Alloys and Compounds,* vol. 509, no. 10, pp. 4154-4159, 2011.

[45] H. Luo, M. Leitch, Y. Behnamian, Y. Ma, H. Zeng and J.-L. Luo, "Development of electroless Ni-P/nano-WC composite coatings and investigation on its properties," *Surface & Coatings Technology,* vol. 277, pp. 99-106, 2015.

[46] A. A. Aal, S. E. Badry and Z. A. Hamid, "Electroless deposition and characterization of Ni-P-WC composite alloys," *Surface & Coatings Technology,* vol. 201, pp. 5948-5953, 2007.

[47] S. Afroukhteh, C. Dehghanian and M. Emamy, "Preparation of the Ni-P composite coating co-deposited by nano TiC particles and evaluation of it's corrosion property," *Applied Surface Science,* vol. 258, pp. 2597-2601, 2012.

[48] C.-S. Chang, K.-H. Hou, M.-D. Ger, C.-K. Chung and J.-F. Lin, "Effects of annealing temperature on microstructure, surface roughness, mechanical and tribological properties of Ni-P and Ni-P/SiC films," *Surface & Coatings Technology,* vol. 288, pp. 135-143, 2016.

[49] I. Apachitei, J. Duszczyk, L. Katgerman and P. Overkamp, "Electroless Ni-P composite coatings: the effect of heat treatment on the microhardness of substrate and coating," *Scripta Materialia,* vol. 38, pp. 1347-1353, 1998.

[50] D. Colombo, A. Molinari and G. Straffelini, "Surface durability of electroless Ni-P composite deposits," *Wear,* vol. 236, no. 1-2, pp. 179-188, 1999.

[51] Z. Karaguiozova, "Electroless nickel composite coatings with nanodiamond additives," 2014.

[52] K. Azari-Dorcheh, M. Ebrahimian-Hosseinabadi and S. Vaghefi Moonir, "Wear behavior of electroless Ni-P-B4C Composite Coatings," *Wear,* vol. 260, pp. 123-127, 2006.

[53] A. C. Fischer-Cripps, Introduction to Contact Mechanics, New York : Springer , 2007.

[54] K. Breder and D. Louapre, "Hertzian Indentation Stress Field Equations," *Int. J. Appl. Ceram. Technol.,* vol. 12, no. 5 , pp. 1071-1079, 2015.

[55] T. O'Brien and I. Raju, "Fracture mechanics concepts, stress fields, strain energy release rates, delamination initiation and growth criteria," in *Delamination*

behaviour of composites, Cambridge, Woodhead Publishing and Maney Publishing, 2008, pp. 3-27.

[56] P. Kumar, Elements of Fracture Mechanics, India: McGraw Hill Education (India) Private Limited, 2009.

[57] A. Almotairi, *Mechanical and Thermal Damage of Hard Chromium Coatings on 416 Stainless Steel,* Halifax, 2016.

[58] R. F. Cook and G. M. Pharr, *Direct Observation and Analysis of Indentation Cracking in Glasses and Ceramics,* vol. 73, A.H.Heuer, Ed., American Ceramic Society, 1990, pp. 787-817.

[59] J. Chen, "Indentation-based methods to assess fracture toughness for thin coatings," *J.Phys. D: Appl. Phys,* vol. 45, p. 14, 2012.

[60] A. C. Fischer-Cripps, Introduction to Contact Mechanics, Springer, 2007.

[61] R. C. Yu, "Modeling of delamination fracture in composites: a review," in *Delamination behaviour of composites*, Cambridge, Woodhead Publishing and Maney Publishing, 2008, pp. 429-457.

[62] K. G. Budinski, Friction, Wear and Erosion Atlas, Boca Raton: CRS Press, 2014.

[63] G. W. Stachowiak and A. W. Batchelor, Engineering Tribology, Oxford: Elsevier Inc., 2014.

[64] M. A. Islam and Z. N. Farhat, "Effect of impact angle and velocity on erosion of API X42 pipeline steel under high abrasive feed rate," *Wear,* vol. 311, pp. 180-190, 2014.

[65] M. Naveed, H. Schlag, F. Konig and W. Sabine, "Influence of the Erodent Shape on the Erosion Behavior of Ductile and Brittle Materials," *Tribology Letters,* vol. 65, no. 18, pp. 1-9, 2017.

[66] E. Bousser, L. Martinu and J. E. Klemberg-Sapieha, "Effect of erodent properties on the solid particle erosion mechanisms of brittle materials," *Journal of Materials Science,* vol. 48, no. 16, pp. 5543-5558, 2013.

[67] S. A. Alidokht, P. Vo, S. Yue and R. R. Chromik, "Erosive wear behavior of Cold-Sprayed Ni-WC composite coating," *Wear,* Vols. 376-377, pp. 566-577, 2017.

[68] G. Sundararajan, *The Nature of Plastic Deformation During Single Impact and Its Relevance To Solid Particle Erosion,* Columbus: The Ohio State University , 1981.

[69] A. Cenna, N. Page, E. Kisi and M. Jones, "Single particle impact tests using gan gun and analysis of high strain-rate impact events in ductile materials," *Wear,* vol. 271, no. 9-10, pp. 1497-1503, 2011.

[70] G. Y. Lee, C. Dharan and R. Ritchie, "A physically-based abrasive wear model for composite materials," *Wear,* vol. 252, pp. 322-331, 2002.

[71] Y. Shen and N. Chawla, "On the correlation between hardness and tensile strength in particle reinforced metal matrix composites," *Materials Science and Engineering,* vol. A297, pp. 44-47, 2001.

[72] M. Taya, S. Hayashi, A. Kobayashi and H. Yoon, "Toughening of a Particulate-Reinforced/Ceramic-Matrix Composite," Office of Naval Research, Washington, 1989.

[73] L. S. Sigl, "Microcrack toughening in brittle materials containing weak and strong interfaces," *Acta mater.,* vol. 44, no. 9, pp. 3599-3609, 1996.

[74] X. Sun and J. Yeomans, "Ductile Phase Toughned Brittle Materials," *Journal of Materials Science & Technology,* vol. 12, no. 2, pp. 124-134, 1996.

[75] M. Song, S. He, K. Du, Z. Huang, T. Yao, Y. Hao, S. Li, R. Yang and H. Ye, "Transformation induced crack deflection in a metastable titanium alloy and

implications on transformation toughening," *Acta Materialia,* vol. 118, pp. 120-128, 2016.

[76] D. Alman and J. Hawk, "Abrasive wear behavior of a brittle matrix (MoSi2) composite reinforced with a ductile phase (Nb)," *Wear,* vol. 251, no. 1-12, pp. 890-900, 2001.

[77] W. Hillig, O. Raddatz, A. Schneider and N. Claussen, "Analysis and model of the crack bridging mechanisms in a ductile fiber reinforced ceramic matrix composite," *Journal of Materials Science,* vol. 36, no. 7, pp. 1653-1663, 2001.

[78] J. S.-C. Jang and C.-T. Liu, "Structural and mechanical characterizations of ductile Fe particles-reinforced Mg-based bulk metallic glass composites," *Journal of Alloys and Compounds,* vol. 485, no. 1-2, pp. 290-294, 2009.

[79] K. T. Faber, T. Iwagoshi and A. Ghosh, "Toughening by Stress-Induced Microcracking in Two-Phase Ceramics," *Communications of the American Ceramic Society,* vol. 71, no. 9, pp. C399-C401, 1988.

[80] J. P. Singh, D. Hasselman, W. Su, J. Rubin and R. Palicka, "Observations on the nature of micro-cracking in brittle composites," *Journal of Materials Science,* vol. 16, no. 1, pp. 141-150, 1981.

[81] S. Warrier, M. B.S. and D. Miracle, "Interface effects on crack deflection and bridging during fatigue crack growth of titanium matrix composites," *Acta Materialia,* vol. 45, no. 12, pp. 4969-4980, 1997.

[82] P. J. Withers, P. Lopez-Crepso, A. Kyrieleis and Y.-C. Hung, "Evolution of crack-bridging and crack-tip driving force during the growth of a fatigue crack in Ti/SiC composite," *Proceedings: Mathematical, Physical and Engineering Sciences,* vol. 468, no. 2145, pp. 2722-2743, 2012.

[83] G. Bao and F. Zok, "ON THE STRENGTH OF DUCTILE PARTICLE REINFORCED BRITTLE MATRIX COMPOSITES," *Acta metallurgica et materialia,* vol. 41, no. 12, pp. 3515-3524, 1993.

[84] M. Jin and S. Chen, "Mode-I Crack Control by SMA Fiber with a Special Configuration," in *Damage and Fracture of Composite Materials and Structures*, Berlin, Springer, 2012, pp. 5-16.

[85] R. Ritchie, "Mechanisms of Fatigue Crack Propagation in Metals, Ceramics and Composites: Role of Crack Tip Shielding," *MAterials Science and Engineering ,* vol. 103, pp. 15-28, 1988.

[86] M. Barchiesi, "Toughening by Crack Deflection in the Homogenization of Brittle Composites with Soft Inclusions," *Arch. Rational Mech. Anal,* vol. 227, pp. 749-766, 2018.

[87] E. Martin, P. Peters, D. Leguillon and J. Quenisset, "Conditions for matrix crack deflection at an interface in ceramic matrix composites," *Materials Science and Engineering: A,* vol. 250, no. 2, pp. 291-302, 1998.

[88] L. Ma, "Fundamental formulation for transformation toughening," *International Journal of Solids and Structures,* vol. 47, pp. 3214-3220, 2010.

[89] C. Wang, Z. Farhat, G. Jarjoura, M. K. Hassan and A. M. Abdullah, "Indentation and bending behavior of electroless Ni-P-Ti composite on pipeline steel," *Surface & Coatings Technology,* vol. 334, pp. 243-252, 2018.

[90] ASM International, ASM Handbook Volume 18 Friction, Lubrication, and Wear Technology, USA: ASM International, 1992.

[91] C. Wang, Z. Farhat, G. Jarjoura and M. K. Hassan, "Indentation and bending behavior of electroless Ni-P-Ti composite coatings on pipeline steel," *Surface & Coatings Technology ,* vol. 334, pp. 243-252, 2018.

[92] S. Ranganatha, T. Venkatesha and K. Vathsala, "Development of high performance electroless Ni-P-HNT composite coatings," *Applied Surface Science,* vol. 263, pp. 149-156, 2012.

[93] H.-L. Wang, L.-Y. Liu, D. Yong, W.-Z. Zhang and W.-F. Jiang, "Preparation and corrosion resistance of electroless Ni-P/SiC funtionally gradient coatings on AZ91D magnesium alloy," *Applied Surface Science,* vol. 286, pp. 319-327, 2013.

[94] J. Sudagar, J. Lian and W. Sha, "Electroless nickel, alloy, composite and nano coatings - A critical review," *Journal of Alloys and Compounds,* vol. 571, pp. 183-204, 2013.

[95] F. E.-T. Heakal and M. A. Maanoum, "Role of Some Plating Parameters in the Properties of Ni-P/Al2O3 Nanocomposite Coatings on Mg alloy," *International Journal of Electrochemical Science,* vol. 11, pp. 7198-7215, 2016.

[96] J. N. Balaraju, T. S. Narayanan and S. Seshadri, "Electroless Ni-P composite coatings," *Journal of Applied Electrochemistry ,* vol. 33, pp. 807-816, 2003.

[97] S. Karthikeyan and B. Ramamoorthy, "Effect of reducing agent and nano Al2O3 particles on the properties of electroless Ni-P coating," *Applied Surface Science,* vol. 307, pp. 654-660, 2014.

[98] P. Sahoo and S. K. Das, "Tribology of electroless nickel coatings- A review," *Materials and Design,* vol. 32, pp. 1760-1775, 2011.

[99] M. Islam, M. R. Azhar, N. Fredj and T. D. Burleigh, "Electrochemical impedance spectroscopy and indentation studies of pure and composite electroless Ni-P coatings," *Surface & Coatings Technology,* vol. 236, pp. 262-268, 2013.

[100] E. Georgiza, J. Novakovic and P. Vassiliou, "Characterization and corrosion resistance of duplex electroless Ni-P composite coatings on magnesium alloy," *Surface & Coatings Technology,* vol. 232, pp. 432-439, 2013.

[101] S. Afroukhteh, C. Dehghanian and M. Emamy, "Preparation of the Ni-P composite coating co-deposited by nano TiC particles and evaluation of it's corrosion property," *Applied Surface Science,* vol. 258, pp. 2597-2601, 2012.

[102] C. Wang, Z. Farhat, G. Jarjoura, M. K. Hassan and A. M. Abdullah, "Indentation and erosion behaviour of electroless Ni-P coating on pipeline steel," *Wear,* Vols. 376-377, pp. 1630-1639, 2017.

[103] I. Sivandipoor and F. Ashrafizadeh, "Synthesis and tribological behaviour of electroless Ni-P-WS2 composite coatings," *Applied Surface Science,* vol. 263, pp. 314-319, 2012.

[104] M. Czagany, P. Baumli and G. Kaptay, "The influence of the phosphorous content and heat treatment on the nano-micro-structure, thickness and micro-hardness of electroless Ni-P coatings on steel," *Applied Surface Science,* vol. 423, pp. 160-169, 2017.

[105] R. Neupane, *Indentation and Wear Behavior of Superelastic TiNi Shape Memory Alloy,* Halifax : Dalhousie University, 2014.

[106] Z. Farhat and C. Zhang, "On the Deformation of Superelastic TiNi Alloy," *Tribology Letters,* vol. 37, pp. 169-173, 2010.

[107] D.-H. Lee, B. Park, A. Saxena and T. P. Serene, "Enhanced Surface Hardness by Boron Implantation in Nitinol Alloy," *Journal of Endodontics,* vol. 22, no. 10, pp. 543-546, 1996.

[108] M. Sribalaji, O. A. Rahman, T. Laha and A. K. Keshri, "Nanoindentation and nanoscratch behavior of electroless deposited nickel-phosphorous coating," *Materials Chemistry and Physics ,* vol. 177, pp. 220-228, 2016.

[109] P. Sittner, L. Heller, J. Pilch, C. Curfs, T. Alonso and D. Favier, "Young's Modulus of Austenite and Martensite Phases in Superelastic NiTi Wires," *Journal of Materials Engineering and Performance,* vol. 23, no. 7, pp. 2303-2314, 2014.

[110] J. Chen, "Indentation-based methods to assess fracture toughness for thin coatings," *Journal of Physics D: Applied Physics,* vol. 45, pp. 1-14, 2012.

[111] Q. Zhou, J. He, X. Hao, W. Chu and L. Qiao, "The effect of hydrogen on plastic deformation of electroless nickel phosphorous amorphous coating," *Materials Science and Engineering A,* vol. 437, pp. 356-359, 2006.

[112] D. Lopez, J. Congote, J. Cano, A. Toro and T. A.P., "Effect of particle velocity and impact angle on the corrosion-erosion of AISI 304 and AISI 420 stainless steels," *Wear,* vol. 259, no. 1-6, pp. 118-124, 2005.

[113] Y. Oka, S. Mihara and T. Yoshida, "Impact-angle dependence and estimation of erosion damage to ceramic materials caused by solid particle impact," *Wear,* vol. 267, no. 1-4, pp. 129-135, 2009.

[114] E. Bousser, L. Martinu and J. Klemberg-Sapieha, "Solid particle erosion mechanisms of protective coatings for aerospace applications," *Surface & Coatings Technology,* vol. 257, pp. 165-181, 2014.

[115] M. Lindroos, M. Apostol, V.-T. Kuokkala, A. Laukkanen, K. VAltonen, K. Holmberg and O. Oja, "Experimental study on the behavior of wear resistant steels under high velocity single particle impacts," *International Journal of Impact Engineering,* vol. 78, pp. 114-127, 2015.

[116] B. Lawn, "Indentation of ceramics with spheres: a century after hertz," *J.Am.Ceram. Soc.,* vol. 81, no. 8, pp. 1977-1994, 1998.

[117] K. Johnson, Contact Mechanics, Cambridge, U.K.: Camrbidge University Press, 1985.

[118] J. Lackner, "Tribology and micromechanics of chromium nitride based multilayer coatings on soft and hard substrates," *Coatings,* vol. 4, no. 1, pp. 121-138, 2014.

[119] C. Hardy, C. Baronet and G. Tordion, "The elasto-plastic indentation of a half-space by a rigid spehre," *Int. J. Numer. Methods Eng.,* vol. 3, no. 4, pp. 451-462, 1971.

[120] A. Yonezu, M. Niwa, J. Ye and X. Chen, "Contact fracture mechanisms of electroplated Ni-P coating upon stainless steel substrate," *Materials Science & Engineering A,* vol. 563, pp. 184-192, 2013.

[121] M. Roy, Thermal sprayed coatings and their tribological performances, Hershey: IGI Global, 2015.

[122] W. Y. Li, J. Wang, H. Zhu, H. Li and C. Huang, "On ultra high velocity micro-particle impact on steels- A single impact study," *Wear,* vol. 305, pp. 216-227, 2013.

[123] D. Al-Anazi, M. Hasmi and B. Yilbas, "Three-point bend testing of HVOF AMDRY 9954 coating on Ti-6Al-4V alloy," *Journal of Materials Processing Technology,* vol. 174, no. 1-3, pp. 204-210, 2006.

[124] G. Dayananda and M. S. Rao, "Effect of strain rate on properties of superelastic NiTi thin wires," *Materials Science and Engineering: A,* vol. 486, no. 1-2, pp. 96-103, 2008.

[125] Z. Yin, C. Huang, B. Zou, H. Liu, H. Zhu and J. Wang, "Study of the mechanical properties, strengthening and toughening mechanisms of Al2O3/ TiC micro-nano-composite ceramic tool material," *Materials Science and Engineering: A,* vol. 577, pp. 9-15, 2013.

[126] H. Tan and W. Yang, "Toughening mechanisms of nano-composite ceramics," *Mechanics of Materials,* vol. 30, no. 2, pp. 111-123, 1998.

[127] D. Vashishth, K. Tanner and W. Bonfield, "Experimental validation of a microcracking-based toughening mechanism for cortical bone," *Journal of Biomechanics,* vol. 36, no. 1, pp. 121-124, 2003.

[128] B. Zhu, X. Xue, H. Kou, X. Li and J. Li, "Effect of microstructure on the fracture toughness of multi-phase high Nb-containing TiAl alloy," *Intermetallics,* vol. 100, pp. 142-150, 2018.

[129] Z. Farhat, G. Jarjoura and M. Shahirnia, "Dent Resistance and Effect of Indentation Loading Rate on Superelastic TiNi Alloy," *Metallurgical and Materials Transactions A,* vol. 44A, no. 8, pp. 3544-3551, 2013.

[130] C. Lin, N. Dadvand, Z. Farhat and G. J. Kipouros, "Electroless nickel phosphorous plating on carbon steel," in *Materials Science and Technology*, Montreal, 2013.

[131] C. A. Klein and G. F. Cardinale, "Young's modulus and Poisson's ratio of CVD diamond," *Diamond and Related Materials,* vol. 2, no. 5-7, pp. 918-923, 1993.

[132] J. Hou, Q. Li, J. Lv and H. Zuo, "Crack deflection by the transformable particles dispersed in composites," *Acta Mech,* vol. 227, no. 3, pp. 743-756, 2016.

[133] M. Song, S. He, K. Du, Z. Huang, T. Yao, Y. Hao, S. Li, R. Yang and H. Ye, "Transformation induced crack deflection in a metastable titanium alloy and implications on transformation toughening," *Acta Materialia,* vol. 118, pp. 120-128, 2016.

[134] R. H. Hannink, P. M. Kelly and B. C. Muddle, "Transformation Toughening in Zirconia-Containing Ceramics," *J. Am. Ceram. Soc.,* vol. 83, no. 3, pp. 461-487, 2000.

[135] R. A. Flinn and P. K. Trojan, Engineering Materials and Their Applications, Boston : Houghton Mifflin Company, 1990.

[136] J. von Appen, F. Bachhuber, R. Dronskowski, T. Nilges, A. Pfitzner, P. Schmidt and R. Weihrich, "The Extended Stability Range of Phosphorous Allotropes," *Angew. Chem. Int. Ed.,* vol. 53, pp. 11629-11633, 2014.

[137] P. Sittner, L. Heller, J. Pilch and C. Curfs, "Young's modulus of austenite and martensite phases in superelastic niti wires," *Journal of materials engineering and performance,* vol. 23, no. 7, pp. 2303-2314, 2014.

[138] M. Naveed, H. Schlag, F. Konig and S. Weib, "Influence of the Erodent Shape on the Erosion Behavior of Ductile and Brittle Materials," *Tribology Letters,* vol. 65, no. 18, pp. 1-9, 2017.

[139] A. Steel, *316/316L Stainless Steel Product Data Sheet,* West Chester, 2007.

[140] E. Abel, Y. Liu and Q. Zhao, "Surface free energies of electroless Ni-P based composite coatings," *Applied Surface Science,* vol. 240, pp. 441-451, 2005.

[141] J. Pelleg, Mechanical Properties of Materials, Springer Dordrecht Heidelberg New York London, 2013.

[142] C.-S. Kim, K. Cho, M. Manjili and M. Nezafati, "Mechanical performance of particulate-reinforced Al metal-matrix composites (MMCs) and Al metal-matrix nano-composites (MMNCs)," *J Mater Sci,* vol. 52, pp. 13319-13349, 2017.

[143] M. Franco, W. Shaw and H. Liu, "Micro-scale wear characteristics of electroless Ni-P/SiC composite coating under two different sliding conditions," *Wear,* vol. 317, pp. 254-264, 2014.

[144] L. Yu, W. Huang and X. Zhao, "Preparation and characterization of Ni-P-nanoTiN electroless composite coatings," *Journal of Alloys and Compounds,* vol. 509, no. 10, pp. 4154-4159, 2011.

[145] A. Rouzaud, E. Barbier, J. Ernoult and E. Quesnel, "A method for elastic modulus measurements of magnetron sputtered thin films dedicated to mechanical applications," *Thin Solid Films,* vol. 270, pp. 270-274, 1995.

[146] M. MacLean, Z. Farhat, G. Jarjoura, E. Fayyad, A. Abdullah and M. Hassan, "Fabrication and investigation of the scratch and indentation behaviour of new

generation Ni-P-nano-NiTi composite coating for oil and gas pipelines," *Wear,* Accepted in Print, 2019 .

[147] B. Syed, S. M. Shariff, G. Padmanabham, S. Lenka, B. Bhattacharya and S. Kundu, "Influence of laser surface hardened layer on mechanical properties of re-engineered low carbon steel sheet," *Materials Science and Engineering A,* vol. 685, pp. 168-177, 2017.

[148] H.-J. Kim and Y. Kweon, "Elastic modulus of plasma-sprayed coatings determined by indentation and bend tests," *Thin Solid Films,* vol. 342, no. 1-2, pp. 201-206, 1999.

[149] N. Bosh, L. Deggelmann, C. Blattert, H. Mozaffari and C. Muller, "Synthesis and characterization of Halar polymer coating deposited on titanium substrate by electrophoretic deposition process," *Surface and Coatings Technology,* vol. 347, pp. 369-378, 2018.

[150] J. Miguel, J. Guilemany, B. Mellor and Y. Xu, "Acoustic emission study on WC-Co thermal sprayed coatings," *Materials Science and Engineering A,* vol. 352, pp. 55-63, 2003.

[151] R. Taheri, I. Oguocha and S. Yannacopoulos, "Effect of coating parameters and heat treatment on the adhesive properties of electroless Ni-P coatings," *Canadian Metallurgical Quarterly,* vol. 43, no. 3, pp. 363-369, 2004.

[152] Y. Xu and B. Mellor, "Application of acoustic emission to detect damage mechanisms of particulate filled thermoset polymeric coatings in four pointb end tests," *Surface and Coatings Technology,* vol. 205, no. 23-24, pp. 5478-5482, 2011.

Appendix A – Scratch Behaviour

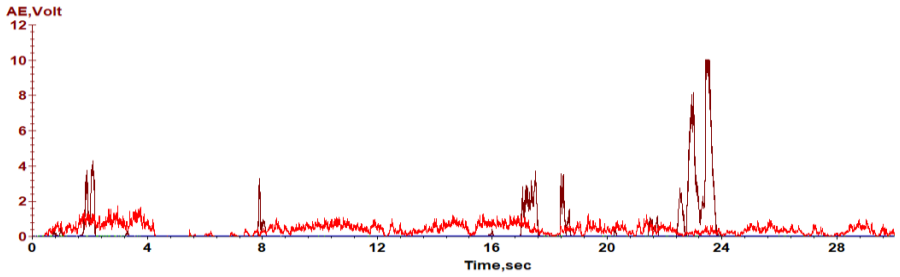

Figure 0-1 Acoustic emission signals under 0.5 kg constant load for Ni-P, 5.14 wt.% NiTi, 6.07 wt.% NiTi, and 7.02 wt.% NiTi coatings

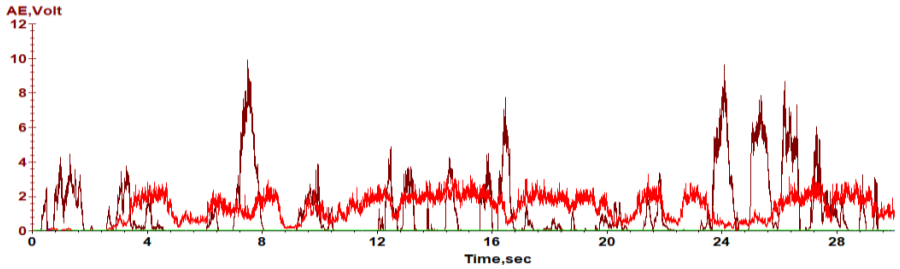

Figure 0-2 Acoustic emission signals under 2 kg constant load for Ni-P, 5.14 wt.% NiTi, 6.07 wt.% NiTi, and 7.02 wt.% NiTi coatings

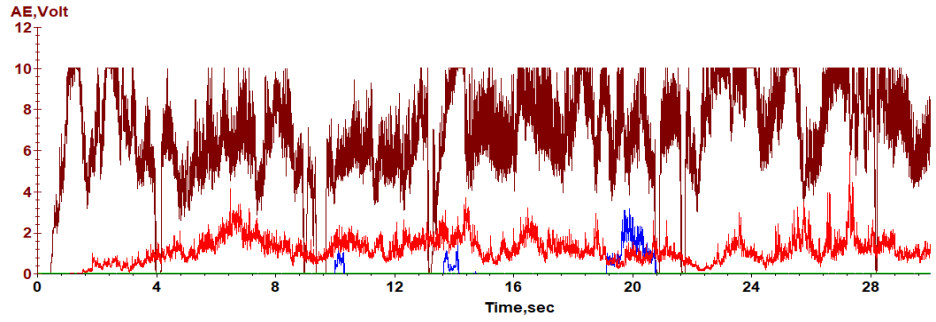

Figure 0-3 Acoustic emission signals under 4 kg constant load for Ni-P, 5.14 wt.% NiTi, 6.07 wt.% NiTi, and 7.02 wt.% NiTi coatings

Appendix B– Indentation Behaviour

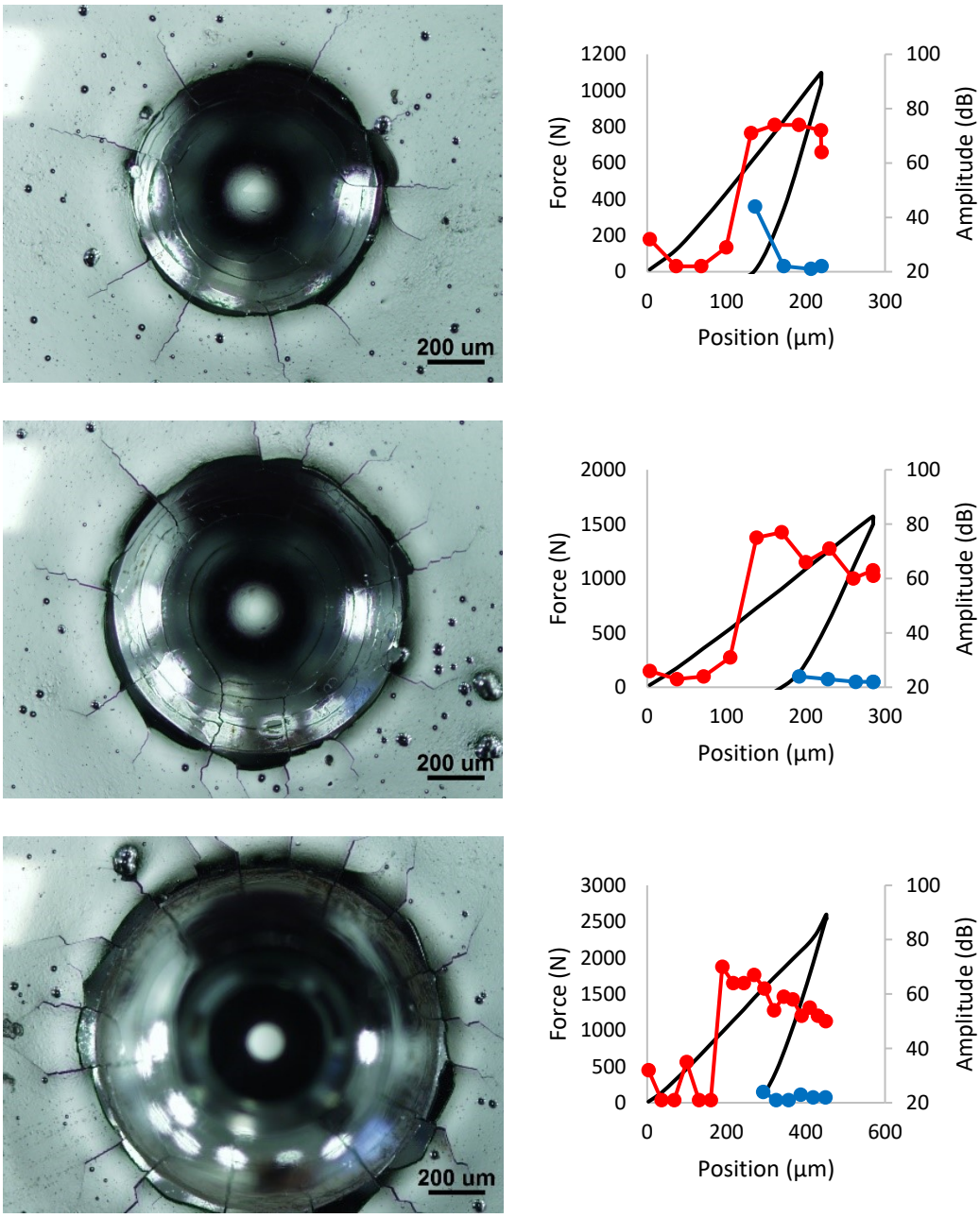

Figure 0-4 Indentation surfaces and load-depth-AE curves under 1000 N (top), 1500 N (middle) and 2500 N (bottom) for monolithic Ni-P coating

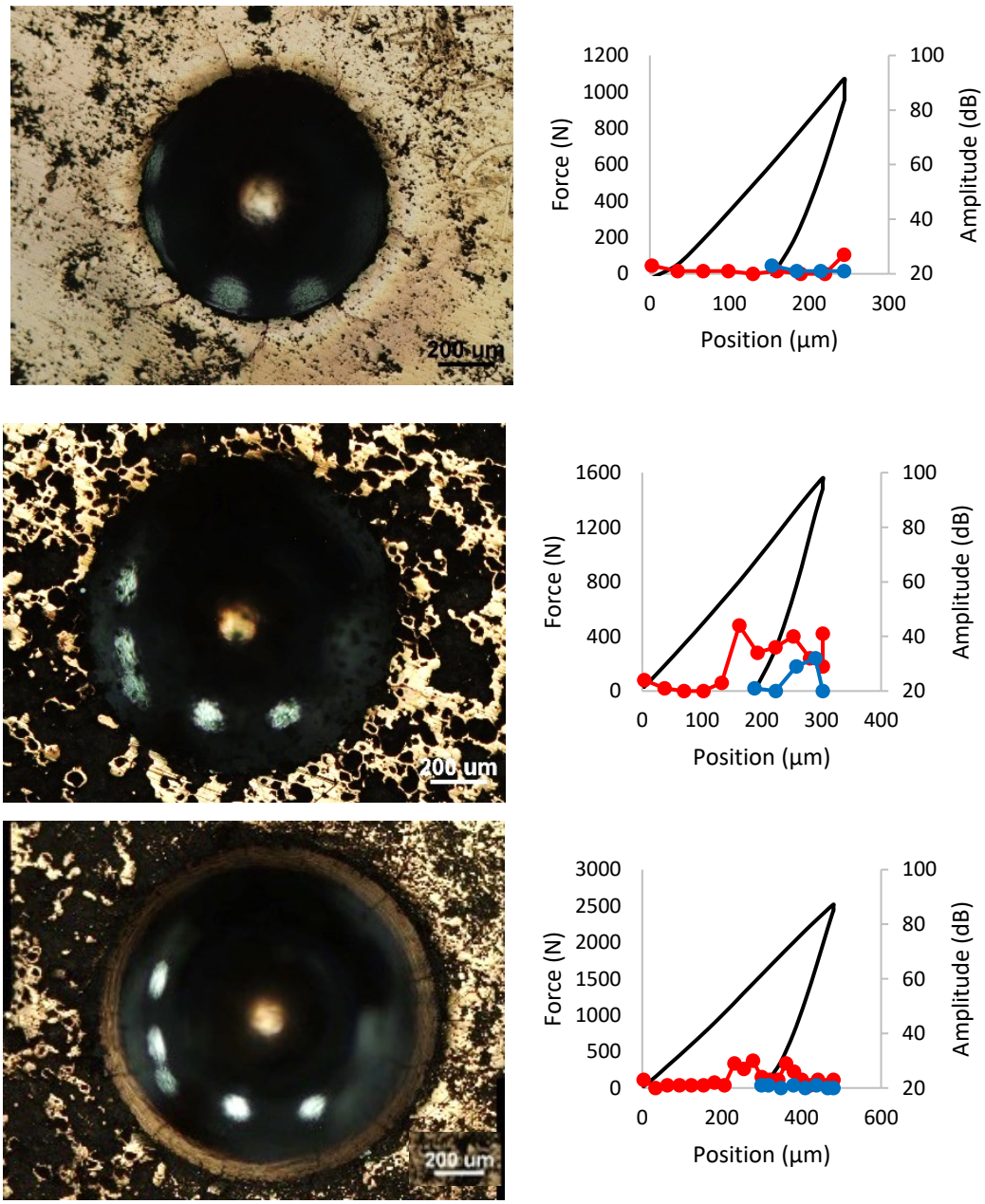

Figure 0-5 Indentation surfaces and load-depth-AE curves under 1000 N (top), 1500 N (middle) and 2500 N (bottom) for 5.14 wt.% NiTi coating

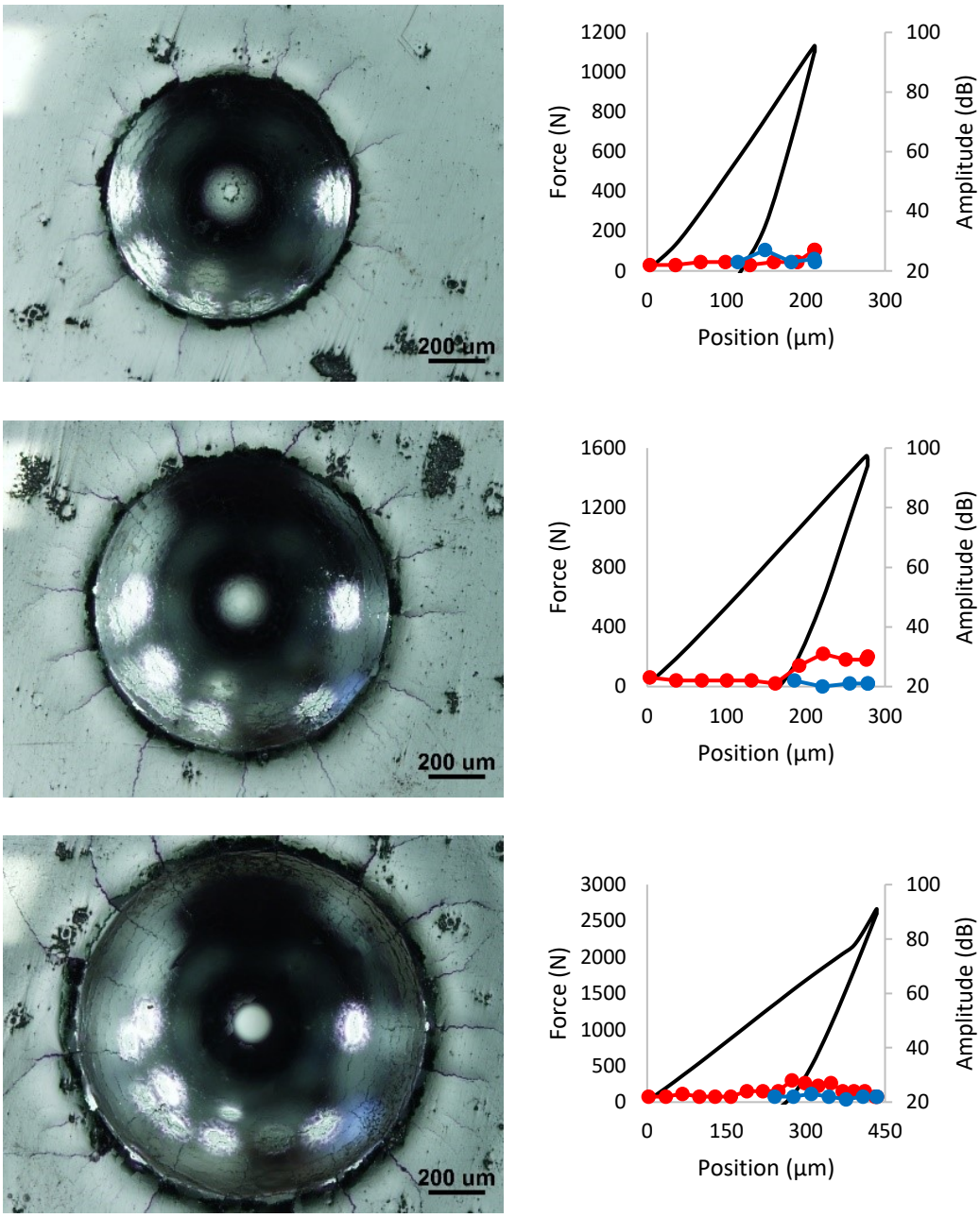

Figure 0-6 Indentation surfaces and load-depth-AE curves under 1000 N (top), 1500 N (middle) and 2500 N (bottom) for 6.07 wt.% NiTi coating

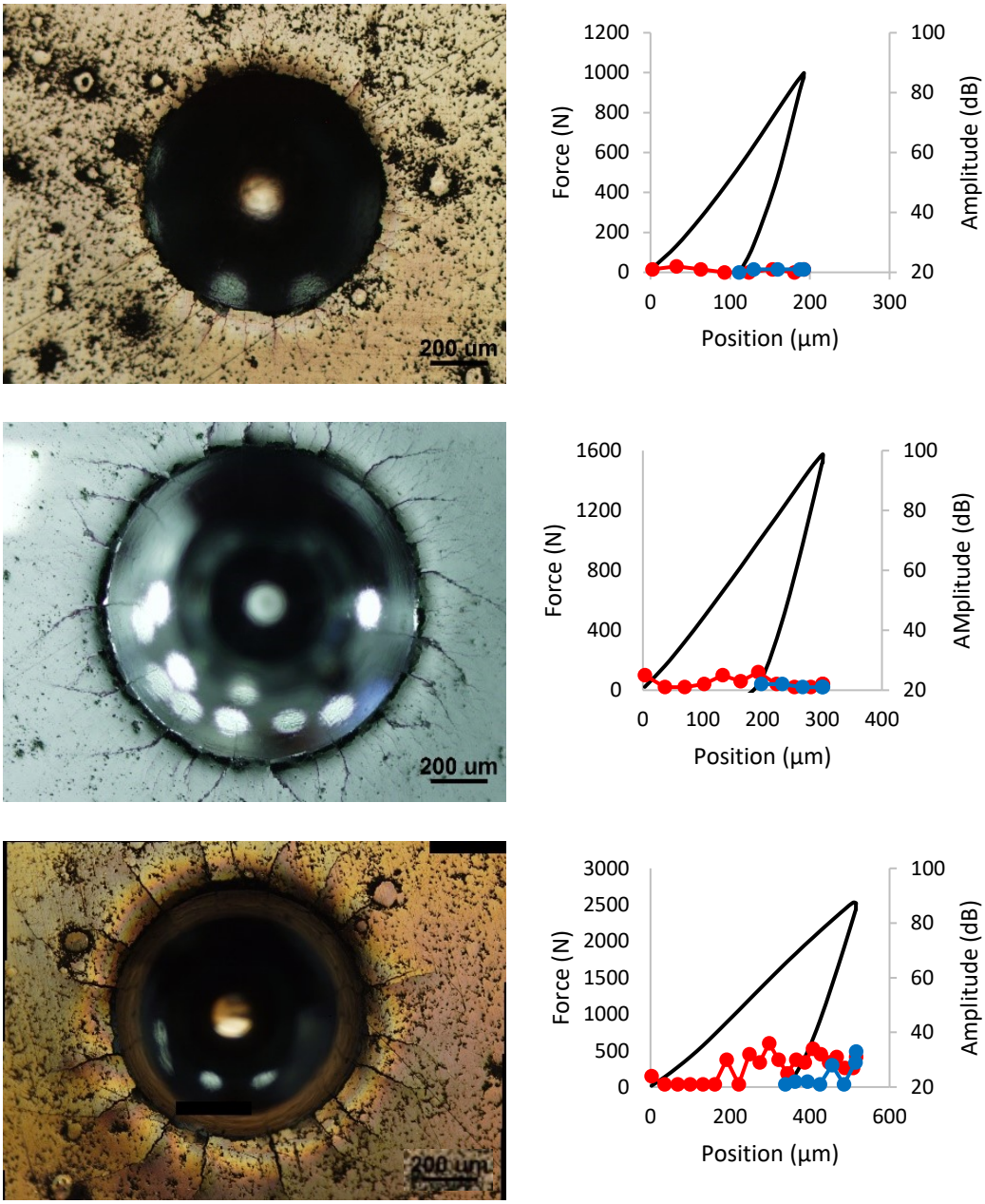

Figure 0-7 Indentation surfaces and load-depth-AE curves under 1000 N (top), 1500 N (middle) and 2500 N (bottom) for 7.02 wt.% NiTi coating

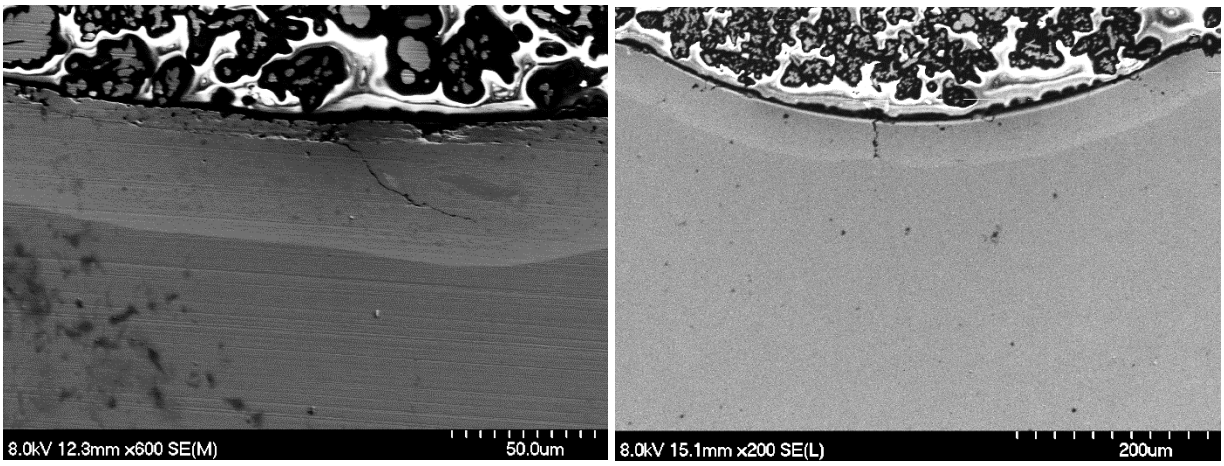

Figure 0-8 Indentation cross-sections of 6.07 wt.% NiTi (left) and 7.02 wt.% NiTi (right) coating

Appendix C – Erosion Behaviour

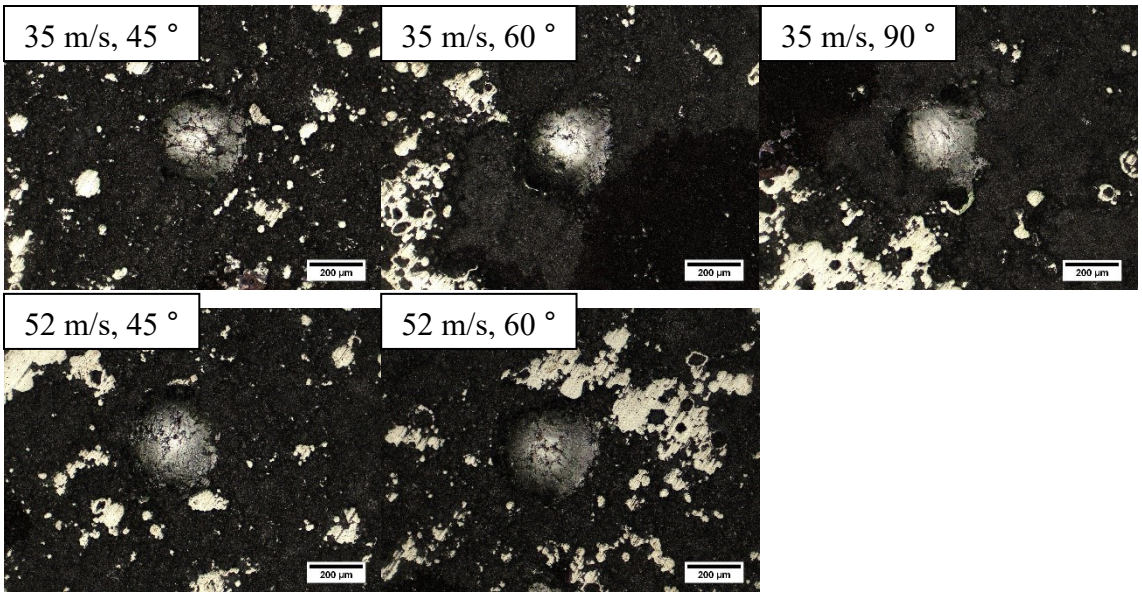

Figure 0-9 SPE indents for 5.14 wt.% NiTi coating

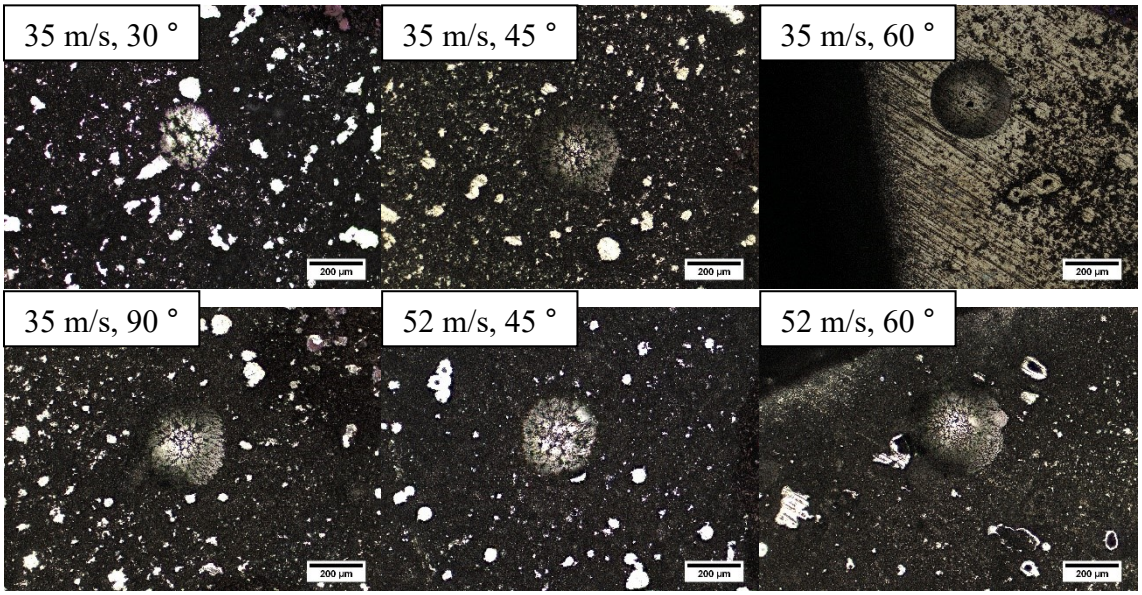

Figure 0-10 SPE indents for 6.07 wt.% NiTi coating

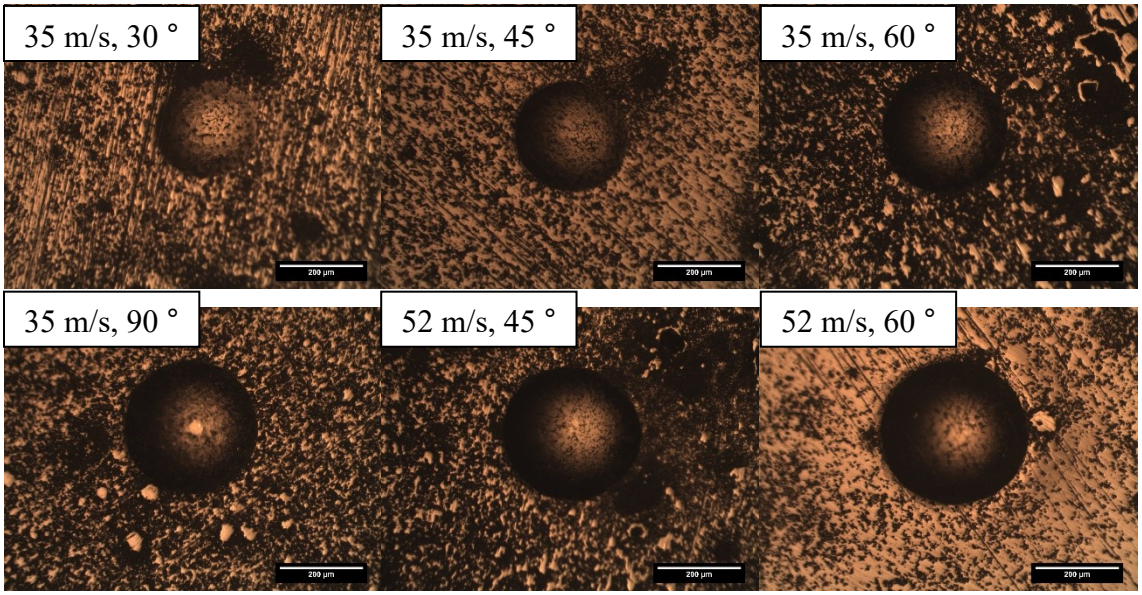

Figure 0-11 SPE indents for 7.02 wt.% NiTi coating